MESO-MECHANICAL ANALYSIS OF STEEL FIBER REINFORCED CEMENTITIOUS COMPOSITES

THIS IS A TEMPORARY TITLE PAGE
It will be replaced for the final print by a version
provided by the service academique.

Facoltà di Ingegneria
Università degli Studi di Salerno
Dottorato in Ingegneria delle Strutture e del Recupero Edilizio ed Urbano

and

Facultad de Ciencias Exactas y Tecnología
Universidad Nacional De Tucumán
Doctorado en Ciencias Exactas e Ingeniería

for the obtention of the degree of Doctor of Philosophy
Binationally co-supervised PhD Thesis Argentina / Italy

Candidate:

Antonio Caggiano

Thesis Jury:

Prof Name Surname, president of the Jury
Prof Guillermo Etse and Prof Enzo Martinelli, thesis advisors
Prof Name Surname, Rapporteur
Prof Name Surname, Rapporteur
Prof Name Surname, Rapporteur

Fisciano (SA), Italy, 2013

TO BE WRITTEN
TO BE WRITTEN
— Antonio Caggiano

To my parents...

Acknowledgements

TO BE WRITTEN

Caggiano, Salerno, Italia, February 4th 2013 A. C.

Preface

A preface is not mandatory. It would typically be written by some other persons (e.g., the thesis directors).

Salerno, February 4th 2013 G. E. and E. M.

Abstract

TO BE WRITTEN

Sommario

Da scrivere

Resumen

A escribir

Contents

List of Figures

List of Tables

1 Introduction

1.1 Scientific framework and general overview

Cement-based materials like concrete and most of the cohesive-frictional media are characterized by low strength and brittle response in low confinement and tensile stress states. These deficiencies can be mitigated by randomly adding short reinforcements into the cement mortar [Gettu, 2008].

Fiber-Reinforced Cementitious Composite (FRCC), obtained by randomly mixing short fibers (made out of steel, plastic, natural materials, recycled reinforcements, etc.) into conventional cementitious materials, is a structural material characterized by a significant residual tensile strength in post-cracking regime and enhanced capacity to absorb strain energy due to fiber bridging mechanisms across the crack surfaces [Brandt, 2008, di Prisco et al., 2009, Nguyen et al., 2010]. In particular, fibers play a relevant role in the post-cracking regime providing resistance to crack opening processes. In this sense, Fiber-Reinforced Cementitious Composites (FRCCs) may results in a less brittle and possible quasi-ductile behavior even in case of tensile loading, exhibiting strain-hardening processes with multiple cracks and relatively large energy absorption prior to failure. Composites with these relevant features take the name of High Performance Fiber-Reinforced Cementitious Composites (HPFRCCs) [Naaman and Reinhardt, 2006].

Several recently published experimental researches, related to the mechanical characterization of FRCC, allowed to clarify relevant aspects. Among others, it can be referred the evaluation of the workability dependence on the fiber distributions by Ferrara and Meda [2006], and that of the fiber orientations on the compaction procedures by Gettu et al. [2005]. Experimental tests aimed at investigating the FRCC failure behavior in compression and tension were performed, among others, by Ezeldin and Balaguru [1992] and Barros and Figueiras [1999], respectively. Also, the work by Shannag et al. [1997] that defines the mechanisms governing the fiber pull-out response, and those by Buratti et al. [2011] and Tlemat et al. [2006] that analyze the post-cracking behavior of three- and four-point bending tests, respectively. Finally, it should be also noted the

failure behavior evaluations of Steel Fiber Reinforced Concrete (SFRC) subjected to multiaxial compressive states by Fantilli et al. [2011] and to the Brazilian test conditions by Liu et al. [1997]. Moreover, fibers spread up within the concrete matrix also influence its durability [Mechtcherine, 2012], as they control the crack opening and reduce the diffusion phenomena which lead to corrosion [El-Dieb, 2009]. While the benefits of fibers on strength and ductility were demonstrated in Valle and Buyukozturk [1993] and Khaloo and Kim [1997] based on direct shear test results on FRCC specimens characterized by different strength levels. Also, the positive effect of fibers on the dynamic response under impact actions was also investigated by Xu et al. [2012].

Recent researches on Fiber-Reinforced Concrete (FRC) also addressed to the possible use of mixed fibers of different geometry and/or material which can, in principle, play a synergistic role in enhancing flexural and post-cracking response of FRC members. This kind of fibrous cement-based composites are known as Hybrid FRC (HyFRC). Experimental tests aimed at investigating the HyFRC failure behavior in direct tension were performed, among others, by Sorelli et al. [2005] and Park et al. [2012]. The mechanical behavior measured by means of indirect tensile tests were proposed on Hy-Polypropylene FRC [Hsie et al., 2008], Hy-Steel FRC [Banthia and Sappakittipakorn, 2007, Kim et al., 2011] or combining several material fibers: i.e., Carbon/Steel/Polypropylene FRC [Yao et al., 2003] or Steel/Palm/Synthetic FRC [Dawood and Ramli, 2011, 2012]. The experimental results on contoured double cantilever beam specimens with steel and polypropylene FRC was given by Banthia and Nandakumar [2003]. Other relevant contributions regarding HyFRC with lightweight aggregates [Libre et al., 2011], high-volume coarse fly ash [Sahmaran and Yaman, 2007], RC beams with mixed fibers [Ding et al., 2010], HyFRC exposed to high temperatures [Chen and Liu, 2004, Ding et al., 2012] or self compacting HyFRC [Ding et al., 2009, Dawood and Ramli, 2010, Akcay and Tasdemir, 2012] are proposed by the scientific community.

In the recent past, several theoretical models were proposed for investigating the mechanical behavior of cement-based material with or without fibers. Plenty of those researches were recently proposed for investigating the fracture behavior on both plain concrete [Bazant et al., 1990, Carol et al., 1997, Pandolfi et al., 2000, van Mier et al., 2002] and FRCC [Radtke et al., 2010, Gal and Kryvoruk, 2011, Caggiano et al., 2011, 2012b, Cunha et al., 2012, Laranjeira et al., 2012, Pereira et al., 2012]. A more detailed and comprehensive review on this topic is given in the following Sections 1.2 and 1.3.

1.2 Observation scale and modeling

A large amounts of theoretical models and numerical tools were proposed with the aim to realistically predict the physical and mechanical properties of concrete at each size scale. An extended literature review of the proposed constitutive theories for modeling the concrete behavior on the above focus was given in Dolado and van Breugel [2011].

Concrete and other cementitious materials are multiphase (composite) materials. At macroscale, concrete can be considered as a homogeneous continuum material, while at lower levels of observation, it is considered as a multiphase material as outlined in Fig. 1.1.

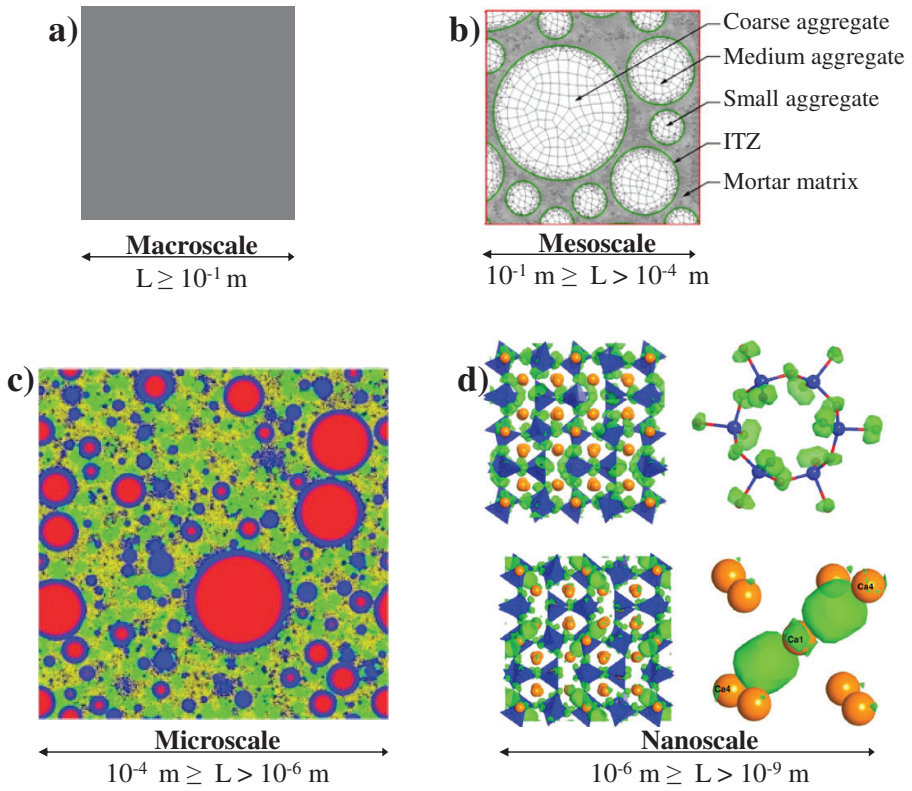

Figure 1.1: Concrete materials under different length scales: (a) macroscale continoum, (b) 2-D meso-scale concrete analysis [Kim and Al-Rub, 2011], (c) modelling the hydration of cements at microscale [Bishnoi and Scrivener, 2009] and (d) simulations by means of electrophilic and nucleophilic attack at a nanoscale standpoint [Puertas et al., 2011].

Based on the above discussion and referring to the fibrous cements, it can be stated that constitutive models, currently available in the scientific literature for simulating the mechanical response of FRCC, can be classified on the basis of their observation scale as proposed in the following subsections.

1.2.1 Structural-scale models

These models, based also on the general continuum approach, capture the essence of structural members made of FRCC. Typical examples of structural-scale formulations are those related to either cross-sectional moment versus curvature or panel shear force versus lateral displacements. For instance, structural-scale formulations for

FRCC structures were proposed by Stang and Olesen [1998] and Lee and Barr [2003] who characterized the complete load-deflection curve for FRCC three-point beams, as well as Billington [2010] that proposed a formulation for retrofit analysis of structures made of ductile FRCC. Regarding bending behavior of FRCC beams a comprehensive summary can be found in Zhang and Stang [1998] where different semi-analytical models based on the stress equilibrium in critical cracked sections were presented.

1.2.2 Macro-scale models

In this case FRCCs were ideally considered as continuum media and modeled within the theoretical framework of the smeared crack approach. Among the others, the contributions by Hu et al. [2003], who proposed a single smooth biaxial failure surface for FRCC, the one by Seow and Swaddiwudhipong [2005], who introduced a five parameter failure criterion for FRCC with both straight and hooked-end steel fibers, and the paper by Minelli and Vecchio [2006], who proposed a model based on a modification of the compression field theory, are worthy of mention. Other relevant contributions can be found in Beghini et al. [2007] and Guttema [2003].

1.2.3 Meso-scale models

Thereby the interaction among the different phases of the composite (i.e. fibers, matrix and coarse aggregates and their interfaces) was explicitly considered. Key contributions in this filed were due to Schauffert and Cusatis [2012] and Schauffert et al. [2012] who considered the effect of fibers dispersed into a proposed lattice discrete particle model (LDPM), as well as in Etse et al. [2012], Oliver et al. [2012] Vrech et al. [2010], Leung and Geng [1998], Bolander and Saito [1997], Alwan et al. [1991], Stang et al. [1990], Etse et al., among the others.

1.2.4 Microscale models

Micro-scale models were based on the observation scale in which the cement paste was described in terms of their chemical constituents which thermodynamical reactions, during the time, play a key role.

In this field, contributions dealing with the microstructure hydration/dehydration concepts were often treated as competitive approaches for describing properties of early age concrete (to see Schutter [2004], Camps et al. [2008] and Schlangen et al. [2007]) and concrete degradation under high temperature (i.e., Pont and Ehrlacher [2004], Ulm and Coussy [1999a] and Ulm and Coussy [1999b]), respectively.

1.2.5 Nanoscale models

Atomistic simulations at nano-level were typically conceived within the modeling of the cementitious crystals (namely, tobermorite and jennite). Particularly, several and innovative researches were carried out on the description and modeling the crystalline phases of cementitious materials such as the C_3A [Manzano et al., 2009b], etringite [Manzano et al., 2008], C_3S, $\beta - C_2S$ and portlandite [Manzano et al., 2009a].

1.2.6 Multi-scale models

In these models coupling effects of the different scales of observation were taken into account: i.e. nano-, micro-, meso-, macro- and structural scales of observation. The objective of these formulations is to develop an efficient approach to simulate the intrinsic multi-scale and multi-physics nature of the problem under consideration [Kabele, 2002, Hund and Ramm, 2006].

1.3 Crack modeling strategies and approaches

The mechanical behavior of concrete-based materials is greatly affected by crack propagation under general stress states. The presence of one or more dominant cracks in a concrete member modifies its structural behavior, possibly leading to brittle failure modes. The random dispersion of short steel fibers in cement materials is a new methodology used for enhancing the response in the post-cracking regime. Particularly, as the behavior of Fiber-Reinforced Cementitious Composite (FRCC) compared to conventional plain concrete, is characterized by several advantages, e.g., higher tensile and shear resistance, better post-cracking ductility, higher fracture energy, etc.

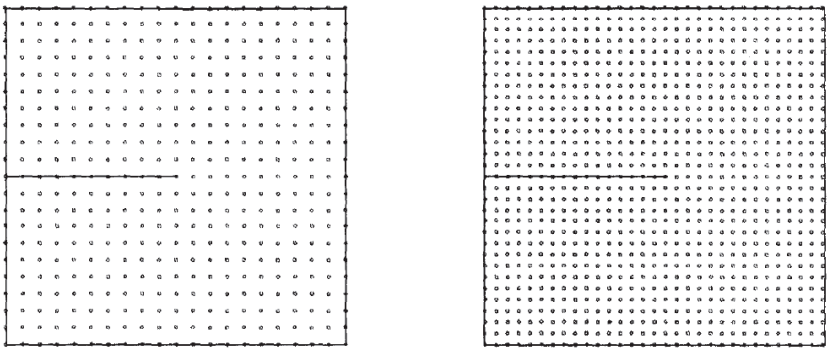

Figure 1.2: Numerical specimens based on the EFG method by Belytschko et al. [1995] for the near-tip crack problems.

Theoretical models and numerical procedures are needed for describing both cracking

onset and propagation in non-homogeneous quasi-brittle materials such as FRCC. In fact, simulating cracking phenomena in solids is still an open issue in computational mechanics. Concrete cracks were traditionally treated by means of classical continuum or smeared-crack approaches in which the fracture zone was considered to be distributed in a certain region of the solid [De Borst and Guitierrez, 1999]. Despite its advantages from the computational point of view, classical concrete models based on the smeared crack approach suffered a strong FE-size dependence of the localization band width, see a.o. Oliver [1989], Rots et al. [1985] and others. Different regularization procedures were proposed to avoid this severe deficiency of the smeared-crack approach. On the one hand, continuum models were based on fracture mechanics concepts leading to fracture energy release regularization but still suffering from loss of objectivity of the deformation pattern. Fracture energy-based concrete models were, among others, due to Bazant and Oh [1983], Willam et al. [1984], Etse and Willam [1994], Shah [1990], Carpinteri et al. [1997], Comi and Perego [2001], Duan et al. [2007] and Meschke and Dumstorff [2007]. On the other hand, more sophisticated constitutive theories were proposed to solve the strong mesh dependency which appears when the governing equations turn ill posed. They were based on rate dependency, higher strain gradients, micropolar theory, etc. Among others it can be referred here the contributions by Vardoulakis and Aifantis [1991], de Borst et al. [1995], Peerlings et al. [2004], Lee and Fenves [1998], Carosio et al. [2000], Etse et al. [2003], Vrech and Etse [2009], etc.

Discrete Crack Approaches (DCAs) aimed at incorporating strain or, moreover, displacement discontinuities into standard FE procedures have progressively became an attractive and effective alternative to the smeared-crack approach. Several proposals in the last years were currently available to introduce crack discontinuities within FE domains and are outlined in the following paragraphs.

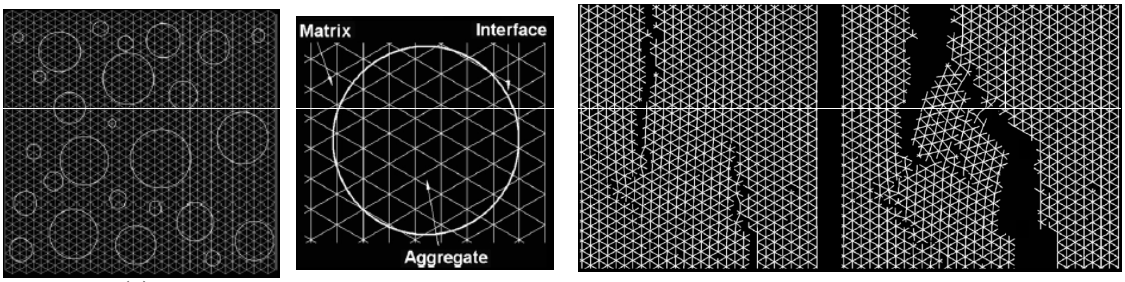

(a) (b) (c)

Figure 1.3: Meso-mechanical simulation by means of the beam lattice model [Lilliu and van Mier, 2003]: (a) the geometry, (b) definition of matrix, interface and aggregates, then (c) the crack pattern simulation.

Element-Free Galerkin (EFG): this method represents an another attractive tool for modeling the propagation of material cracks. The EFG approach differs from the classical Finite Element Method (FEM) because the discretization was achieved by only nodal data (Fig. 1.2): no element connectivity was stated. The description of the

geometry and the numerical model formulation of the problem was given only on a set of nodes jointly with a description of exterior and interior boundaries. Significant contributions to static elasticity and fracture mechanics were given in Belytschko et al. [1995], Belytschko et al. [2000], Singh et al. [2011] and Zhang et al. [2008].

Lattice models: within the framework of discontinuous crack approaches and fracture behaviors of concrete elements, the lattice-based model was a simple and effective tool for understanding the physics of fracture processes [Yip et al., 2006]. Lattice type models can be based on either truss elements [Schorn and Rode, 1987] or beam ones [Lilliu and van Mier, 2003].

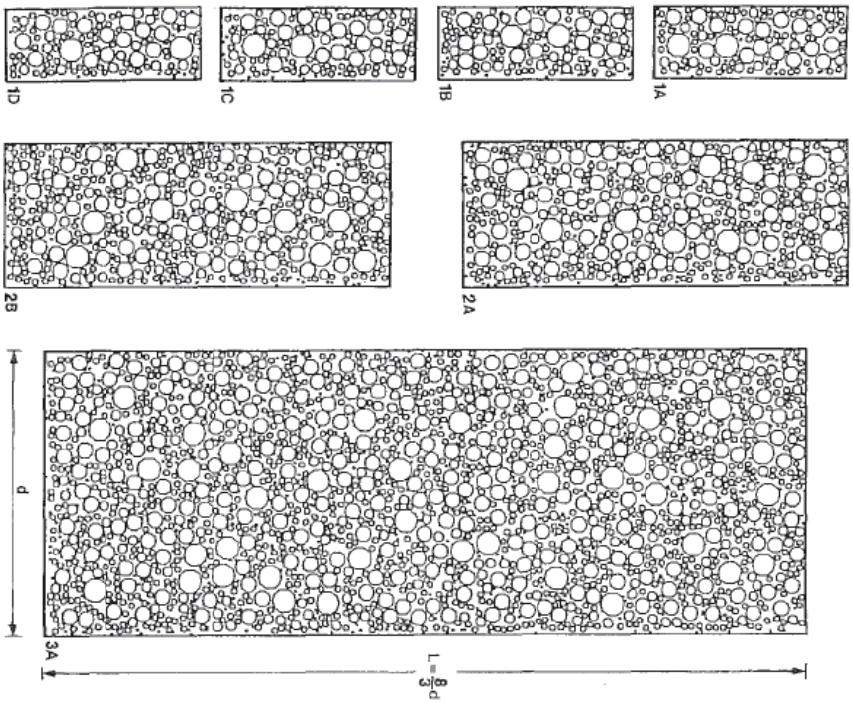

Figure 1.4: Unnotched specimens in tension of various sizes with randomly generated particles by Bazant et al. [1990].

Particle models: these models were based on the formulation of the microscopic inter-particle contact layers of the matrix particles [Jirasek and Bazant, 1994]. The pioneer proposals of particle simulation were reported in the works of Cundall [1971], Rodriguez [1974] and Kawai [1980]. These works mainly modeled the behavior of granular solids (such as sand) considering rigid particles that interacted by friction. Furthermore, a particle model for brittle composite materials was proposed by Zubelewicz and Bazant [1987] and Bazant et al. [1990], for simulating cracking localization in concrete elements. Fig. 1.4 outlines several particle schemes adopted by Bazant et al. [1990] for studying the size effect on the failure load for unnotched specimens in tension.

Strong discontinuity approaches: they allowed for displacement discontinuities into

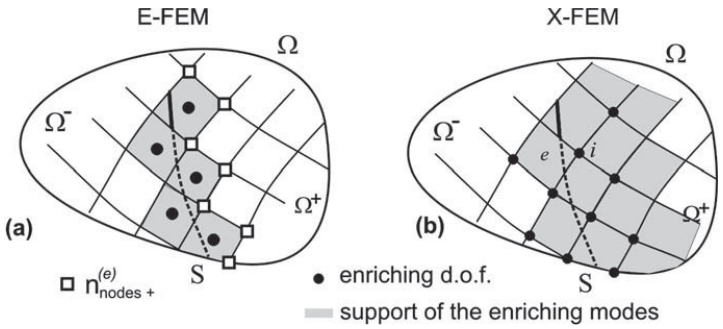

Figure 1.5: Elemental (E-FEM) and eXtended (X-FEM) enrichment approaches [Oliver et al., 2006].

the finite element formulations for capturing arbitrary crack propagation with a fixed FE mesh without loss of mesh objectivity. Particularly, new types of finite elements, essentially formulated for enriching the (continuous) displacement modes with additional discontinuities, were proposed. It can be distinguished two broad families dealing with the techniques aimed at enriching the discontinuous displacement modes:

- the Embedded strong discontinuity Finite Elements (E-FEM), proposed among others by Dvorkin et al. [1990], Oliver et al. [2002], Oliver [1996] and Armero and Linder [2009], which were able to reproduce displacement jumps through elemental discontinuity enrichments (Fig. 1.5a), and
- the eXtended Finite Element Method (X-FEM) which captured the discontinuity by means of nodal enrichments (Fig. 1.5b) by Wells and Sluys [2001] and Liu et al. [2011].

An interesting comparison between the E-FEM and X-FEM approaches, to model strong discontinuities in concrete materials, was proposed by Oliver et al. [2006].

Zero-thickness interface models: an alternative approach for discrete finite element failure analysis was represented by interface crack models. Zero-thickness joints connect continuum solid elements throughout potential crack lines as outlined in Fig. 1.6. The material failure in crack processes was captured by means of those elements for discrete constitutive analyses, relating contact stresses (in normal and/or tangential direction) and the relative displacements (crack opening and sliding) with specific constitutive models, e.g., Hillerborg et al. [1976], Carol et al. [1997], Pandolfi and Ortiz [2002], Lorefice et al. [2008], etc. Interface formulations may only include traction-separation laws [Olesen, 2001, Oh et al., 2007, Buratti et al., 2011] or, eventually, constitutive relations based also on the more complex mixed-modes of fracture [Carol et al., 1997, Hillerborg et al., 1976, Pandolfi et al., 2000, Park et al., 2010].

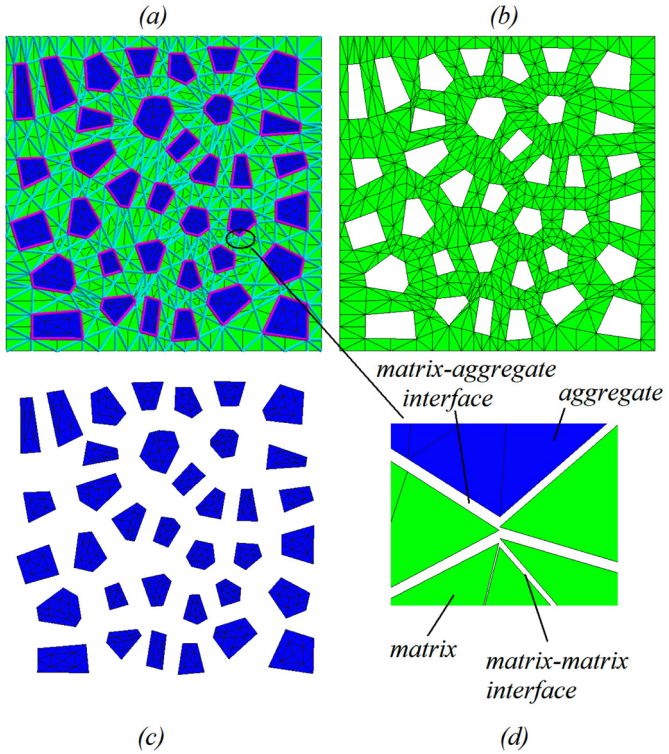

Figure 1.6: FE discretization [Lopez et al., 2008a,b] of (a) 6 x 6 aggregate-arrangement, (b) matrix, (c) coarse aggregates and (d) interfaces.

Among the different procedures in the framework of the discrete crack approach, the one based on zero-thickness interface elements was particularly interesting due to the simplicity of the involved numerical tools as the non-linear kinematics were fully defined in the displacement field.

1.4 Fiber-reinforced cementitious composites: Codes and Standards

1.4.1 State-of-the-art review

In the last decades, a large amounts of studies were performed in order to better understand the mechanical properties of Fiber-Reinforced Cementitious Composite (FRCC). However for many years, the lack of international codes, standards and guidelines for the design purpose of FRCC members slowed its expansion in structural application. As a matter of fact, the use of FRCC was principally limited to non-structural applications such as cracking control, durability enhancements, etc.

The incorporation of fibers as reinforcements substituting (even if in partial substitution) the classical steel rebars was strongly considered in the last twenty years, after

the publication of many design guidelines and codes in Europe: for example, the Sweden code [Stalfiberbetong, 1995], the Swiss recommendations [SIA-162-6, 1999], the German code [DBV, 2001], the Austria guidelines [Faserbeton-R, 2002], the French recommendations [AFGC-SETRA, 2002], the guidelines provided by the RILEM Committee [RILEM-TC162-TDF, 2003], the Italian codes [UNI-11039-1, 2003, UNI-11039-2, 2003, UNI-11188, 2004, CNR-DT-204, 2006], the Spanish code [EHE08, 2008] and the very recent new fib Model Code [fib Model-Code, 2010a]. Further design considerations were introduced by the American standards ACI-544.4R-88 [1996] and ACI-318-08/318R-08 [2008].

Some of these codes explicitly distinguished non-structural against structural applications based on the fiber types and dosages employed in such an applications. Particularly FRCC for structural members are that able to guarantee minimum FRCC performance (mainly measured in terms of toughness indexes or post-cracking parameters: see for example UNI-11039-1 [2003]).

Several constitutive models were proposed in current national and international codes in order to design FRCC structures. These constitutive proposals principally deal with tensile formulations through either stress-strain (σ-ϵ) or stress-crack opening displacement ($\sigma - w$) curves [Blanco et al., 2013].

Despite the large variety of existing constitutive models for FRCC designs, this section is aimed at reviewing and classifying the main proposals given by standards and recommendations available in literature. Particular focus will give in Subsection 1.4.2 to the fib Model-Code [2010a] which is largely considered as the worldwide reference for FRCC in structural applications.

The post-cracking tensile behavior and the parameters which identify such a relationship represent the key ingredients in design for FRCC members. On the one hand there are several guidelines which propose a different type of $\sigma - \epsilon$ diagram to be used for design purposes: i.e., the rectangular shapes given by DBV [2001], CNR-DT-204 [2006], EHE08 [2008], fib Model-Code [2010a], the bilinear proposals [DBV, 2001, CNR-DT-204, 2006], trilinear relationships [DBV, 2001, RILEM-TC162-TDF, 2003] and multilinear models [DBV, 2001, fib Model-Code, 2010a] (Fig. 1.7).

On the another hand the main parameters which define each one of the above models are derived by means of experimental tests which recommendations are given by others companion codes. It can be taken as reference the test recommendations of several countries such as Italy [UNI-11039-1, 2003, UNI-11039-2, 2003], USA [ACI-544.2R-89, 1996, ASTM-C-1018, 1998], Spain [UNE-83510, 1989], France [NFP-18409, 1993], Belgium [NBN-B-15-238, 1992], Japan [JSCE-SF4, 1984], Germany [DIN-1048, 1991], Netherlands [CUR, 1994], Norway [NB, 1993], EU standards [EN-14651, 2005] and the Rilem international test procedure [RILEM-TC162-TDF, 2002].

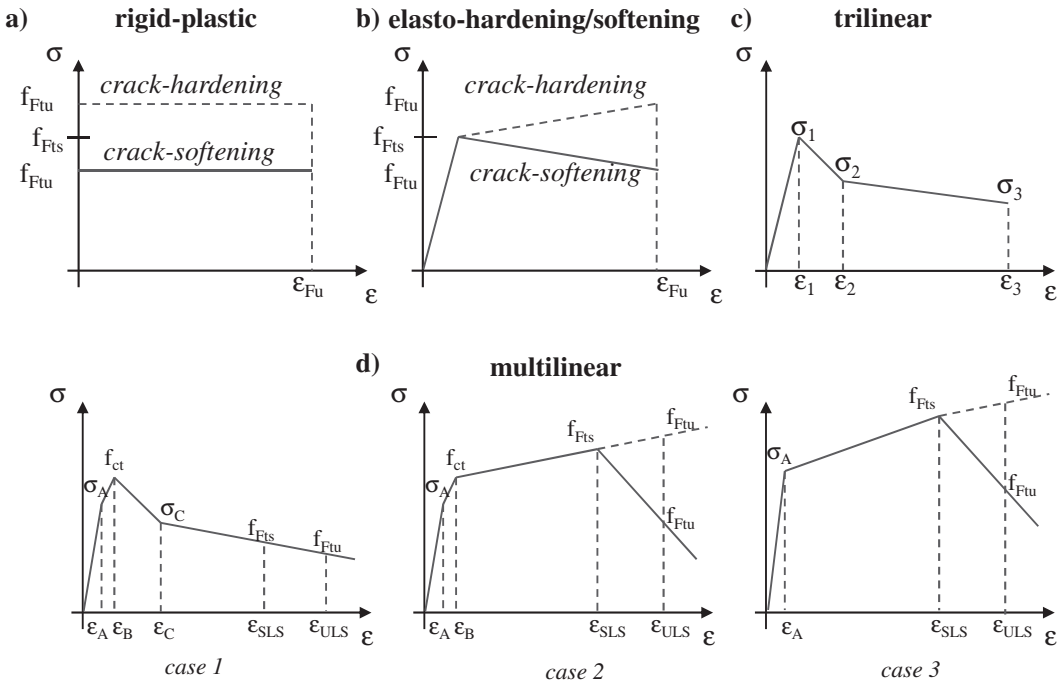

Figure 1.7: Constitutive $\sigma - \epsilon$ laws for the tensile behavior of FRCC: a) rectangular and b) bilinear shapes [CNR-DT-204, 2006], c) trilinear law [RILEM-TC162-TDF, 2003] and d) multilinear rules [fib Model-Code, 2010a].

These codes mainly were used as guide to experimentally obtain two quantities alternatively adopted in design: (i) the equivalent flexural tensile strength (f_{eq}) otherwise the residual flexural tensile strength (f_R). The first one (f_{eq}) is related to the work absorption capacity of the material, derived by means of the area enclosed under the experimental force-crack tip opening displacements [Caggiano et al., 2012a] while the second parameter (f_R) corresponds to the stress associated to the force at a certain deflection measures or crack opening values [Barros et al., 2005].

1.4.2 The new fib Model Code 2010

Recently, the lack of the international guidelines and codes for Fiber-Reinforced Concrete (FRC) elements in structural applications was strongly filled by means of the publication of the new fib Model-Code [2010a] which aims at updating and reviewing the previous CEB-FIP-90 [1993]. In this regard, FRC was introduced into the "Technical Groups fib TG 8.3" (*Fibre reinforced concrete*) and "fib TG 8.6" (*Ultra high performance FRC*). In this subsection the fundamental assumptions and the main design guides for FRCC, proposed into the fib Model-Code [2010a], are reported and discussed.

Uniaxial behavior: compressive and tensile stress-strain

One of the most important aspect regarding the mechanical response of FRC was represented by its behavior in tension. Different test methods were possible for assessing the post-cracking behavior of FRC. However, the bending test on prismatic specimens was the most popular and widely used experimental technique. It is relatively simple to realize and can be representative of many practical situations.

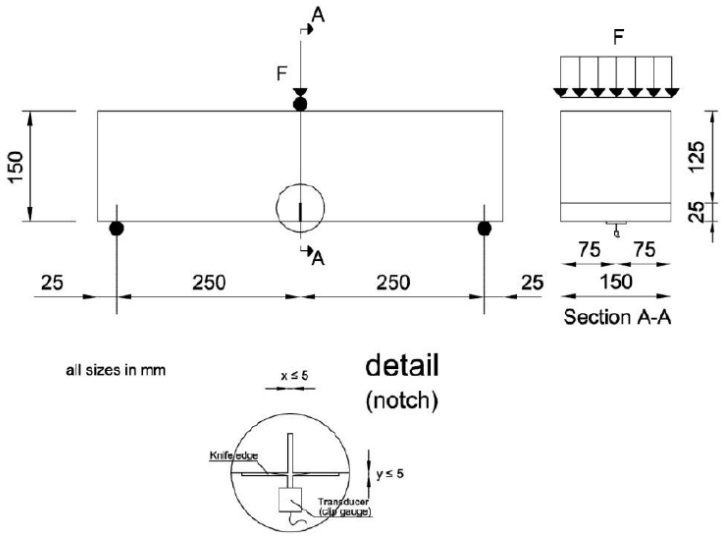

Figure 1.8: Experimental set-up and geometry details of the notched beams under three-point bending test [fib Model-Code, 2010a].

The fib Model-Code [2010a] considered residual flexural tensile strengths determined by performing 3-point bending tests (Fig. 1.8) on notched prisms according to EN-14651 [2005]. Particularly, the residual flexural tensile strengths, $f_{R,j}$, were defined as

$$f_{R,j} = \frac{3F_j l}{2bh_{sp}^2} \tag{1.1}$$

being l and b the span length and width of the specimens, respectively, while h_{sp} is the distance between the notch tip and the top of the specimen; the j index refers to the considered Crack Mouth Opening Displacement (CMOD); then F_j is the load corresponding to $CMOD = CMOD_j$.

At last, the fib Model-Code [2010a], and as generally accepted into the worldwide guidelines, deals with the assumption that the compressive relations valid for plain concrete can further be applied to FRC.

Post-cracking strength and classification

The post-cracking strength in hardening or softening FRC is a material parameter which varies with the increasing crack opening displacement. Two crack values were typically considered: from one hand it was considered the opening crack which was significant for Serviceability Limit State (SLS) verifications, on the other hand a second crack should be significant for the Ultimate Limit State (ULS) [Eurocode-2, 2004].

The European standard EN-14651 [2005] proposed four different residual strengths: i.e., f_{R1}, f_{R2}, f_{R3} and f_{R4} (Fig. 1.9). They corresponded to specific values for the $CMODs$: $CMOD_1 = 0.5mm$, $CMOD_2 = 1.5mm$, $CMOD_3 = 2.5mm$ and $CMOD_4 = 3.5mm$, respectively. Particularly, f_{R1} and f_{R3} were the FRC residual strengths representative for the SLS and ULS, respectively.

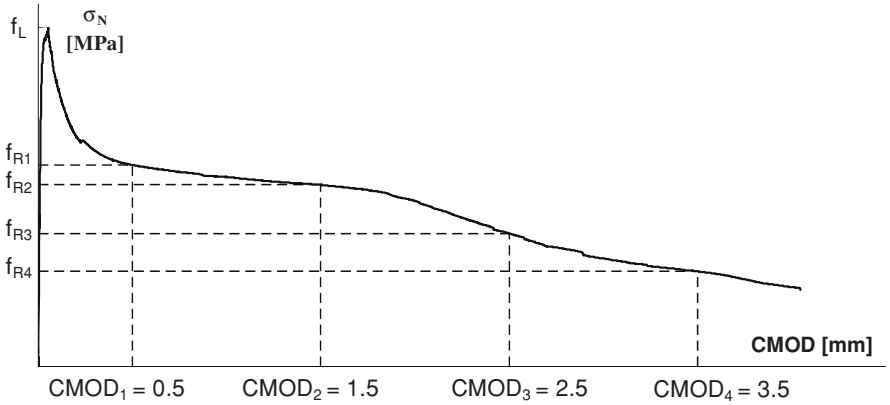

Figure 1.9: Typical curve of the nominal stress versus CMOD for FRCC [EN-14651, 2005].

Then, post-cracking residual strength and FRC toughness can be classified by using two parameters: the first one outlined the strength class and it was given by f_{R1}, while the second parameter (represented by a letter "a", "b", "c", "d" or "e") recognized the ratio between f_{R3} and f_{R1}. Particularly, the strength classes, based on the characteristic value of f_{R1}, were defined through the following values of ratio: 1.0 (if $f_{R1,k} \geq 1.0\,MPa$), 1.5 (if $f_{R1,k} \geq 1.5\,MPa$), 2.0 (if $f_{R1,k} \geq 2.0\,MPa$), 2.5 (if $f_{R1,k} \geq 2.5\,MPa$), 3.0 (if $f_{R1,k} \geq 3.0\,MPa$), 4.0 (if $f_{R1,k} \geq 4.0\,MPa$), 5.0 (if $f_{R1,k} \geq 5.0\,MPa$), 6.0 (if $f_{R1,k} \geq 6.0\,MPa$), 7.0 (if $f_{R1,k} \geq 7.0\,MPa$) and 8.0 (if $f_{R1,k} \geq 8.0\,MPa$).

The f_{R3}/f_{R1} ratio can be represented with the letters "a", "b", "c", "d" and "e", corresponding to the following characteristic strength values:

- "a" if $0.5 \leq f_{R3,k}/f_{R1,k} \leq 0.7$;
- "b" if $0.7 \leq f_{R3,k}/f_{R1,k} \leq 0.9$;
- "c" if $0.9 \leq f_{R3,k}/f_{R1,k} \leq 1.1$;

- "d" if $1.1 \leq f_{R3,k}/f_{R1,k} \leq 1.3$;
- "e" if $1.3 \leq f_{R3,k}/f_{R1,k}$.

According to fib Model-Code [2010a], in practical design minimum mechanical performances were required to FRC. Particularly, fiber reinforcement can be used in substitution (even partially) of conventional reinforcement at the ultimate limit state, if the following relationships were respected

- $f_{R1,k}/f_{L,k} > 0.4\,MPa$
- $f_{R3,k}/f_{R1,k} > 0.5\,MPa$

being $f_{L,k}$ the characteristic value of the nominal strength corresponding to the peak load (or the highest load value in the CMOD range $0-0.05\,mm$) according to the test specimen of EN-14651 [2005].

Constitutive laws for Limit State Analyses

Two alternative stress-crack opening relationships, as schematically proposed in Fig. 1.10, were considered by fib Model-Code [2010a] for the ULS:

- a **rigid-plastic model**, based on a unique reference strength, f_{Ftu}. Such a value was determined by means of the following relationship

$$f_{Ftu} = \frac{f_{R3}}{3} \tag{1.2}$$

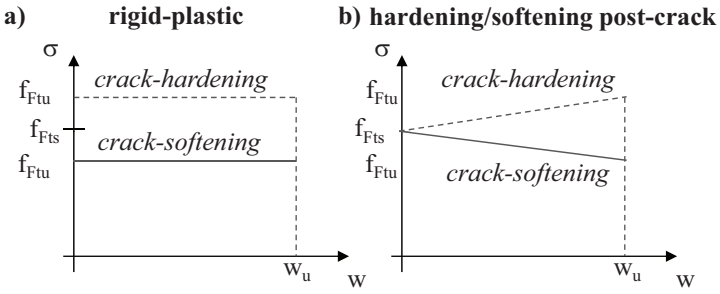

Figure 1.10: Post-cracking constitutive laws for ULS states [fib Model-Code, 2010a].

- a linear post-cracking behavior (hardening, perfectly plastic or softening) was formulated by means of two strength values: i.e., f_{Fts} and f_{Ftu}. These quantities used for the rigid-linear diagram of Fig. 1.10b were defined through the following equations

$$f_{Fts} = 0.41\,f_{R1} \tag{1.3}$$

$$f_{Ftu} = f_{Fts} - \frac{w_u}{CMOD_3}\left(f_{Fts} - 0.5f_{R3} + 0.2f_{R1}\right) \geq 0 \tag{1.4}$$

Therein f_{Fts} was the serviceability residual strength, relative to a crack opening value representative for the SLS analysis, while f_{Ftu} represented the post-cracking strength for the ULS. At last w_u is the maximum crack opening accepted in structural design and its value depends on the ductility required.

When concrete cracks are treated by means of classical smeared-crack models, as traditionally adopted in design procedures, the fracture zone must necessarily be considered as distributed in a certain region of the body. Based on this, classical models behaves with a loss of objectivity under softening responses. Actually, the definition of a stress-strain law is based on the identification of a crack width and on the corresponding structural characteristic length. The link between the stress-crack ($\sigma - w$) law and the stress-strain ($\sigma - \epsilon$) constitutive relationship was given by the introduction of a characteristic length, l_{cs},

$$\varepsilon = w / l_{cs}. \tag{1.5}$$

The characteristic length, for elements with conventional rebars, may be calculated as

$$l_{cs} = \min\{s_{rm}, y\} \tag{1.6}$$

being s_{rm} the mean distance between successive cracks while y represents the distance between neutral axis and tensile side of the cross section. Further details can be recognized into the fib Model-Code [2010a].

In sections without traditional reinforcement in bending, under combined tensile-flexural or combined compressive-flexural stresses, with resulting force external to the cross-section, the simplified expression of $y = h$ (being h the specimen height) can be assumed due to the very reduced extension of the compressed region. The same assumption can be taken for slabs.

In case of serviceability limit states analysis, the constitutive relationship adopted for plain concrete in uniaxial tension, was also used up to the peak strength f_{ct}. Then, in post-cracking regime, the multilinear laws given in Fig. 1.7d were considered. The post-cracking residual strength is defined by means of two points corresponding to (ϵ_{SLS}, f_{Ftsd}) and (ϵ_{ULS}, f_{Ftud}), where ϵ_{SLS} and ϵ_{ULS} were defined according to the considered limit states as outlined by the fib Model-Code [2010a].

Partial safety factors

Based on the stress-crack opening displacement relationship given in Fig. 1.10 and used for the ULS-design, the following strength values were considered

$$f_{tsd} = \frac{f_{tsk}}{\gamma_F} \tag{1.7}$$

and

$$f_{tud} = \frac{f_{tuk}}{\gamma_F} \tag{1.8}$$

where the recommended values for the material partial safety factors γ_F were given according to fib Model-Code [2010a]:

- *FRC in compression*: γ_F as for plain concrete;
- *FRC in tension (limit of linearity)*: γ_F as for plain concrete;
- *FRC in tension (post-cracking residual strength)*: $\gamma_F = 1.5$.

At last, for serviceability limit states, the partial factors should be taken as 1.0.

Design of FRC structures

The above constitutive laws and post-cracking strengths were then used for design rules as outlined in the "PART III: DESIGN" of fib Model-Code [2010b]. For the sake of brevity, the description of the design rules was omitted in this work. These details are beyond the scopes of the present thesis. However, further details can be founded in the fib Model-Code [2010b].

1.5 Thesis theoretical framework and methodology

The main objective of this thesis concerns the development of a 2D numerical model aimed at analyzing cracking phenomena in fiber-reinforced concrete and involving the explicit characterization of fiber effects on concrete cracks from a mesostructural point of view. Particularly, in this work an interface constitutive model for mesoscopic fracture analysis of FRCCs was firstly presented. For this purpose, FRCC can be regarded as a four-phase material (Figs. 1.11), composed by:

- (i) coarse aggregates,

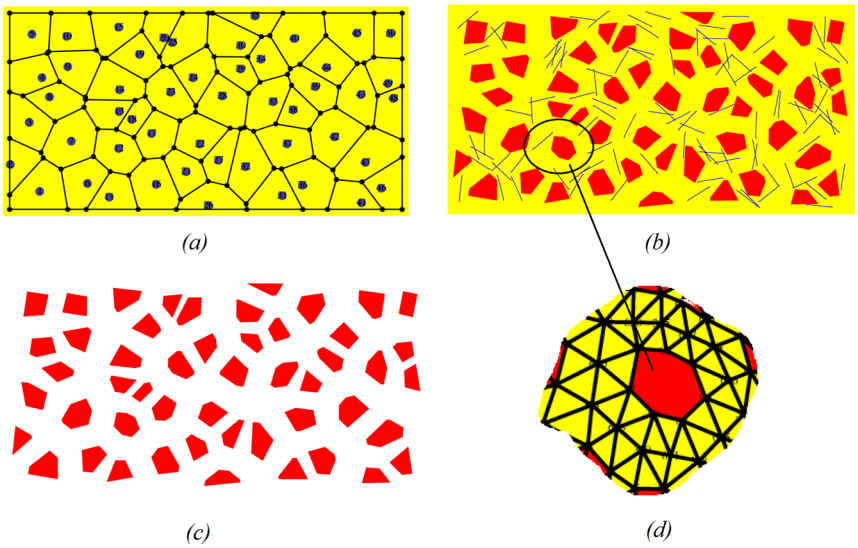

Figure 1.11: 2D meso-structure geometry: (a) Delaunay triangulation/Voronoi tessellation [Idiart, 2009], (b) FRCC meso-probe, (c) coarse aggregates and (d) position of the interface elements.

- (ii) plain mortar,
- (iii) plain interfaces modeling the cementitious matrix-to-coarse aggregate interaction and
- (iv) FRCC interfaces for the matrix-to-matrix crack modeling.

Only the coarse aggregates were explicitly discretized in the FE mesh and embedded in a matrix phase representing the cementitious mortar plus smaller aggregates and fibers. In principle, a explicit meso-geometry permits to correctly model fracture and failure processes in concrete which are generally governed by the main heterogeneities in the composite. A convex polygonal representation was adopted for representing the large aggregates. The polygonal geometry was numerically generated though standard Voronoi/Delaunay tessellation [Klein, 1989] from a regular array of points which was slightly perturbed as shown in Fig. 1.12. Both the polygonal particles and the space between them (surrounding matrix) were meshed with finite elements for generating the modeling analysis. The continuum elements obtained by means of the above procedure were assumed to be linear elastic, whereas all nonlinearities were concentrated within zero-thickness interface elements defined throughout the adjacent edges of the meshed elements. Non-linear fracture-based laws and fiber actions (in terms of both bridging and dowel effects) were introduced in those interface elements according to the formulation outlined in this thesis. In particular, aggregate-matrix interfaces did not consider the effect of fibers, while matrix-matrix ones took into account the contribution of passing through fibers. As a matter of fact, interface elements represented

the potential crack patterns which can develop during the analysis process.

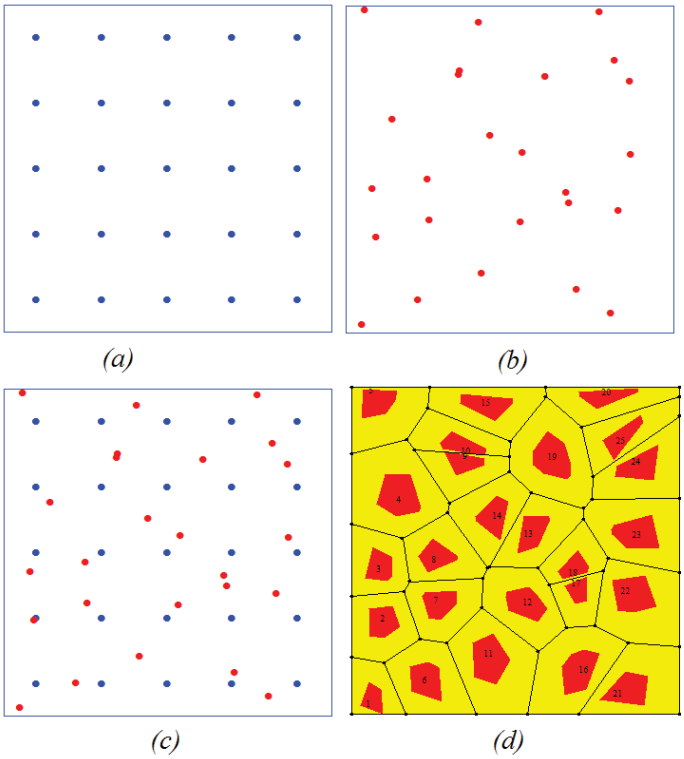

Figure 1.12: (a) Initial regular 2D distribution, (b) randomly perturbed positions, (c) superposition of the points and (d) Voronoi/Delaunay tessellation.

The non-linear behavior of steel fiber-reinforced concrete/mortar was fully captured by means of the model formulation for zero-thickness joint elements [Caggiano et al., 2012b]. The constitutive proposal was based on the original idea of Carol et al. [1997] modified and extended to fiber concrete composites on the basis of the well-known "Mixture Theory" [Trusdell and Toupin, 1960] also employed by Manzoli et al. [2008] for RC members. Actually, the following four "ingredients" were accounted with the aim of formulating the post-cracking behavior of FRCC materials:

- (i) the reformulation of a fracture-based interface model for simulating the mixed cracking modes occurring in cement-based materials,
- (ii) the adoption of the well-known "Mixture Theory" to combine the composite response,
- (iii) the fiber-to-surrounding concrete bond-slip behavior and at last
- (iv) the dowel effect between concrete cracks and crossing fibers.

It is important to note that the entire progress made in the modeling of the fiber effects on concrete composites and on concrete mortars was classically based on the continuum smeared crack approach. This included most of the proposals related to macro-scale models where the fiber-reinforced matrix was considered as a continuum. As it is well known, classical or continuum models for simulating quasi-brittle materials like concrete were characterized by strong FE-size dependence of the localization band width and, consequently, to a loss of objectivity of their results.

On the contrary, in Discrete Crack Approaches (DCAs), the discontinuity of the displacement field due to cracking was directly accounted into the finite element formulation. The most effective procedure to use the DCA was the one based on interface elements. The zero-thickness interface formulation, proposed in this thesis, was particularly interesting due to the simplicity of the involved numerical tools as the non-linear kinematics were fully and directly defined in the displacement field.

1.6 Thesis structures and main contents

After this Introduction chapter, the thesis is structured as outlined in the following descriptive paragraphs.

At first, Chapter 2 reports the results of an extensive experimental campaign realized on several prismatic concrete specimens, which were cast by using different types and amounts of steel fibers and successively tested under four-point bending. Particularly, it was analyzed Steel Fiber-Reinforced Concrete (SFRC) specimens prepared with two different fiber contents (i.e., 0.5% and 1.0% of volume fraction). Moreover, for each fiber content, five different combinations of long and short fibers were considered with the aim of investigating the possible influence of those combination on the resulting behavior of SFRC specimens.

Chapter 3 presents a novel model for Fiber-Reinforced Cementitious Composites (FRCCs) based on a cohesive-frictional interface theory. The formulation of a zero-thickness joint model was given for simulating the fracture behavior at meso-phases level of fiber-reinforced concretes. In particular, the "Mixture Theory" was used for describing the coupled action between concrete and fibers. Then, the softening behavior of the interface model due to crack propagation was outlined by means of an incremental approach, which was similar to the one usually adopted in the classical flow theory of plasticity. A novel bond-slip model was presented, in order to correctly simulate the axial effect of fibers on concrete cracks. Also, the composite action between concrete and fiber reinforcements was also completed by considering the transversal fiber effect by means of a dowel model.

Chapter 4 reports the explicit formulation for simulating the debonding behavior of fibers embedded in cementitious matrices. Such a formulation was based on assuming

a bond model between interface stresses against the corresponding relative displacements. The considered formulation addresses the behavior of fibers under tensile axial stresses which resulted in a "mode II" debonding phenomenon. The proposed unified formulation was straightforwardly employed into the interface proposal described in Chapter 3. The adoption of the presented formulation within the general framework of discontinuous cracking models of FRCC was, at the same time, the key motivation and the most relevant development of the Chapter 4. At the ultimate part of the same chapter, numerical analyses for validating the proposed formulation against relevant experimental pull-out results was discussed.

In Chapter 5, the numerical results realized for estimating the soundness and capabilities by using the proposed interface model in FRCC specimens were presented. In the first section, the interface model was just calibrated by using experimental results performed on SFRC probes tested under pure tensile stress cases by considering the experimental tests by Li et al. [1998]. Furthermore, the stress history on plane concrete panels by Hassanzadeh [1990] were considered to asses the predictive capability of the model in terms of failure behavior of SFRC specimens in mixed-modes of fracture. Next, the second section was intended to study the incidence of steel fibers on the post-cracking performance for several stress states under overall possible failure modes. For this purpose, several interface cracking conditions were considered and analyzed through a defined "cracking indicator".

Chapter 6 explores the analyses of boundary value problems by means of the Finite Element Method in order to show numerical simulations at structural level carried out with the proposed interface constitutive model. The attention of this Chapter was focused on the analysis of the failure behavior of Steel Fiber-Reinforced Concretes (SFRCs) evaluated at both macro and mesoscale levels of observation.

Chapter 7 deals with a nonlinear cracked hinge model aimed at reproducing the bending fracture behavior of fiber-reinforced concrete beams. The model was based on the fracture mechanics concepts of the fictitious crack model where the stress-crack opening relationship was accounted in a similar way obtainable by considering the pure "mode I" case of the discontinuous proposal formulated in Chapter 3. A closed-form solution for the stress-crack opening relationship with the explicit consideration of the fiber effects was presented. The applicability of this simplest model was demonstrated by simulating the bending fracture specimens under four-point bending conditions, objects of the Chapter 2.

Finally, Chapter 8 summarized the main final remarks and conclusions which can be figure out from this work. Also, further developments and the straightforward extensions of this work related to both continoum and discontinuous mechanical analyses of quasi-brittle materials, will be proposed and discussed.

2 Experimental characterization of concrete beams reinforced with mixed long/short steel fibers

This section presents the results of an experimental activity carried out on Fiber-Reinforced Concrete (FRC) obtained by mixing short and long hooked-end steel fibers. Eleven mixtures were considered including plain concrete as a reference and Steel FRC with 0.5% and 1.0% of fiber volume fractions. The experimental campaign was aimed at observing the key aspects of the mechanical behavior of FRC in bending. Notched plain and fiber-reinforced concrete specimens were tested under 4PB according to UNI-11039-1 [2003] and UNI-11039-2 [2003]. Particularly, the study was focused on examining the results of Four-Point Bending (4PB) tests performed on notched prisms. The structural behavior was evaluated in terms of traction-separation law of FRC and the possible influence of both amount and type of fibers was investigated.

In Section 2.1, a short overview of the standards and codes, dealing with the flexural test experiments in FRCC, will be proposed. Then, Section 2.2 describes the analyzed mixtures and experimental test methods employed in the present research. Section 2.3 reports the experimental results of both compressive and four-point bending tests. Finally, some concluding remarks are given in Section 2.4.

2.1 Flexural tests for obtaining residual strengths

Steel Fiber-Reinforced Concrete (SFRC), obtained by mixing short fibers and cement-based mixtures, are becoming extensively used materials in civil engineering applications, particularly those related to structures [Ferro et al., 2007, di Prisco et al., 2009].

Main benefits of SFRC are the very high ductility improvement of structural components and the significant enhancement of residual strengths in final or cracked stage [Barros and Figueiras, 1999]. The superior ductility of structures made of SFRC, particularly in post-peak regimes, were typically observed, under both pure mode I type of failure [Gopalaratnam and Gettu, 1995] and mixed failure modes [Carpinteri and Brighenti, 2010], through flexural tests.

Several National and International Codes deal with the flexural test methods for measuring the relevant mechanical properties of FRC [JSCE-SF4, 1984, UNE-83510, 1989, NBN-B-15-238, 1992, NFP-18409, 1993, ASTM-C-1018, 1998, SIA-162-6, 1999, DBV, 2001, RILEM-TC162-TDF, 2002, UNI-11039-1, 2003, UNI-11039-2, 2003, EN-14651, 2005, DAfStB, 2010].

The bending test of prismatic specimens is the most popular and widely used experimental technique for assessing the post-cracking behaviour of FRC. It is relatively simple to realise and can be representative of many practical situations. The specimens are supported on two points and can be loaded in one or two points to obtain Three-Point Bending (3PB) [Olesen, 2001, Zhang and Li, 2004, Carpinteri and Brighenti, 2010] or Four-Point Bending (4PB) tests [Banthia and Trottier, 1995, Oh et al., 2007].

The results of a bending test can be represented by the load - vertical displacement curve [Gopalaratnam et al., 1991, Barros et al., 2005, Kim et al., 2008] or, in case of notched specimens, throughout the flexural load against the Crack (Tip or Mouth) Opening Displacement ($CTOD$ or $CMOD$, respectively) [Oliver et al., 2006, Park et al., 2010, Buratti et al., 2011]. The main purpose of the test is to determine the enhanced toughness of FRC compared to conventional concrete.

2.2 Experimental campaign

Several notched specimens were fabricated and tested for examining the mechanical properties of plain and fiber-reinforced concrete. Eleven mixtures, made with two different types of steel fibers and various amount of them, were considered. Moreover, a mixture of plain concrete without fibers was taken as reference and labeled as “REF”.

The tests were performed according to UNI-11039-1 [2003] for definitions, classification and designation and UNI-11039-2 [2003] for the test method. The most important aspects of the experimental campaign are described in the following.

2.2.1 Materials

The mixtures considered in the present research were made by employing a maximum aggregate size of 20 mm according to UNI-EN-12620 [2002] and UNI-11039-1 [2003] specifications, a constant cement content of 320 kg/m^3 and a water to cement ratio w/c of 0.51. Table 2.1 describes the mix of the reference concrete. Coarse natural aggregates were defined as $N1$ when the grain dimension ranges between 2 and 10 mm and $N2$ for the grain size from 10 to 20 mm, while fine aggregates (namely sand) had a maximum aggregate size equals to 2 mm as shown in Fig. 2.1. The aggregate grading of the reference concrete in comparison with the classical Fuller grain size distribution is proposed in Fig. 2.2.

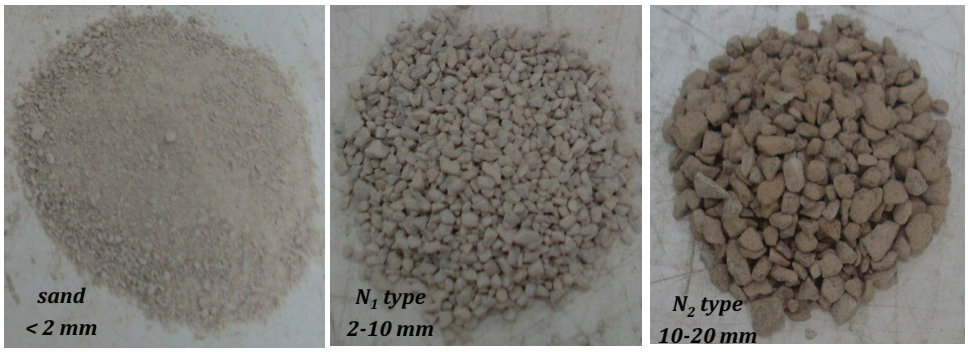

Figure 2.1: Fine and coarse aggregates employed in the experimental campaign.

Table 2.1: Mix design per cubic meter of the reference concrete.

Material	Density	Absorption	Dosage
Sand	2690 kg/m^3	1.20 %	1012 kg
Coarse agg. N1	2690 kg/m^3	0.70 %	134 kg
Coarse agg. N2	2690 kg/m^3	0.50 %	764 kg
Cement 42.5R	3030 kg/m^3	-	320 kg
Water	1000 kg/m^3	-	180 lt
Water absorption	1000 kg/m^3	-	17 lt
Superplasticizer	1050 kg/m^3	-	2.7 lt

Two types of steel reinforcements were employed in FRCs: Wirand Fibers FF3 type (namely “long fibers”) and Wirand Fibers FS7 type (“short fibers”) as shown in Fig. 2.3. Table 2.2 outlines the geometric and mechanical properties of fibers. The aspect ratio of the ‘long” and “short” steel fibers are 67 and 60, respectively, and the number of fibers/kg are 5700 and 16100, respectively.

Table 2.2: Geometric and mechanical properties.

Fibers	Diameter	Length	Tensile strength	Ultimate strain
Wirand FF3	0.75 mm	50 mm	> 1100 MPa	< 4%
Wirand FS7	0.55 mm	33 mm	> 1200 MPa	< 2%

2.2.2 Test method

Tests were carried out according to the procedures described in UNI-11039-2 [2003]. Particularly, prismatic $150 \times 150 \times 600\ mm^3$ specimens were tested in displacement control under four-point bending scheme as shown in Fig. 2.4(a). The main geometry of the adopted beams is given in Fig. 2.4(b).

Each specimen was preliminarily cracked through a vertical notch (approximately 2.0 mm wide) starting from the bottom surface of the sample and for a depth of $45mm$. The specimens were tested under displacement control (having displacement rate

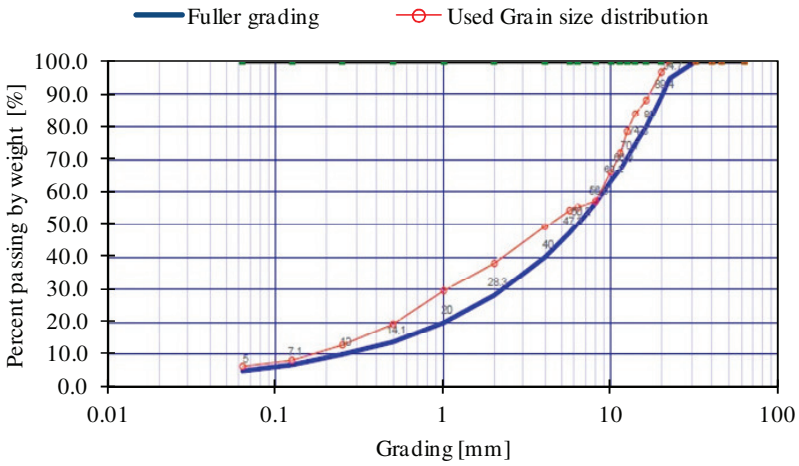

Figure 2.2: Grain size distribution of the "REF" mixture.

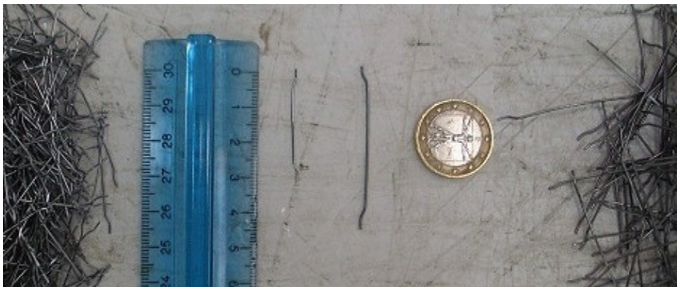

Figure 2.3: Fiber types: FS7 (short fiber) and FF3 (long fiber).

of 0.005 mm/min.) by recording the load by means of a load-cell as in Fig. 2.5(a), the displacements and the crack openings. The latter were measured by means of dedicated displacement transducers, as shown in Fig. 2.5(b), which measured the relative displacements of the two sides of the notch.

2.2.3 Test programme

Three series of specimens were tested (Table 2.3): plain (or reference) concrete specimens (labeled as "REF") and steel fiber-reinforced specimens with 0.5% and 1.0% of fiber content. All specimens were cast by using the concrete mix given in Table 2.1 with the exception of the superplasticizer. Its quantity was duly adjusted in each mixture with the aim to obtain a comparable workability measured by a slump value about equals to 150 mm. The prismatic concrete specimens were cured under water (100% humidity) at a constant temperature of 22^oC, for 28 days as in Fig. 2.6.

For each mixture, three beams were cast and tested in four-point bending. Moreover, three cubes of $150 \times 150 \times 150$ mm^3 (Fig. 2.7) were also cast in polyurethane molds [EN-12390-3, 2009] and then tested (in displacement control) for measuring the compressive

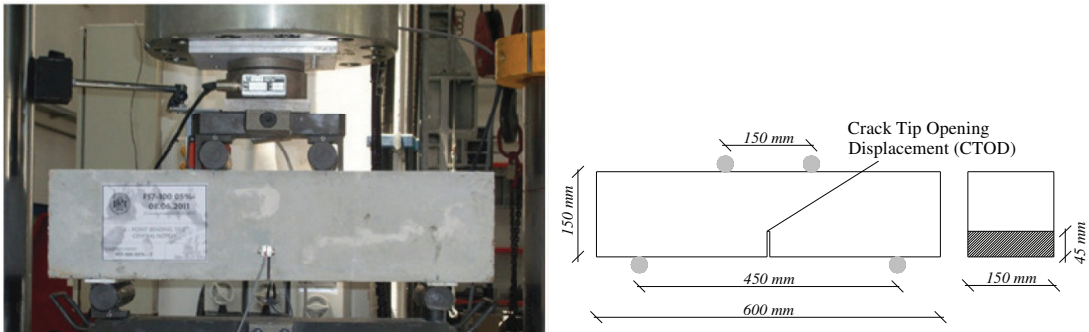

(a) (b)

Figure 2.4: Four-point bending test: (a) experimental set-up and (b) geometry of the notched beams.

(a) (b)

Figure 2.5: Four-point bending test: (a) load-cell and (b) crack opening transducers.

strength of the SFRCs at the time of testing. One of them (labeled as “white”) was extracted before the mixing of fibers with the aim to capture the actual contribution of fibers on the compressive response of the considered SFRC.

2.3 Experimental results

The main mechanical proprieties determined in the experimental tests are presented in the following subsections. At first, concrete specimens tested under compression will be given in subsection 2.3.1, then the experimental results on prismatic beams loaded in four-point bending tests will be detailed in the subsection 2.3.2.

2.3.1 Compression

The mechanical compressive results are summarized in Table 2.4 in terms of cube compressive strengths. The same table also reports the density mean values measured

Table 2.3: Considered mixture types of the experimental programme.

Mixture	Amount of Fibers	Long fibers (FF3)	Short fibers (FS7)
REF	-	-	-
S100 - 05	40 kg/m^3	-	100 %
S75 - 05	40 kg/m^3	25 %	75 %
LS50 - 05	40 kg/m^3	50 %	50 %
L75 - 05	40 kg/m^3	75 %	25 %
L100 - 05	40 kg/m^3	100 %	-
S100 -10	80 kg/m^3	-	100 %
S75 - 10	80 kg/m^3	25 %	75 %
LS50 - 10	80 kg/m^3	50 %	50 %
L75 - 10	80 kg/m^3	75 %	25 %
L100 - 10	80 kg/m^3	100 %	-

Table 2.4: Densities and cube compressive strengths measured in each mixture.

Mix Label	Density [kg/m^3]		R_c at 28 days [MPa]	
	white	SFRC	white	SFRC (mean of two)
REF	2371		42.59 (mean of three)	
S100-05	2376	2413	40.57	39.01
S75-05	2411	2439	41.79	40.88
LS50-05	2390	2430	44.80	43.36
L75-05	2410	2428	48.03	45.41
L100-05	2407	2443	43.70	42.74
S100-10	2353	2488	40.33	44.91
S75-10	2342	2458	38.44	39.54
LS50-10	2362	2448	43.77	40.87
L75-10	2391	2455	45.27	48.56
L100-10	2418	2519	38.54	49.39

in each considered mixture at hardened state.

In Fig. 2.9, the stress-strain curves obtained with white specimens and SFRCs having $\rho_f = 0.5\%$ and $\rho_f = 1.0\%$ of fiber volume contents are plotted. The vertical axis represents the average uniaxial stress measured as the applied compressive force subdivided to $150 \times 150\ mm^2$, being this latter the cross-sectional area of each cube. The horizontal axis is represented by the corresponding strain given as the prescribed vertical displacement subdivided to the specimen height ($150\ mm^2$).

The experimental results in Fig. 2.8 show very similar compressive strengths in both white and fiber-reinforced specimens. As largely accepted in literature [Nataraja et al., 1999, Fantilli et al., 2011], no more strength differences can be appreciated in terms of mean values of both white and steel fiber specimens (42.53 and 43.47 MPa, respectively), when these kinds of fiber volume contents are considered. The better performances of SFRCs compared to white samples can be appreciable only in terms of post-peak ductility when compressive failure processes are considered, as clearly observed in Fig. 2.9.

Figure 2.6: Underwater curing of specimens during 28 days at constant temperature of approximately 22^oC.

Figure 2.7: SFRC samples tested in compression.

A very high stability of the results in compression was obtained as demonstrated by the relative standard deviations

$$s_{n,white} = \sqrt{\frac{\sum_{i=1}^{n} \left(R_{c,i,white} - R_{c,m,white}\right)^2}{n}}$$
$$s_{n,SFRC} = \sqrt{\frac{\sum_{i=1}^{n} \left(R_{c,i,SFRC} - R_{c,m,SFRC}\right)^2}{n}} \tag{2.1}$$

measuring $s_{n,white} = 2.82\%$ and $s_{n,SFRC} = 3.41\%$ for white and SFRCs, respectively. In Eq. 2.1 $R_{c,i,white}$ and $R_{c,i,SFRC}$ represent the compressive strengths in white and SFRC specimens, above given in Table 2.4. Finally, $R_{c,m,white}$ and $R_{c,m,SFRC}$ deal with its mean values.

2.3.2 Four-point bending tests

Four-point bending tests were performed with the aim of characterizing the tensile post-cracking behavior of the considered SFRC mixture type. The UNI-11039-1 [2003]

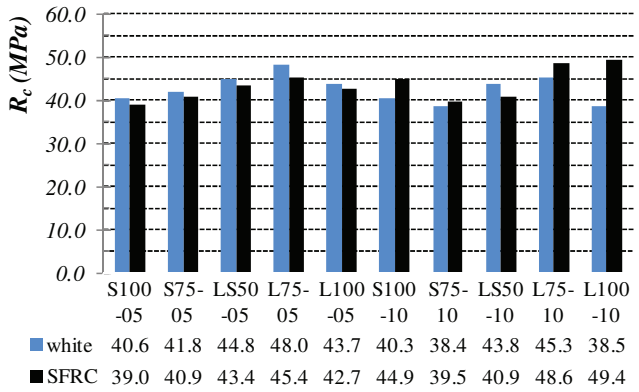

Figure 2.8: Cube compressive strengths of the SFRC probes [EN-12390-3, 2009].

and UNI-11039-2 [2003] standard guidelines were taken into account. Ten SFRC types, as well as plain reference concrete, were tested and compared. Fig. 2.10 shows the curves of the vertical load, P, versus the corresponding $CTODm$ curves, obtained in experimental tests. $CTODm$ represents the mean of the two opposite Crack Tip Opening Displacements ($CTODs$) registered by the transductor devices (Fig. 2.5b).

The experimental results demonstrate that fibers lead to a significant enhancement of the post-cracking toughness of the SFRC in both $\rho_f = 0.5\%$ and $\rho_f = 1.0\%$. The scatter observed in force-$CTODm$ curves was usually due to the non-regular distributions of fibers inside the specimens. A lower sensitivity emerged for compressive strength which was actually less influenced by fibers.

The first-crack strength values, f_{lf}, defining the post-cracking response of the SFRC composite, were defined by means of the following expression [UNI-11039-2, 2003]

$$f_{lf} = \frac{P_{lf} \cdot l}{b(h-a_0)^2} \tag{2.2}$$

where P_{lf} represents the first crack strength $[N]$; b, h and l are the width $[mm]$, height $[mm]$ and length $[mm]$ of the beam, respectively; a_0 $[mm]$ is the notch depth. Fig. 2.11 depicts the mean values of first crack strength and the two equivalent crack resistances, defined in standard $CTODm$ ranges, i.e. $[CTODm_0; CTODm_0 + 0.6\,mm]$ and $[CTODm_0 + 0.6; CTODm_0 + 3.0\,mm]$.

These quantities, known as $f_{eq_{(0-0.6)}}$ and $f_{eq_{(0.6-3.0)}}$, were defined as follows

$$\begin{aligned} f_{eq_{(0-0.6)}} &= \frac{l}{b(h-a_0)^2}\frac{U_1}{0.6} \\ f_{eq_{(0.6-3.0)}} &= \frac{l}{b(h-a_0)^2}\frac{U_2}{2.4} \end{aligned} \tag{2.3}$$

where U_1 and U_2 represent work capacity measures derived by means of the following

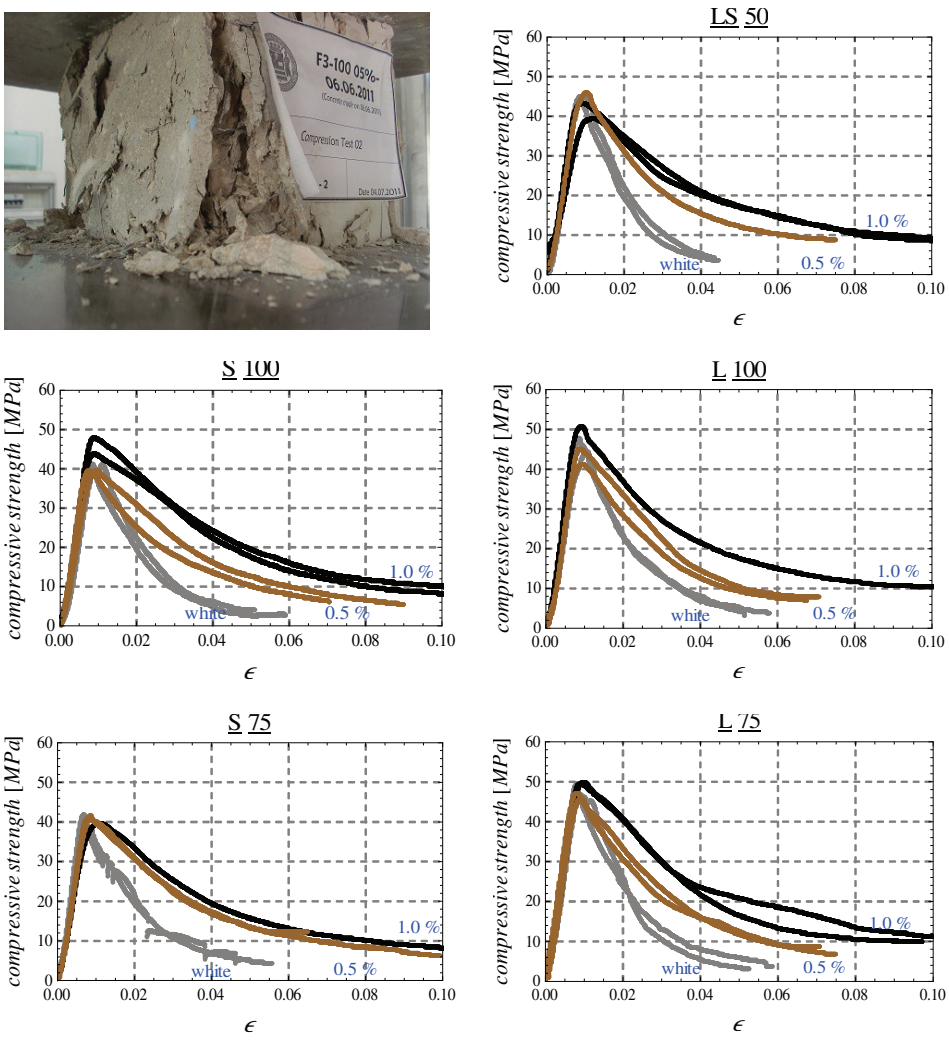

Figure 2.9: Compressive stress - strain curves of white concretes and SFRCs having $\rho_f = 0.5\%$ and $\rho_f = 1.0\%$ of fiber volume contents.

relations

$$U_1 = \int_{CTODm_0}^{CTODm_0+0.6} P[CTODm]dCTODm$$
$$U_2 = \int_{CTODm_0+0.6}^{CTODm_0+3.0} P[CTODm]dCTODm \tag{2.4}$$

The latter represent the area under the $P-CTODm$ curves between the range $[CTODm_0$; $CTODm_0 + 0.6\,mm]$ and $[CTODm_0 + 0.6$; $CTODm_0 + 3.0\,mm]$ for U_1 and U_2, respectively.

Fig. 2.12 shows the energy absorption values of each sample, calculated by means of the Eq. (2.4) while Fig. 2.11 reports the values of strength parameters defined

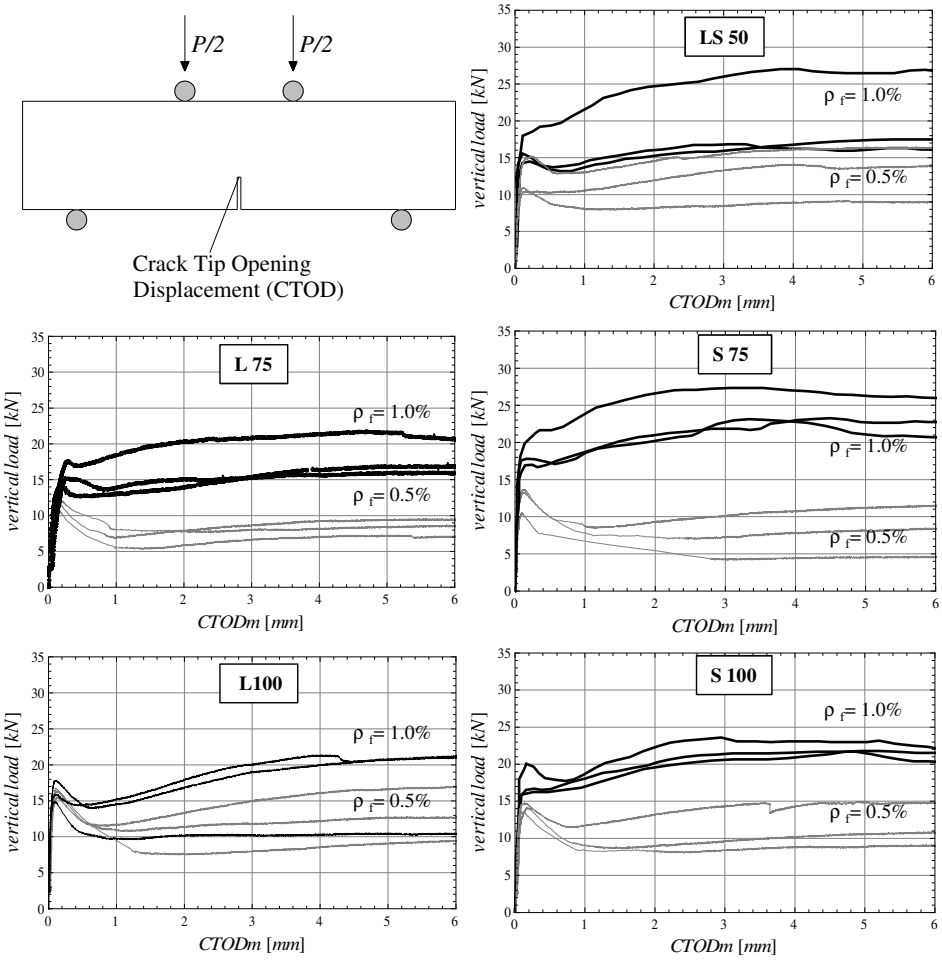

Figure 2.10: Vertical force - $CTODm$ curves: black lines refer to specimens with 1.0% of fiber volume content while grey lines indicate the 0.5% of fiber fraction.

by Eqs. (2.2) and (2.3) and measured for the various tested specimens. Keeping in mind the mechanical meaning of those parameters, Fig. 2.11 shows that specimens reinforced with 1.0% of steel fibers exhibit a significant hardening behavior in the flexural post-cracking regime, whereas a softening behavior was generally observed for specimens with 0.5% of fibers. It was demonstrated that a higher presence of short fibers increase the peak and post-peak strengths for small crack openings in cases with 1.0% of fiber contents. On the other hand, SFRC specimens with only presence of long fibers (L100-10) deals with a composite characterized by an immediately post-peak softening behavior in the first crack range $[CTODm_0; CTODm_0 + 0.6\,mm]$: i.e., $f_{eq_{(0-0.6)}} < f_{lf}$; then, a flexural re-hardening response takes place in the second crack range $[CTODm_0 + 0.6; CTODm_0 + 3.0\,mm]$: $f_{eq_{(0.6-3.0)}} > f_{eq_{(0-0.6)}}$. Finally, the results clarify that the composite with the best performance was represented by the S75-10 mixture.

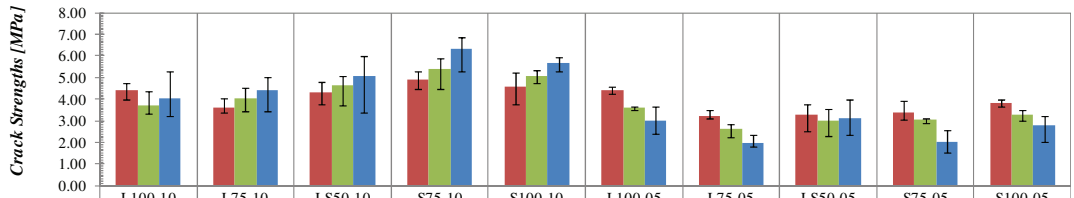

	L100-10	L75-10	LS50-10	S75-10	S100-10	L100-05	L75-05	LS50-05	S75-05	S100-05
flf	4.41	3.60	4.34	4.91	4.57	4.41	3.25	3.30	3.40	3.84
feq(0-0.6)	3.74	4.04	4.61	5.39	5.06	3.58	2.60	3.03	3.05	3.27
feq(0.6-3.0)	4.03	4.42	5.08	6.31	5.67	3.02	2.00	3.12	2.03	2.78

Figure 2.11: Comparisons between the first crack strength, f_{lf}, with the equivalent crack resistances, $f_{eq(0-0.6)}$ and $f_{eq(0.6-3.0)}$ [UNI-11039-2, 2003]. The vertical segments quantify the min-max range observed for each concrete mix.

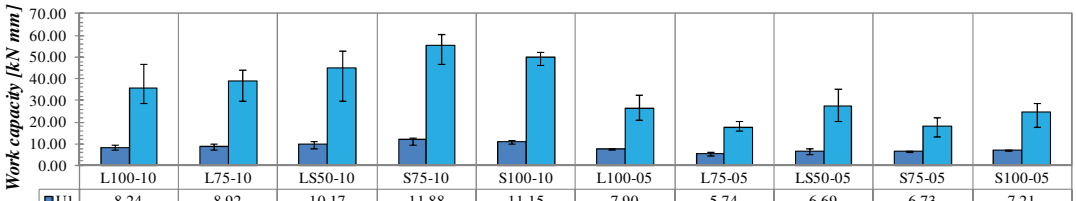

	L100-10	L75-10	LS50-10	S75-10	S100-10	L100-05	L75-05	LS50-05	S75-05	S100-05
U1	8.24	8.92	10.17	11.88	11.15	7.90	5.74	6.69	6.73	7.21
U2	35.51	38.97	44.82	55.61	49.98	26.60	17.65	27.55	17.90	24.55

Figure 2.12: Energy absorption measures U_1 and U_2 according to UNI-11039-2 [2003]. The vertical segments quantify the min-max range observed for each concrete mix.

Experimental results on SFRC with low fiber contents (0.5%) were characterized by high sensitivity to the number of fibers crossing the cracked section. It follows that a lower stability of the experimental results can be recognized. Furthermore, as for the 1.0% types, the presence of short fibers generates some enhancements of the post-peak strength for small cracks (as shown in Fig. 2.11 for the cases of LS50-05, S75-05 and S100-05) but these residual strengths rapidly decrease since fibers were debonded from the cementitious matrix.

Further ductility indices can be considered as objective measurements of the fiber bridging effect. Based on the UNI-11039-2 [2003] code, the following ductility measures were calculated

$$D_0 = f_{eq\,(0-0.6)} / f_{lf} \tag{2.5}$$

and

$$D_1 = f_{eq\,(0.6-3.0)} / f_{lf} \tag{2.6}$$

Fig. 2.13 depicts the values of ductility indices defined by Eqs. (2.5) and (2.6) and measured for the various tested beams.

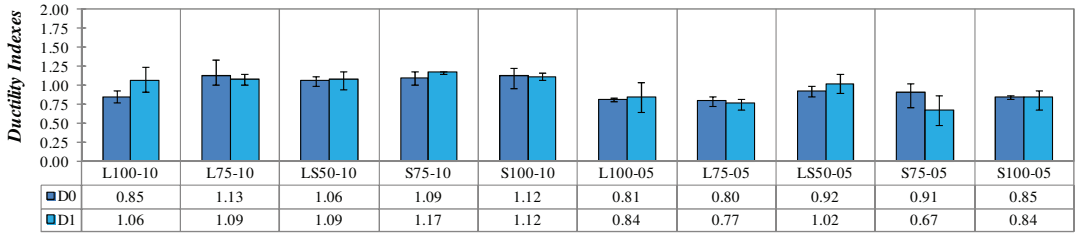

	L100-10	L75-10	LS50-10	S75-10	S100-10	L100-05	L75-05	LS50-05	S75-05	S100-05
D0	0.85	1.13	1.06	1.09	1.12	0.81	0.80	0.92	0.91	0.85
D1	1.06	1.09	1.09	1.17	1.12	0.84	0.77	1.02	0.67	0.84

Figure 2.13: Indices of the ductility according to UNI-11039-2 [2003]. The vertical segments quantify the min-max range observed for each concrete mix.

Class	$F_{2.0}$	$F_{2.5}$	$F_{3.0}$	$F_{3.7}$	$F_{4.5}$	$F_{5.5}$	$F_{6.5}$	$F_{7.7}$	$F_{9.0}$
First Crack Resistance (Minimum Value)	2.0	2.5	3	3.7	4.5	5.5	6.5	7.7	9

Ductility Indices	**Ductility Class**						
(Minimum Value)	D_{S0}	D_{S1}	D_{S2}	D_P	D_{H0}	D_{H1}	D_{H2}
D_0	< 0.5	≥ 0.5	≥ 0.7	≥ 0.9	≥ 1.1	≥ 1.3	≥ 1.55
D_1	≥ 0.3	≥ 0.5	≥ 0.7	≥ 0.9	≥ 1.1	≥ 1.3	≥ 1.55
Type of response	**crack-softening**			**perfectly plastic**	**crack-hardening**		

Figure 2.14: Classifications based on the first crack resistances and the ductility indices by UNI-11039-1 [2003] code.

According to the classification of UNI-11039-1 [2003] given in Fig. 2.14, when the specific ductility index (referred to the considered $CTODm$ range) is greater than the unit, the material is considered as a crack-hardening medium under flexure; when that indices are approximatively equal to 1 the SFRC responds in a plastic post-cracking behavior. If D_0 or $D_1 \leq 1$ the post-cracking response is mainly softening. In practical designs, minimum mechanical performances are required to SFRC composites. Particularly, only if $f_{eq_{(0-0.6)}} \geq 0.5 \cdot f_{lf}$ or $D_0 \geq 0.5$ the post-cracking resistance can be considered. When the post-cracking behavior does not comply with the above limits, it should be neglected in design calculations.

2.4 Closure chapter and concluding remarks

The four-point bending behavior of notched FRC beams was investigated in this section. The present experimental campaign focused on investigating the possible influence of combining two different types of fibers on the resulting properties of FRC. Thus, two different amounts of hooked-end steel fibers were employed in the concrete mixes of tested specimens and five combinations of long/short fibers were considered for each of them.

The following observations emerged by analysing the experimental results:

- the first-crack strength and the whole post-cracking behavior were mainly influenced by the amount of fibers: crack-softening response was observed for all specimens with $\rho_f = 0.5\%$, whereas a rather hardening behavior characterized the post-cracking response of specimens with $\rho_f = 1.0\%$;
- slight influence of fiber combination can be observed in terms of first-crack strength: this parameter is almost irrelevant in the case of low amount of fibers, while results in a slightly more regular trend in the case of $\rho_f = 1.0\%$ fibers;
- the toughness indices determined for all specimens point out that no clear influence can be recognized to fiber combination in affecting the overall response of FRC in the post-cracking regime.

As a matter of fact, the very low influence of fiber combination on the observed FRC behavior was the key conclusion of the experimental activity. However, it is worth underlining that this was not a general conclusion, as in the case under consideration, the two "different" fibers were characterized by the same material, similar geometric details (i.e., hooked ends) and rather close values of aspect ratios. Thus, the possible synergic effect of combining different fibers should be investigated by considering two (or more) types of really "more different" fibers (i.e., in terms of materials, geometric and detailing).

3 Zero-thickness interface model for failure behavior of fiber-reinforced cementitious composites

This chapter deals with the formulation of a zero-thickness interface model conceived within the general framework of the discrete-crack approach and aimed at simulating the mechanical response of Fiber-Reinforced Cementitious Composites (FRCCs). Following a cohesive-frictional interface proposal, already available in scientific literature for plain concrete, the formulation of an interface constitutive model was further developed and extended to capture the key mechanical phenomena controlling the FRCC behavior. An original approach was introduced for reproducing the complex influence of fibers on cracking phenomena of concrete/mortar matrix. Particularly, the proposal takes into account both the bond-slip strength and dowel mechanisms generated by fibers crossing the concrete cracks.

This novel interface model for FRCC was mainly based on flow theory of plasticity and fracture energy concepts to control the energy release during cracking processes under both fracture mode I and/or II. The constitutive proposal represents an extension of the previous interface formulation for plain concrete approached by Carol et al. [1997] and by Lopez et al. [2008a,b] to take into account the interaction between cement/mortar and steel fibers. Particularly, fiber reinforcements, here considered to be embedded into the plane of interfaces, were explicitly incorporated by means of the well-known "Mixture Theory" by Trusdell and Toupin [1960], following the approach used in Manzoli et al. [2008].

In this chapter, section 3.1 briefly reports the main issues of the interface model for FRCC outlining the main assumptions utilized in the constitutive proposal. After this, section 3.2 summarizes an overview of "Mixture Theory" concepts [Trusdell and Toupin, 1960] and its use on the given discontinuous based proposal. The interface model, aimed in principle at reproducing the post-peak softening behavior due to crack propagations in plain concrete, is outlined in section 3.3. It was formulated by means of an incremental approach, which is similar to the one usually adopted in the classical flow theory of plasticity. A novel bond-slip model for simulating the axial effect of fibers on concrete cracks is presented in section 3.4. Then, the composite action between

concrete and fiber reinforcements is also completed by considering the dowel fiber effect as given in 3.5. Some concluding remarks of this chapter are finally reported in section 3.6.

3.1 Interface constitutive model for FRCC

The present constitutive model for FRCC interfaces, based on an application of the "Mixture Theory", includes three internal "components" listed below:

1. a *fracture energy-based cracking formulation for plain mortar/concrete interfaces* which relates normal and tangential stress components with the corresponding relative displacements in the plane of the interface. Its maximum strength criterion was defined according to the three-parameter hyperbolic failure surface by Carol et al. [1997]. Main features of this model are summarized in section 3.3.
2. a*fiber bond-slip formulation* to describe the uniaxial inelastic behavior of steel fibers crossing the interfaces by means of an elastoplastic model as indicated in section 3.4.
3. a *formulation for fiber dowel action* based on elastic foundation concepts to obtain the dowel force-displacement relationship. Further details of the constitutive model are proposed in section 3.5.

For the sake of simplicity, the present model was formulated in 2D, as Lopez et al. [2008a,b] did in a similar proposal for simulating the meso-scale fracture behavior on plain concrete. Particularly, they demonstrated that the results obtained in 2D successfully reproduced the experimental behavior under several basic stress states.

3.2 Outline of the Mixture Theory

3.2.1 Composite material model

According to the fundamental assumptions of the Mixture Theory formulated in Truesdell and Toupin [1960], each infinitesimal volume of the mixture is ideally and simultaneously occupied by all mixture constituents (i.e. "phases"), that are subjected to the same displacement fields. Consequently, the composite stress is obtained from the addition of the mixture stresses weighted by the volume fraction of each mixing constituent.

The composite schematization of a considered steel FRCC panel, as in Fig. 3.1, takes into account three main phases: (i) coarse aggregates, (ii) cementitious matrix or mortar and (iii) steel fibers. The mechanical properties of the considered composite material

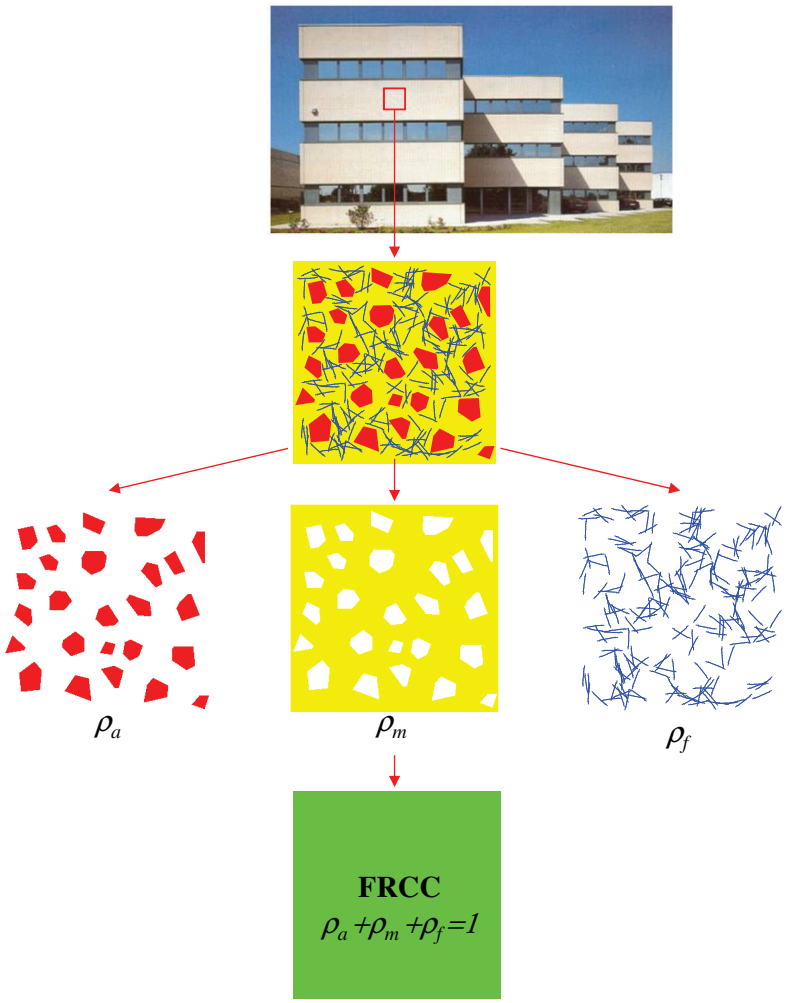

Figure 3.1: Main assumptions of fibrous concretes in the framework of the well-known "Mixture Theory" [Trusdell and Toupin, 1960].

can be defined according to the "Mixture Theory" above mentioned. For instance, a generic mechanical parameter of the composite can be derived as

$$p_c = \rho_a p_a + \rho_m p_m + \rho_f p_f \tag{3.1}$$

being p_c the considered mechanical parameter (i.e., the elastic modulus or the Poisson's ratio) while $\rho_\#$ refers to the volume fraction of each # component (Fig. 3.2): i.e., $\# = c$ for the considered composite, $\# = a$ for coarse aggregates, $\# = m$ for matrix and $\# = f$ for fibers.

In a similar way, let us consider a generic relative displacement vector at the interface $\boldsymbol{u}$ (Fig. 3.3), the axial displacement of the single fiber is given by $u_N = \boldsymbol{u} \cdot \boldsymbol{n}_N$ (being $\boldsymbol{n}_N$ the fiber direction), while in the transversal direction $u_T = \boldsymbol{u} \cdot \boldsymbol{n}_T$. Thereby, $\boldsymbol{n}_T$ is a

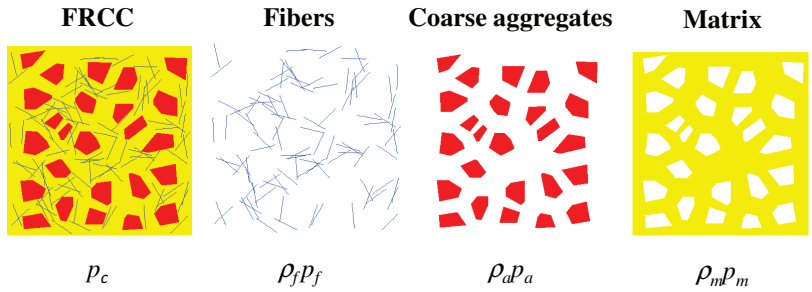

Figure 3.2: Mixture components of the FRCC continuum material.

unitary vector orthogonal to $\boldsymbol{n}_N$. Consequently, the axial and tangential fiber strains can be derived as $\varepsilon_N = u_N/l_f$ and $\gamma_T = u_T/l_f$, respectively, being l_f the fiber length (each fiber was ideally assumed to cross the interface fracture surface at its mid-length, i.e. at $l_f/2$).

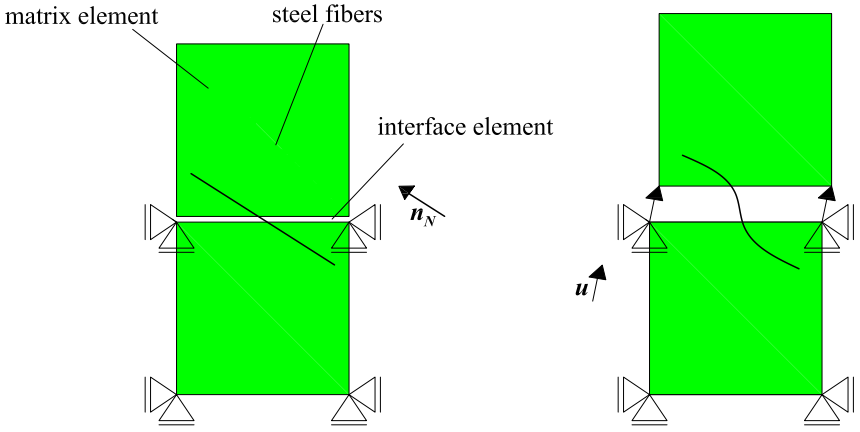

Figure 3.3: Schematic configuration of an interface element crossed by one fiber.

The interface constitutive model was formulated in incremental form, as generally assumed for the flow theory of plasticity. According to the hypotheses of the composite model, the rate of the stress vector at the interface $\dot{\boldsymbol{t}} = [\dot{\sigma}, \dot{\tau}]^t$ (being σ and τ the normal and tangential interfacial composite stresses, respectively), was calculated by means of the following $\rho_{\#}$-weighted sum

$$\dot{\boldsymbol{t}} = w[\rho_i]\dot{\boldsymbol{t}}^i + \sum_{f=0}^{n_f} w[\rho_f]\left(\dot{\sigma}_f[\dot{\varepsilon}_N]\,\boldsymbol{n}_N + \dot{\tau}_f\left[\dot{\gamma}_T\right]\boldsymbol{n}_T\right). \tag{3.2}$$

The indices i and f refer to interface and fiber, respectively; σ_f and τ_f mean the bond-slip force and dowel effect of the single considered fiber; n_f is the number of fibers crossing the interface. The weighting function of the plain interfaces $w[\rho_i]$ was generally assumed as unitary, while $w[\rho_f]$ takes into account the effectiveness decay of fiber contributions to the total stress as the fiber content increases. It can be formulated as a function of the total fiber content ρ_f,

$$w[\rho_f] = \left[1 - \alpha_f \rho_f\right] \rho_{f,1} \tag{3.3}$$

being $\rho_{f,1}$ the fiber content of a single reinforcement while α_f is a material parameter to be calibrated.

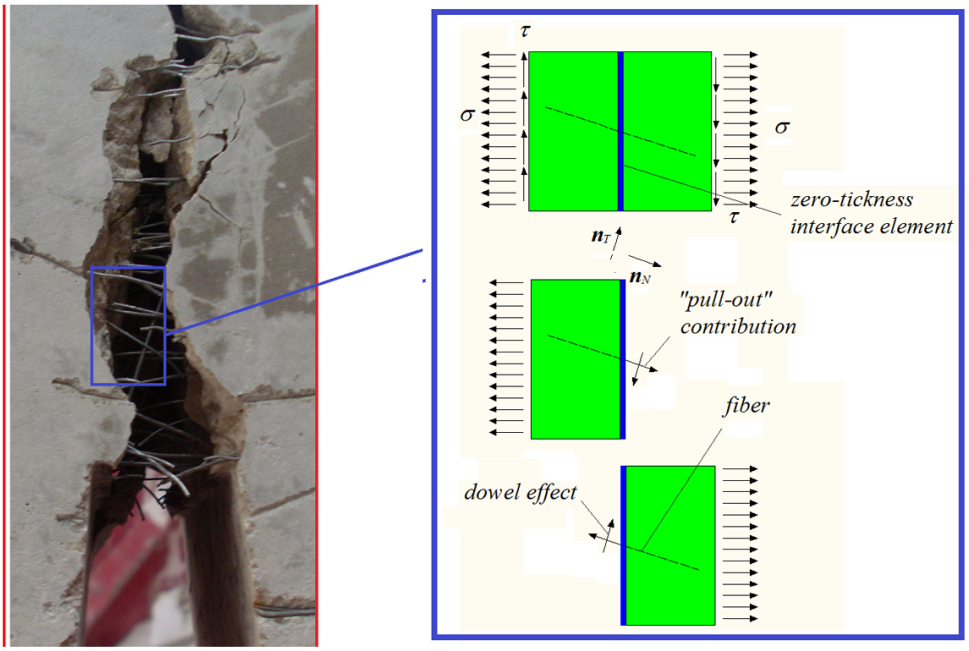

Figure 3.4: Fiber effects on the plane of the zero-thickness interface

Fiber bridging effects, formulated herein in terms of bond-slip and dowel mechanisms, are schematically represented in the interface plane as in Fig. 3.4.

The number of fibers per interface, radially distributed in the crack plane, was explicitly considered in the present work. No random distribution of fibers was considered in this formulation. This could be handled within the framework of well established statistical procedures. Particularly, the present interface model deals with the schemes given in Fig. 3.5, in which a regular iso-angular spacing between fibers crossing the interface was considered.

The evaluation of the total number of fibers which cross the interface was essentially

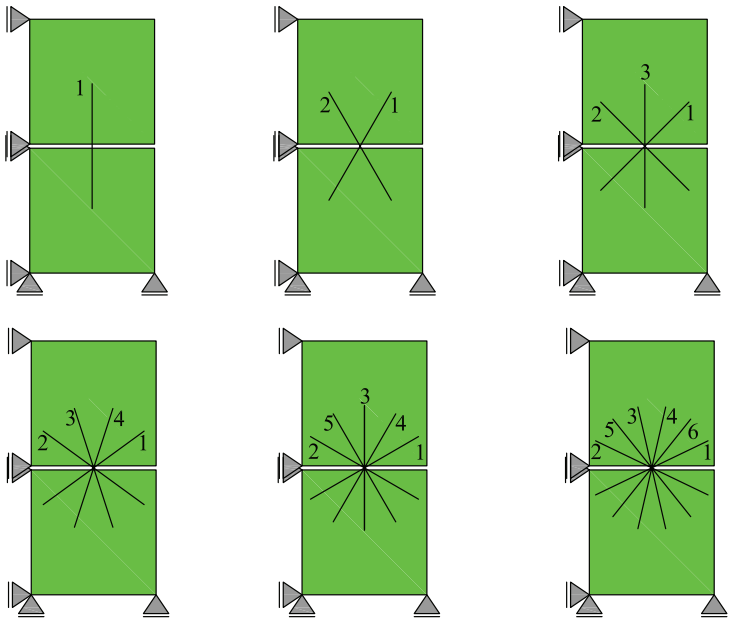

Figure 3.5: Considered fibers crossing the interface: as example the cases of 1, 2, 3, 4, 5 and 6 reinforcements are presented.

founded on the relationship proposed by Krenchel [1975]

$$n_f = \alpha_{\vec{N}} \frac{\rho_f}{A_f} A_i \tag{3.4}$$

where ρ_f is the fiber content, A_f and A_i are the cross-sectional area of a single fiber and the area of the considered interface, respectively.

The calculation of the orientation factor $\alpha_{\vec{N}}$ was investigated for many researchers [Krenchel, 1975, Soroushian and Lee, 1990, Li et al., 1991, Stroeven, 1999, Kooiman, 2000, Dupont and Vandewalle, 2005]. The most recent proposal outlined by Dupont and Vandewalle [2005] was taken as reference in the following of this work.

3.2.2 Constitutive models of each single phase

The relationship between stresses and relative displacements, developed throughout the generic fracture interface, can be formulated in the following incremental form, as usual in classical plasticity-based model

$$\dot{\boldsymbol{t}} = \boldsymbol{E}^{ep} \cdot \dot{\boldsymbol{u}} \tag{3.5}$$

being $\dot{\boldsymbol{t}}$ the rate vector of the composite joint stresses and $\dot{\boldsymbol{u}}$ the interface displacement rate vector, respectively.

As previously proposed, the composite interface was based on the consideration that each infinitesimal surface is ideally and simultaneously occupied by all components. Each component is subjected to the same displacement field while the corresponding composite stress is given by the weighted sum of the component s tresses. For the same assumption the constitutive tangent operator, $\boldsymbol{E}^{ep}$, is given by the following expression

$$\boldsymbol{E}^{ep} = w[\rho_i]\boldsymbol{C}^{ep} + \sum_{f=0}^{n_f} w[\rho_f]\left(\frac{E_f^{ep}}{l_f}\boldsymbol{n}_N \otimes \boldsymbol{n}_N + \frac{G_f^{ep}}{l_f}\boldsymbol{n}_T \otimes \boldsymbol{n}_T\right) \tag{3.6}$$

based on the weighting functions $w[\rho_\#]$ ($\# = i, f$) of Eq. (3.3), where $\rho_\#$ represents the volume fraction of the # composite phase, $\boldsymbol{n}_N \otimes \boldsymbol{n}_N$ and $\boldsymbol{n}_T \otimes \boldsymbol{n}_T$ identify the second order dyadic tensor constructed on the fiber direction and its orthogonal of a generic fiber with respect to the global Cartesian reference system.

The tangent operators $\left[\boldsymbol{C}^{ep}, E_f^{ep}, G_f^{ep}\right]$ of Equation [3.6] were defined as follows:

- *for the fracture-based plain interface model*:

$$\boldsymbol{C}^{ep} = \partial \boldsymbol{t}^i / \partial \boldsymbol{u}, \tag{3.7}$$

  formulated in terms of normal (σ_N) and shear (σ_T) stresses ($\boldsymbol{t}^i = [\sigma_N, \sigma_T]^t$) of plain concrete joints corresponding to the relative displacements $\boldsymbol{u}$ (further details are explained in section 3.3);

- *for the bond-slip fiber-to-concrete model*:

$$E_f^{ep} = d\sigma_f / d\varepsilon_N, \tag{3.8}$$

  being σ_f and ε_N the axial stress and strain of fibers at cracks (ideally assuming that each fiber crosses the interface fracture surface at its mid-length, i.e. $l_f/2$); a closed-form analytical constitutive model for the debonding fiber process (in terms of $\sigma_f - \varepsilon_N$ law) was considered (see section 3.4 for further details);

- *for the dowel action model*:

$$G_f^{ep} = d\tau_f / d\gamma_T, \tag{3.9}$$

  in which the elastic branch of the shear stress-strain law ($\tau_f - \gamma_T$) was derived by modeling the fiber embedded into the cement matrix as a Winkler foundation beam (as presented in section 3.5).

3.3 Fracture energy-based model for plain mortar/concrete interface

This section summarizes the interface model originally proposed in Gens et al. [1988] for application in soil-mechanics and extended to plain concrete by Carol et al. [1997]. The constitutive equation, in the framework of the rate-independent plasticity theory, can be presented in incremental form as

$$\dot{\boldsymbol{u}} = \dot{\boldsymbol{u}}^{el} + \dot{\boldsymbol{u}}^{cr} \tag{3.10}$$

$$\dot{\boldsymbol{u}}^{el} = \boldsymbol{C}^{-1} \cdot \dot{\boldsymbol{t}}^{i} \tag{3.11}$$

$$\dot{\boldsymbol{t}}^{i} = \boldsymbol{C} \cdot (\dot{\boldsymbol{u}} - \dot{\boldsymbol{u}}^{cr}) \tag{3.12}$$

where $\dot{\boldsymbol{u}} = [\dot{u}, \dot{v}]^t$ is the rate of the relative joint displacement vector, decomposed into elastic and plastic components, $\dot{\boldsymbol{u}}^{el}$ and $\dot{\boldsymbol{u}}^{cr}$, respectively. $\boldsymbol{C}$ defines a fully uncoupled normal/tangential elastic stiffness matrix

$$\boldsymbol{C} = \begin{pmatrix} k_N & 0 \\ 0 & k_T \end{pmatrix} \tag{3.13}$$

while $\dot{\boldsymbol{t}}^{i} = [\dot{\sigma}_N, \dot{\sigma}_T]^t$ is the incremental stress vector defined in the interface coordinates, being σ_N and σ_T the normal and shear components, respectively.

The vector of the plastic displacement rate, according to a non-associated flow rule, was defined as

$$\dot{\boldsymbol{u}}^{cr} = \dot{\lambda} \boldsymbol{m} \tag{3.14}$$

where $\dot{\lambda}$ is the non-negative plastic multiplier derived by means of the classical Kuhn-Tucker loading/unloading and consistency conditions which take the following form

$$\begin{array}{lll} \dot{\lambda} \geq 0, \quad f \leq 0, \quad \dot{\lambda} \cdot f = 0 & \text{Kuhn} - \text{Tucker} \\ \dot{f} = 0 & \text{Consistency} \end{array} \tag{3.15}$$

where $f = f[\sigma_N, \sigma_T]$ defines the yield condition of the model on the bases of the following three-parameter formulation (outlining the hyperbola represented in Fig. 3.6)

$$f = \sigma_T^2 - (c - \sigma_N \tan\phi)^2 + (c - \chi \tan\phi)^2. \tag{3.16}$$

The tensile strength χ (vertex of the hyperbola), the cohesion c and the frictional angle ϕ are material parameters needed for identifying the interface model. Eq. (3.16) outlines two principal failure modes:

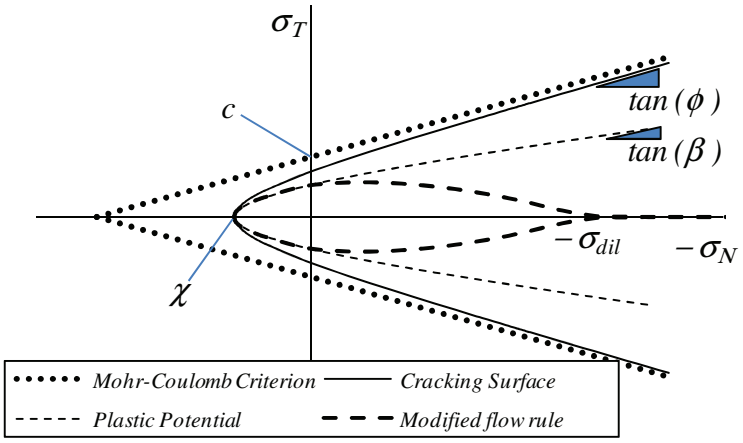

Figure 3.6: Failure hyperbola by Carol et al. [1997], Mohr-Coulomb surface, plastic potential and the modified flow rule according to Eq. (3.19) of the interface model.

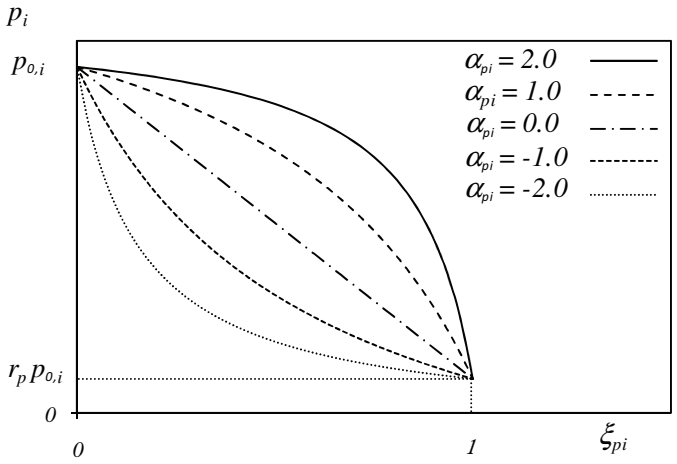

Figure 3.7: Evolution law of the interface fracture parameters.

- *Mode I type of fracture*: maximum strength surface is reached along its horizontal axis;
- *asymptotic Mode II type of fracture*: maximum strength surface is reached on its asymptotic region in which the hyperbola approaches a Mohr-Coulomb criterion (see Fig. 3.6).

Eq. (3.14) describes a general non-associated flow rule which controls the direction $\boldsymbol{m}$ of interface fracture displacements. In the present formulation the non-associated plastic direction is described by means of the transformation matrix operator $\boldsymbol{A}$

$$\boldsymbol{m} = \boldsymbol{A} \cdot \boldsymbol{n} \tag{3.17}$$

being

$$\boldsymbol{n} = \frac{\partial f}{\partial \boldsymbol{t}^i} = \left[\frac{\partial f}{\partial \sigma_N}, \frac{\partial f}{\partial \sigma_T}\right]^t = \left[2\tan\phi(c - \sigma_N \tan\phi), 2\sigma_T\right]^t \tag{3.18}$$

and

$$\boldsymbol{A} = \begin{cases} \begin{pmatrix} \frac{\tan\beta}{\tan\phi} & 0 \\ 0 & 1 \end{pmatrix} & \text{if} \quad \sigma_N \geq 0 \\ \begin{pmatrix} \left[1 - \frac{|\sigma_N|}{\sigma_{dil}}\right]\frac{\tan\beta}{\tan\phi} & 0 \\ 0 & 1 \end{pmatrix} & \text{if} \quad -\sigma_{dil} \leq \sigma_N < 0 \\ \begin{pmatrix} 0 & 0 \\ 0 & 1 \end{pmatrix} & \text{if} \quad \sigma_N < -\sigma_{dil} \end{cases} \tag{3.19}$$

where $\tan\beta$ is the dilation angle of the plastic potential, represented in Fig. 3.6: $0 \leq \tan\beta \leq \tan\phi$. Thereby, the parameter σ_{dil} represents the normal stress at which the dilatancy vanishes, see in Carol et al. [1997] and Lopez [1999].

3.3.1 Single internal state variable

The fracture work spent w_{cr} during the opening-sliding fracture process governs the evolutions of the material parameters χ, c and $\tan\phi$ in softening regime of the interface constitutive law. The variable w_{cr} defines the necessary amount of released energy to open a single crack in tensile and/or shear fracture mode due to normal σ_N and/or tangential σ_T joint stresses, respectively.

Hence the incremental fracture work spent $\dot{w}_{cr}$, in a generic fracture process, was defined as follows [Carol et al., 1997]

$$\dot{w}_{cr} = \sigma_N \cdot \dot{u}^{cr} + \sigma_T \cdot \dot{v}^{cr}, \ if\ \sigma_N \geqslant 0 \tag{3.20}$$

$$\dot{w}_{cr} = \left[\sigma_T - |\sigma_N|\, tan(\phi)\right] \cdot \dot{v}^{cr}, \ if\ \sigma_N < 0 \tag{3.21}$$

while the total dissipated work was obtained by integrating the fracture work increments during fracture process time frame.

3.3.2 Evolution laws of the fracture surface

In this formulation, the decay function proposed in Caballero et al. [2008] was considered for all internal parameters of the yield condition, see Eq. (3.16), as

$$p_i = \left[1 - \left(1 - r_p\right) S[\xi_{p_i}]\right] p_{0i} \tag{3.22}$$

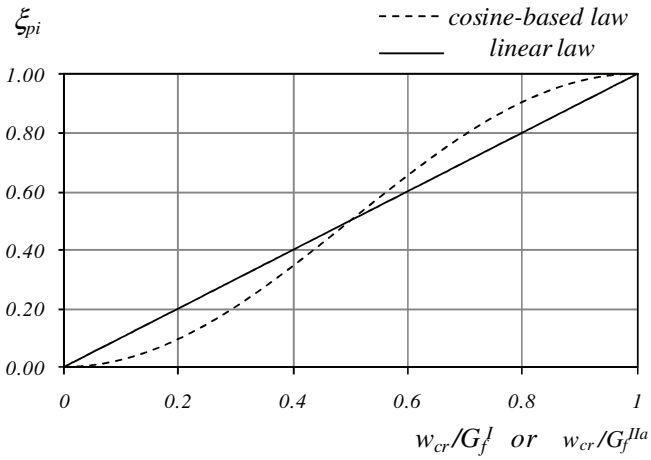

Figure 3.8: Cosine-based vs. linear law related to the ratio between the work spent w_{cr} and the available energies G_f^I or G_f^{IIa}.

with p_i alternatively equals to χ, c or $tan\phi$. Last equation defines the typical internal parameter degradation law from its maximum or initial value, $p_i = p_{0i}$, to the residual one, $p_i = r_p p_{0i}$, in terms of the scaling function $S[\xi_{p_i}]$, where

$$S[\xi_{p_i}] = \frac{e^{-\alpha_{p_i}}\xi_{p_i}}{1+(e^{-\alpha_{p_i}}-1)\xi_{p_i}}. \tag{3.23}$$

Thereby, parameter α_{p_i} controls the decay form of the internal parameter as shown in Fig. 3.7, while the non-dimensional variable ξ_{p_i} introduces the influence of the ratio between the current fracture work spent and the available fracture energy, in the decay function Eq. (3.22) as

$$\xi_\chi = \begin{cases} \frac{1}{2}\left[1-cos\left(\frac{\pi w_{cr}}{G_f^I}\right)\right] & \text{if } w_{cr} \le G_f^I \\ 1 & \text{otherwise} \end{cases} \tag{3.24}$$

$$\xi_c = \xi_{\tan\phi} = \begin{cases} \frac{1}{2}\left[1-cos\left(\frac{\pi w_{cr}}{G_f^{IIa}}\right)\right] & \text{if } w_{cr} \le G_f^{IIa} \\ 1 & \text{otherwise} \end{cases} \tag{3.25}$$

according to the C^1 continuity function proposed in Caballero et al. [2008]. Figs. 3.8 and 3.9 show typical curves obtained with Eqs. (3.24) or (3.25) and the respective derivates compared to the original linear proposal in Carol et al. [1997].

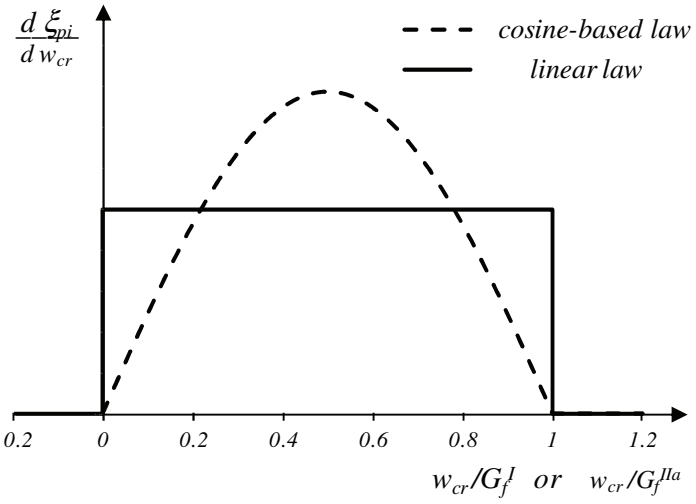

Figure 3.9: Comparison of the derivates between the cosine-based law against the linear rule.

3.3.3 An overview of the interface model for plain concrete/mortar

In the above subsections a rate-independent fracture-based plasticity model has been presented and the main aspects of the interface formulation has completely been detailed. This final subsection is aimed at compactly reporting all the interface ingredients above given. Particularly, in Table 3.1 the adopted yield criterion, the flow rule, the cracking work evolution laws and the well-known Kuhn-Tucker and consistency conditions are compactly reported.

Table 3.1: Overview of the interface model for Plain Concrete/Mortar

	Fracture - based energy interface model
Constitutive equation	$\dot{\boldsymbol{t}}^i = \boldsymbol{C}\cdot\left(\dot{\boldsymbol{u}} - \dot{\boldsymbol{u}}^{cr}\right)$ $\dot{\boldsymbol{u}} = \dot{\boldsymbol{u}}^{el} + \dot{\boldsymbol{u}}^{cr}$
Yield condition	$f\left(\boldsymbol{t}^i,\kappa\right) = \sigma_T^2 - (c - \sigma_N \tan\phi)^2 + (c - \chi\tan\phi)^2$
Flow rule	$\dot{\boldsymbol{u}}^{cr} = \dot{\lambda}\,\boldsymbol{m}$ $\boldsymbol{m} = \boldsymbol{A}\cdot\boldsymbol{n}$
Cracking work evolution	$\dot{\kappa} = \dot{w}_{cr}$ $\dot{w}_{cr} = \sigma_N\cdot\dot{u}^{cr} + \sigma_T\cdot\dot{v}^{cr}$ if $\sigma_N \geq 0$ $\dot{w}_{cr} = \left[\sigma_T - \lvert\sigma_N\rvert\, tan(\phi)\right]\cdot\dot{v}^{cr}$ if $\sigma_N < 0$
Evolution law	$p_i = \left[1 - \left(1 - r_p\right) S[\xi_{p_i}]\right] p_{0i}$
Kuhn - Tucker / Consistency	$\dot{\lambda} \geq 0, \quad f\left(\boldsymbol{t}^i,\kappa\right) \leq 0, \quad \dot{\lambda}\, f\left(\boldsymbol{t}^i,\kappa\right) = 0, \quad \dot{f}\left(\boldsymbol{t}^i,\kappa\right) = 0$

3.4 One-dimensional bond-slip model for fibers

This section deals with the proposed one-dimensional plasticity model for the steel fiber stress-strain response to account in the composite model given in Eq. (3.2). Particularly, the total strain rate $\dot{\varepsilon}_N$ can be decomposed into elastic ($\dot{\varepsilon}_N^{el}$) and plastic ($\dot{\varepsilon}_N^{pl}$) components as

$$\dot{\varepsilon}_N = \dot{\varepsilon}_N^{el} + \dot{\varepsilon}_N^{pl} \tag{3.26}$$

and the total stress rate results

$$\dot{\sigma}_f = E_f(\dot{\varepsilon}_N - \dot{\varepsilon}_N^{pl}) \tag{3.27}$$

where E_f represents the uniaxial elastic modulus which encompasses both the uniaxial response of the steel fiber and the bond-slip effect of the short steel reinforcement in mortar/concrete interfaces. In case of isotropic hardening, the yield condition takes the following form

$$f_f = |\sigma_f| - (\sigma_{y,f} + Q_f) \leq 0 \tag{3.28}$$

with $\sigma_{y,f} \geq 0$ the initial yield stress and Q_f the internal softening variable in post-elastic regime. Its evolution law was defined as

$$\dot{Q}_f = \dot{\lambda}_f H_f \tag{3.29}$$

while that of the plastic strain rate results

$$\dot{\varepsilon}_N^{pl} = \dot{\lambda}_f \partial f_f / \partial \sigma_f = \dot{\lambda}_f sign[\sigma_f] \tag{3.30}$$

being $\dot{\lambda}_f$ the plastic multiplier and H_f is the softening module.

Then, Kuhn-Tucker loading/unloading conditions were given by

$$\dot{\lambda}_f \geq 0,\ f_f(\sigma_f, Q_f) \leq 0,\ \dot{\lambda}_f f_f(\sigma_f, Q_f) = 0 \tag{3.31}$$

imposing $\dot{f}_f(\sigma_f, Q_f) = 0$, the persistent (consistency) under loading condition.

The constitutive stress-strain relationship can be written as

$$\dot{\sigma}_f = E_f^{ep} \dot{\varepsilon}_N \tag{3.32}$$

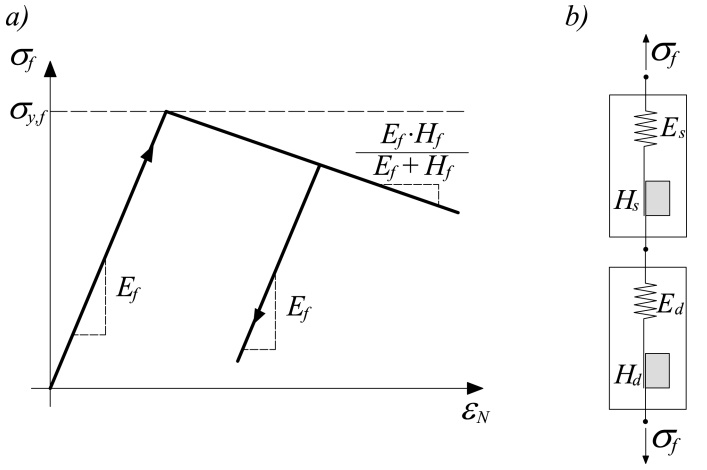

Figure 3.10: (a) Uniaxial model of fiber bond-slip and (b) serial model for the axial/debonding behavior.

where the elasto-plastic tangent module E_f^{ep} takes the two distinct following values [Simo and Hughes, 1998]

$$\begin{cases} E_f^{ep} = E_f & \rightarrow \text{elastic/unloading response} \\ E_f^{ep} = \frac{E_f \cdot H_f}{E_f + H_f} & \rightarrow \text{elasto-plastic regime} \end{cases} . \tag{3.33}$$

Fiber strain ε_N can be simply decomposed into two parts, one due to the intrinsic uniaxial deformation $\varepsilon_{N,s}$ and the other associated to the interface debonding $\varepsilon_{N,d}$,

$$\varepsilon_N = \varepsilon_{N,s} + \varepsilon_{N,d}. \tag{3.34}$$

Assuming a serial system with two 1D elastoplastic components, corresponding to the fiber axial behavior and the fiber-matrix debonding (see Fig. 3.10b), the resulting total elastic flexibility $1/E_f$ is given as

$$\frac{1}{E_f} = \frac{1}{E_s} + \frac{1}{E_d} \tag{3.35}$$

where E_s and E_d are the steel fiber elastic modulus and the equivalent elastic one of matrix-fiber debonding, respectively. Two limiting situations can be recognized:

- $E_d \rightarrow 0$: the serial structure response and, consequently, the uniaxial fiber strength vanish.
- $E_d \rightarrow \infty$: perfect bonding case between fiber and matrix.

The bond-slip axial constitutive model can be completed by defining the following material parameters

$$\sigma_{y,f} = min[\sigma_{y,s}, \sigma_{y,d}] \tag{3.36}$$

$$H_f = \begin{cases} H_s & \text{if } \sigma_{y,s} < \sigma_{y,d} \\ H_d & \text{otherwise} \end{cases} \tag{3.37}$$

whereby $\sigma_{y,s}$ and $\sigma_{y,d}$ are the yield stress and the equivalent interface elastic limit, respectively.

The parameters E_d, $\sigma_{y,d}$ and H_d required for the bond-slip model characterization, can be calibrated by analyzing a simple pull-out scheme as proposed in the following subsections and derived in detail in Chapter 4.

3.4.1 Closed-form pull-out analysis of a single fiber

Fig. 3.11 shows an isolated fiber loaded by a pulling force, P_i. The fiber is embedded in a cementitious matrix for a l_{emb} length measure. The equilibrium scheme given in the figure is used to simulate the complete slipping behavior.

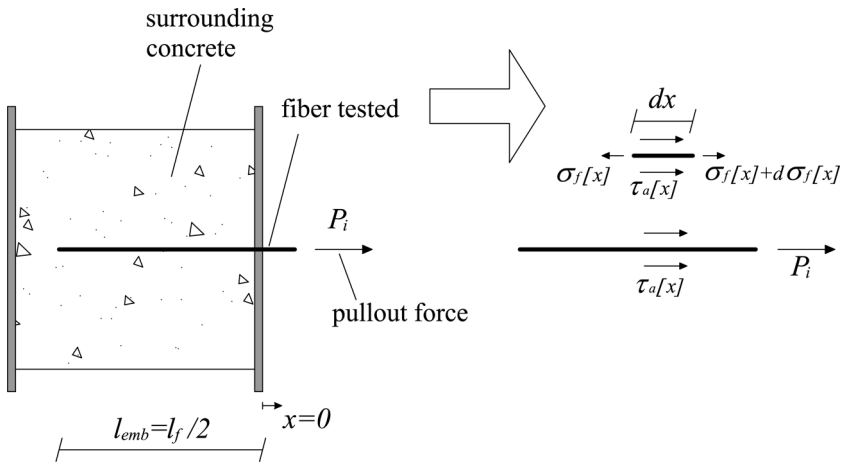

Figure 3.11: Pull-out of a single fiber reinforcement

The following basic equations were used for analyzing the fiber-to-concrete debonding process:

- *Equilibrium*: $\frac{d\sigma_f[x]}{dx} = -\frac{4\tau_a[x]}{d_f}$, being σ_f the axial stress of the fiber, τ_a the shear bond stress and d_f the diameter of the fiber.

- *Fiber constitutive law in axial direction*: $\sigma_f[x] = E_s \frac{ds[x]}{dx}$, with E_s the elastic steel modulus and $s[x]$ the slip between fiber and surrounding concrete mortar based on the assumption of Fig. 3.11.

- *Bond constitutive law*: $\tau_a[x] = \begin{cases} -k_E s[x] & s[x] \le s_e \\ -\tau_{y,a} + k_S (s[x] - s_e) & s_e < s[x] \le s_u \\ 0 & s[x] > s_u \end{cases}$,

  where, assuming a bilinear $\tau_a - s$ law, k_E and $-k_S$ represents the slope of the elastic and softening branches of the bond-slip relationship, respectively, $\tau_{y,a}$ whereas is the maximum shear stress. Thus, $s_e = \frac{\tau_{y,a}}{k_E}$ and s_u represent the elastic and the ultimate slips, respectively.

As schematically reported in Table 3.2 and based on the approaches proposed for studying FRP laminates under pull-out by Yuan et al. [2004] for long anchorages and Caggiano et al. [2012c] for general anchoring lengths, different states of the bond response can be defined. The fiber-to-concrete interface is in elastic bond state (E) if $s[x] \le s_e$, in softening state (S) when $s_e < s[x] \le s_u$, or the bond is crushed if $s[x] > s_u$. A combination of these three stress states can occur throughout the bonding length during the pull-out process of the single fiber (see Table 3.2).

Fully elastic behavior of fibers was assumed. This is strictly true in the case of synthetic fibers, while can be accepted for steel ones when the length l_{emb} results in the condition of $P_{i,max} \le \sigma_{y,s} A_f$, where $\sigma_{y,s}$ is the fiber yielding stress and A_f the area of transverse section.

Table 3.2: Bond response of the fiber-concrete joint depending on the slip $s[x]$ developed throughout the embedment length

Slips	**Type of joint adherence**
$s[x] \le s_e \forall x \in [-l_{emb}, 0]$	Elastic Response (E)
$s[x] \le s_e \forall x \in [-l_{emb}, -l_e]$ $s_e < s[x] \le s_u \forall x \in [-l_e, 0]$	Elastic – Softening Response (ES)
$s_e < s[x] \le s_u \forall x \in [-l_{emb}, 0]$	Softening Response (S)
$s[x] \le s_e \forall x \in [-l_{emb}, -l_e]$ $s_e < s[x] \le s_u \forall x \in [-l_e, -l_u]$ $s[x] > s_u \forall x \in [-l_u, 0]$	Elastic – Softening – Debonding (ESD)
$s_e < s[x] \le s_u \forall x \in [-l_{emb}, -l_u]$ $s[x] > s_u \forall x \in [-l_u, 0]$	Softening – Debonding Response (SD)
$s[x] > s_u \forall x \in [-l_{emb}, 0]$	Debonding Failure (D)

being $-l_e\,(0 \le l_e \le l_{emb})$ and $-l_u\,(0 \le l_u \le l_{emb})$ the abscissas of the points in which the local slip $s[x]$ is equal to the elastic limit (s_e) and the ultimate value (s_u), respectively.

For the sake of simplicity, the description of the complete analytical pull-out model is given in Chapter 4 completely dedicated to the pull-out modeling of fiber-to-concrete joints.

3.4.2 Verification of the pull-out model

Some numerical examples are reported in this section to show the main features of the proposed bond-slip analytical model. The verification examples include pull-out tests of both straight and hooked-end steel fibers. Test data by Lim et al. [1987] regarding pull-out probes were considered which relevant properties of fibers are listed as follows:

- *Straight fibers*: $d_f = 0.565\,mm$ (diameter), $\sigma_{y,s} = 345\,N/mm^2$ (strength), $E_s = 210\,GPa$ (elastic modulus).
- *Hooked fibers*: $d_f = 0.500\,mm$ (diameter), $\sigma_{y,s} = 1130\,N/mm^2$ (strength), $E_s = 200\,GPa$ (elastic modulus).

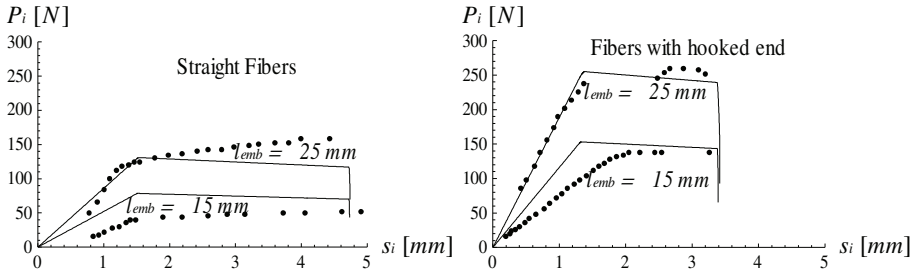

Figure 3.12: Pull-out tests (discontinuous lines) by Lim et al. [1987] on straight and hooked-end steel fibers vs. numerical results (continuous lines)

Table 3.3: Model parameters for the pull-out tests by Lim et al. [1987]

	MaterialParameters			
	$\tau_{y,a}[MPa]$	$k_E[MPa/mm]$	$k_S[MPa/mm]$	$s_u[mm]$
StraightFibers	3.0	2.0	0.1	4.725
HookedFibers	6.0	5.0	0.2	3.380

Figure 3.12 shows the $P_i - s_i$ curves (pull-out action vs. applied slip) for straight and hooked-end steel fibers with different embedment lengths based on the model parameters defined in Table 3.3.

The proposed model leads to good predictions of the behavior of both fiber types, capturing the increment of strength as the embedment measure increases. It is worth

nothing that the presence of hooked-ends in fibers determines an increase in shear strength, $\tau_{y,a}$, compared to straight fibers and a decrement of the ductility of the contact. As a matter of fact, the elastic and softening slopes (k_E and k_S, respectively) increase considering hooked-end fibers, while a decrease in the ultimate slip, s_u, passing from straight to hooked fibers can be observed.

3.5 Dowel effect of steel fibers crossing cracks in cementitious matrix

A 1D elastoplastic model was considered to take into account the dowel effect of fibers crossing one single crack. This model describes the evolution law of the shear fiber strains $\dot{\gamma}_T$ and the dowel stress $\dot{\tau}_f$ (needed relationship in the composite model outlined in Eq. 3.2) representing the interaction between fiber and matrix as follows

$$\dot{\gamma}_T = \dot{\gamma}_T^{el} + \dot{\gamma}_T^{pl} \tag{3.38}$$

$$\dot{\tau}_f = G_f\left(\dot{\gamma}_T - \dot{\gamma}_T^{pl}\right) \tag{3.39}$$

being $\dot{\gamma}_T^{el}$ and $\dot{\gamma}_T^{pl}$ the elastic and plastic shear strain components, respectively, and G_f the equivalent shear modulus.

Within the framework of the flow plasticity theory, the complete model is described by means of the following set of equations:

- *Yield function*: $g_f = |\tau_f| - (\tau_{y,f} + Q_{dow}) \leq 0$, when τ_f is the dowel shear stress, $\tau_{y,f}$ the dowel strength and Q_{dow} the stress-like internal parameter.
- *Softening law*: $\dot{Q}_{dow} = \dot{\lambda}_f H_{dow}$, where $\dot{\lambda}_f$ and H_{dow} are the plastic multiplier and the hardening/softening modulus, respectively.
- *Flow rule*: $\dot{\gamma}_T^{pl} = \dot{\lambda}_f \partial g_f / \partial \tau_f = \dot{\lambda}_f sign[\tau_f]$, where $\dot{\gamma}_T^{pl}$ is the rate of the plastic dowel strain.

The Kuhn-Tucker loading/unloading conditions (with the consistency relation) complete the formulation of the model. The constitutive law between the dowel shear stress, τ_f, and the corresponding equivalent shear strain, γ_T, can be written in incremental form as follows

$$\dot{\tau}_f = G_f^{ep}\dot{\gamma}_T \tag{3.40}$$

being G_f^{ep} the tangent modulus expressed in terms of the initial dowel stiffness G_f and

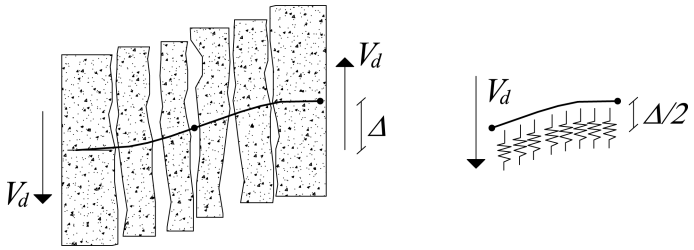

Figure 3.13: Dowel effect based on the well-known Winkler beam theory.

the hardening/softening modulus H_{dow}, depending on to consider the cases of loading or unloading/elastic

$$\begin{cases} G_f^{ep} = G_f & \rightarrow \text{unloading/elastic} \\ G_f^{ep} = \frac{G_f \cdot H_{dow}}{G_f + H_{dow}} & \rightarrow \text{loading} \end{cases} \tag{3.41}$$

in which usually $H_{dow} = 0$.

3.5.1 Dowel stiffness

The analytical model, used to predict the dowel behavior of fibers embedded in concrete composites, was based on the analysis of a beam on elastic foundation (BEF), see Fig. 3.13. The following differential equation for the deflection equilibrium of a BEF can written

$$\frac{d^4\Delta(x)}{x^4} + 4\lambda^4\Delta(x) = 0 \qquad \text{with} \qquad \lambda^4 = \frac{k_c}{4E_sJ_s} \tag{3.42}$$

being $\Delta(x)$ the deflection of the beam, k_c the elastic stiffness of the spring foundation modelling the surrounding cementitious matrix, E_s and J_s are the elastic modulus of the steel and the inertia of the fiber, respectively, and finally λ represents a characteristic length of the Winkler beam.

The quantity λ has the dimension of $1/length$. Then a fundamental parameter can be introduced that is widely used in the related literature: $l_{fun} = 2\pi/\lambda$, representing the characteristic length of BEF. It is largely accepted that when the length dimension of a BEF exceeds $l_{fun}/2$ the same beam can be treated as semi-infinite BEF. In case of SFRC, the fibers are characterized by small diameters d_f, then, this hypothesis is still valid.

Based on this, the fiber can be analyzed as a “semi-infinite” BEF, then the following equations govern the problem

$$\begin{aligned} \Delta(x) &= A_1 e^{-\lambda x}\cos(\lambda x) + A_2 e^{-\lambda x}\sin(\lambda x) \\ M_d(x) &= 2E_sJ_s\lambda^2 e^{-\lambda x}[A_2\cos(\lambda x) - A_1\sin(\lambda x)] \\ V_d(x) &= -2E_sJ_s\lambda^3 e^{-\lambda x}[(A_2 - A_1)\sin(\lambda x) + (A_1 + A_2)\cos(\lambda x)] \end{aligned} \tag{3.43}$$

being M_d and V_d the bending moment and the dowel action at $l_f/2$ of the steel fiber, while A_1 and A_2 are constants deriving by the boundary conditions.

The analytical solution of the semi-infinite BEF problem is based on the assumption that the crack width is considered null and supposing that in $x = 0$ the moment is null (inflection point). Then, considering an applied dowel force, V_d, at the loaded end ($x = 0$), the following analytical deflection is obtained

$$\Delta(x) = -\frac{e^{-\lambda x}\cos(\lambda x)}{2\lambda^3 E_s J_s} V_d. \tag{3.44}$$

Finally, the $V_d - \Delta$ law in correspondence of the considered crack ($x = 0$) takes the following expression

$$\begin{aligned} V_d = \lambda^3 E_s J_s \Delta \rightarrow \frac{V_d}{A_f} = \frac{l_f}{A_f}\lambda^3 E_s J_s \frac{\Delta}{l_f} \\ \Rightarrow G_f = \frac{l_f}{A_f}\lambda^3 E_s J_s \end{aligned} \tag{3.45}$$

also expressed in terms of $\tau_f - \gamma_T \left(\frac{V_d}{A_f} - \frac{\Delta}{l_f}\right)$ law, from which the dowel stiffness, G_f, can be derived. In Equation [3.45] $A_f = \pi \frac{d_f^2}{4}$ is the cross sectional area of a single fiber.

The elastic stiffness of the spring foundation, k_c, represents the foundation stiffness that in the present case is defined by the stiffness of the surrounding mortar. Experimental tests performed on RC-members [Dei Poli et al., 1992] show that typical values of k_c vary from 75 to 450 N/mm^3. In other tests [Soroushian et al., 1987] can be observed that the coefficient k_c increases with the strength of the surrounding mortar matrix as well as with the volume fraction of the reinforcement. Furthermore, the dowel stiffness is somehow inversely proportional to the fiber diameter.

The elastic foundation stiffness of the surrounding concrete, k_c, assumes the following empirical expression [Soroushian et al., 1987]

$$k_c = \kappa_1 \frac{\sqrt{f_c}}{{d_f}^{2/3}} \tag{3.46}$$

being f_c the compression strength of the surrounding cementitious matrix and κ_1 a coefficient to be calibrated.

3.5.2 Dowel strength

Typical failures in the fiber dowel are characterised by local crushing of the surrounding matrix and/or yielding of the steel fiber. For these reasons, the following empirical

expression [Dulacska, 1972], considering both failure modes, is employed

$$V_{d,u} = k_{dow} d_f^2 \sqrt{|f_c||\sigma_{y,s}|} \tag{3.47}$$

being k_{dow} a non-dimensional coefficient which typical value $k_{dow} = 1.27$ could be assumed as a reference for RC-structures [Dulacska, 1972].

Finally, the equivalent dowel strength $\tau_{y,f}$ can be defined for the dowel action (and employed for the yielding criterion above mentioned)

$$\tau_{y,f} = \frac{V_{d,u}}{A_f}. \tag{3.48}$$

3.6 Closure chapter and conclusions

In this section, a new constitutive theory for failure analysis of Fiber-Reinforced Cementitious Composites (FRCCs) was proposed. An innovative approach for reproducing the fiber effects on the cracking phenomena of the concrete/mortar matrix was considered. The well-known discrete crack approach based on zero-thickness interface elements was taken as reference framework. The matrix degradation under mode I and II failure modes was modeled by means of a fracture energy-based softening law formulated in the framework of the flow theory of plasticity. Two fundamental aspects of the fiber-mortar interaction were considered in the model, i.e. the bond behavior of fibers bridging the crack opening and the dowel effect derived by possible relative transverse displacements of the two faces of the crack. The inclusion of fibers and the above two effects were taken into account by means of the well-known Mixture Theory.

The meso-mechanical approach (and the consequent possibility of modeling the behavior of FRCC starting from both their components and the interactions among them) was the key novelty of the proposed model. As a matter of principle, the huge aleatoric nature of FRCC (mainly deriving by the randomness in fiber orientation and distribution, aggregate size and collocation, mixing and casting procedures and so on, so forth) was the key reason why simulating the global behavior of FRCCs starting from their constituents can lead to unreliable predictions of the global response of the composite material as a whole. Nevertheless, the basic interactions among the various components which actually affect the global response of FRCC can be modeled mechanically as proposed in the present work and the natural randomness of the component properties and distribution can be handled within the framework of well established statistical procedures whose application was beyond the scopes of the present formulation. The soundness and capabilities of the proposed formulation will be given in the following dedicated chapter of this thesis.

The interface model proposed in this work can be employed in mesoscopic analyses

aimed at simulating failure processes possibly developing at the mortar-mortar and mortar-aggregate interfaces see a.o. Lopez [1999] and Idiart [2009]. The strategy proposed in this section for modeling failure behavior of FRCCs based on the discrete crack approach and on interface elements can straightforwardly be extended to other well-known numerical techniques. In this regards, finite elements with additional degrees of freedom by Oliver et al. [2002, 2006] (with Embedded discontinuities known as E-FEM), or with additional nodal degrees of freedom [Moes and Belytschko, 1999, Hettich et al., 2008] (eXtended-FEM) could be considered as alternative numerical frameworks for FRCCs modeling. Other interesting procedures that could be also mentioned with the strategy here proposed for FRCCs are the so-called lattice models [van Mier et al., 2002, Lilliu and van Mier, 2003], the particle-based formulations [Bazant et al., 1990, Rabczuk and Belytschko, 2006], the Element-free Galerkin [Belytschko et al., 1995, Zhang et al., 2008] and the hybrid-Trefftz stress-based formulation in Kaczmarczyk and Pearce [2009].

4 A unified formulation for simulating the bond behavior of fibers in cementitious materials

This chapter presents a unified formulation for simulating the overall bond behavior of fibers embedded in cementitious matrices. In principle, such a formulation is based on assuming a model between interface bond stresses and the corresponding relative displacements. Two alternative models are actually considered. The first one is based on a simplified bilinear relationship and can be handled analytically; the second one assumes a refined fracture-based plasticity model which requires for its integration a numerical solution approach. Both models, considered in the present formulation, address the behavior of fibers under tensile axial stresses which result in a "mode II" debonding phenomenon. Finally, numerical results are reported for both validating the proposed models against relevant experimental results and pointing out the differences possibly arising by adopting the two alternative models considered.

4.1 Importance of the bond-slip modeling

A sound knowledge of fiber-matrix interaction is of key importance for simulating the response of structural members made out of Fiber-Reinforced Cementitious Composites (FRCCs). As a matter of principle, the effectiveness of fibers, embedded in cement-based matrices, mainly depends on several factors such as fiber length, diameter, fiber type (e.g., smooth, hooked-end, flattened, twisted, etc.) and materials of both reinforcement and surrounding matrix. Moreover, the bond behavior is a complex phenomenon actually controlled by physical and chemical interactions between fiber and matrix.

In the last decades, several innovative researches were carried out to manipulate the interface-structure at both physical and chemical levels. The superior performance of hooked-ended and "non-smooth" fibers is clearly pointed out in experimental studies by Naaman and Najm [1991], Laranjeira et al. [2010]. Further experimental evidence about such a role is available in Cunha et al. [2010], whereas the effect of fiber length on the pull-out mechanism of polypropylene fibers is outlined in Singh et al. [2004].

However, the bond behavior of fibers embedded in cementitious matrix is not only affected by the above mentioned fiber properties, but it is even deeply influenced by the matrix quality. For instance, experimental researches on smooth fibers embedded in concrete of Normal (N-) and High Strength Concretes (HSCs) given in Shannag et al. [1997] point out the fact that bond behavior can be enhanced as the matrix strength increases. Moreover, the inclusion of nano-particles in cement matrices is one of the most recent solutions, with the twofold objective of enhancing the durability of the fiber-to-matrix interface [Butler et al., 2009] and improving the adhesion properties between fibers and matrix [Wang et al., 2009].

Thus, since several parameters play a significant role in affecting the fiber-matrix interaction in FRCC, the formulation of sound mechanical models for simulating the bond behavior of fibers is a fairly challenging issue. As a matter of principle, two main families of such models can be recognized in the scientific literature[Stang et al., 1990, Li and Chan, 1994]: the first one can be defined as *stress-based approaches* [Katz and Li, 1995, Ghavami et al., 2010], while the second one is represented by the so-called *energy-based bond-slip models* [Shah and Ouyang, 1991, Fantilli and Vallini, 2007].

Besides the particular interest in simulating the mechanical response of single fibers, the above mentioned models should be intended as a key contribution towards the possible modeling of the structural behavior of FRCC members based on the explicit simulation of the fiber influence on cracking processes. As a matter of fact, the most common mechanical models currently employed for simulating the behavior of FRCC are based on continuous smeared-crack approaches [Seow and Swaddiwudhipong, 2005] and generally deriving by previous proposals originally formulated for plain concrete [Folino et al., 2009, Folino and Etse, 2012]. Although such models are generally accepted in simulating the cracking behaviors of FRCC, it should be noted that their calibration is necessarily based on experimental results directly obtained on the FRCC material under consideration, as the fiber-matrix bond interaction deeply affects the post-cracking regime and the corresponding material parameters (mainly related with the fracture energy to be considered in smeared-crack approaches).

To overcome this drawback, alternative models aimed at explicitly simulating the actual discrete nature of FRCC are recently formulated within the framework of the so-called discontinuous-based approaches [Oliver et al., 2008, Caggiano et al., 2012b]. The discrete-crack approach and the consequent possibility of modeling the behavior of FRCC starting from both their components (i.e., the bond-slip mechanisms) and the interactions among them is the main issue of the proposal reported in Chapter 3. Although such model is more computationally demanding, they can, in principle, be identified through accurate models and parameters which are directly and explicitly related to the key material components. Thus, the accurate description of the fiber-matrix bond behavior is a key element to formulate and identify such meso-mechanical models.

In this framework, the present chapter proposes a unified formulation for simulating such a bond behavior based on the fundamental assumptions reported in Section 4.2. Two alternative models are actually considered. The first one is based on the simpler elasto-plastic behavior with isotropic linear softening as outlined in Section 4.3. Conversely, the second one is founded on the fracture energy-based contact model outlined in Section 4.4 and will be employed in a numerical solution of the fiber-matrix interaction problem. Finally, Section 4.5 presents the results of simulations obtained through the two models considered in the presented unified formulation of the tensile response of fibers embedded in concrete matrices. Moreover, the theoretical prediction of the influence of relevant parameters (such as fiber anchorage length and diameter) is also outlined in the same section.

4.2 Bond behavior of fibers in concrete matrix: basic assumptions

The basic assumptions for Finite Element (FE) simulation of bond behavior of fiber embedded in cementitious materials are presented in this section. Fiber reinforcement is modeled through the use of one-dimensional two-nodes iso-parametric truss element. The interface slip between reinforcing steel and surrounding concrete is addressed by means of interface elements as schematically shown in Fig. 4.1.

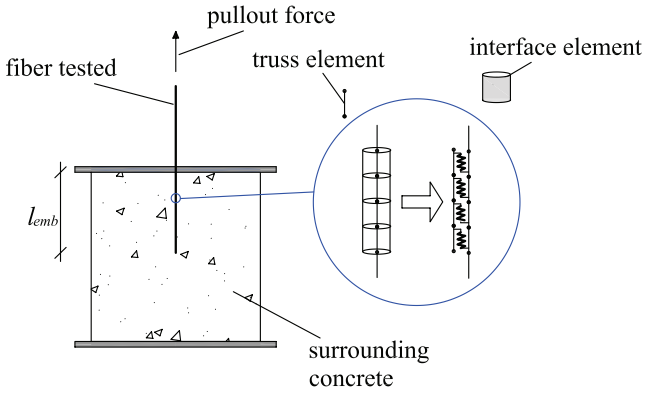

Figure 4.1: Considered scheme of fiber under pull-out loading.

4.2.1 Behavior of steel fibers

The mechanical behavior of steel in fibers is modeled as a 1-D elastic-perfectly plastic material. The incremental stress-strain law can be written as

$$\dot{\sigma}_f = E_f^{ep} \dot{\varepsilon}_f \tag{4.1}$$

being $\dot{\sigma}_f$ the axial stress rate of the fiber, $\dot{\varepsilon}_f$ the incremental axial strain and the tangent elasto-plastic modulus E_f^{ep} takes the following two distinct values

$$\begin{cases} E_f^{ep} = Ef \quad elastic/unloading \\ E_f^{ep} = 0 \quad loading\, with\, \dot{\lambda_f} > 0 \end{cases} \tag{4.2}$$

where $\dot{\lambda}_f$ is the non-negative plastic multiplier captured by means of the Kuhn-Tucker and consistency conditions and E_f represents the uniaxial elastic module of the fiber.

Finally, the yielding criterion takes the following expression

$$f_f = |\sigma_f| - \sigma_{y,f} \leq 0 \tag{4.3}$$

in which $\sigma_{y,f} \geq 0$ is the yield limit of the steel.

4.2.2 Interface bond-slip models

Two rate-independent contact laws are proposed in this work with the aim to study the fiber-to-concrete debonding:

- Elasto-plastic model with linear strain-softening: the same one adopted in the composite model outlined in Chapter 3.
- Fracture-based debonding model: a richer proposal based on fracture-based concepts and conceived within a work-softening plasticity formulation;

Table 4.1 describes the key aspects of both models. In particular, $f(\tau,\kappa)$ and $g(\tau,\kappa)$ represent the two yielding criteria based on the interface shear stress τ and the internal (strain-like) variable κ of each considered model; τ_y represents the failure shear strength.

Both bond-slip models can be directly implemented as plasticity-type constitutive laws for interface elements. The rate of elastic relative slip, $\dot{s}^e$, is introduced and related to the shear stress through the elastic stiffness, k_E. In the framework of the incremental plasticity theory, the following basic equation can be used

$$\dot{s} = \dot{s}^e + \dot{s}^p \qquad \dot{s}^e = \frac{\dot{\tau}}{k_E} \tag{4.4}$$

where inelastic, $\dot{s}^p$, and total interface slip $\dot{s}$ are introduced in incremental form.

Integrating each constitutive model, the constitutive laws can be defined in terms of the tangent elasto-plastic constitutive operator, k_{tan}^{ep}, which is specified for loading or unloading/elastic processes in Table 4.1.

Table 4.1: Interface bond-slip models.

	Fracture-based interface model	Elasto-plasticity with strain-softening
Loading criterion	$f(\tau,\kappa)=\tau^2-\tau_y^2\le 0$	$g(\tau,\kappa)=\lvert\tau\rvert-(\tau_{y,0}+Q)\le 0$
Stress-like internal variables	$\tau_y=\tau_{y,0}\left(1-\frac{w_{sl}}{G_f}\right)$ $\quad \dot{\kappa}=\dot{w}_{sl}=\tau\cdot\dot{s}^p$	$\dot{\kappa}=\dot{Q}=\dot{\lambda}\cdot k_H$
Plastic flow	$\dot{s}^p=\dot{\lambda}\frac{\partial f}{\partial\tau}=2\cdot\dot{\lambda}\cdot\tau$	$\dot{s}^p=\dot{\lambda}\frac{\partial g}{\partial\tau}=\dot{\lambda}\cdot sign[\tau]$
Constitutive equation	$\dot{\tau}=k_E(\dot{s}-\dot{s}^p)$	
Loading-unloading condition	$\dot{\lambda}\ge 0,\ f\le 0,\ \dot{\lambda}\cdot f=0$	$\dot{\lambda}\ge 0,\ g\le 0,\ \dot{\lambda}\cdot g=0$
Constitutive tangent operator	$\dot{\tau}=k_{tan}^{ep}\cdot\dot{s}$ $\quad k_{tan}^{ep}=k_{E,2}\cdot\left(1-\frac{\left(\frac{\partial f}{\partial\tau}\right)^2+\Delta\lambda\frac{\partial f}{\partial\tau}\left(\frac{\partial f}{\partial\kappa}\frac{\partial\kappa}{\partial s^p}\right)\cdot\frac{\partial^2 f}{\partial\tau^2}}{\left(\frac{\partial f}{\partial\tau}\right)^2+H/k_{E,2}}\right)$ $\quad k_{tan}^{ep}=k_E$ $\ elastic/unloading$	$k_{tan}^{ep}=k_E\left(1-\frac{k_E}{k_E+k_H}\right)$

4.3 Elasto-plastic joint model with isotropic linear softening

This section presents a classical one-dimensional plasticity model aimed at simulating the bond-slip behavior of fiber-to-concrete interface.

Based on the additive split of the relative interface displacements and the incremental elastic law given in Eq. (4.4), the model is formulated by means of the following yield criterion

$$g(\tau,\kappa)=|\tau|-(\tau_y+Q)\le 0 \tag{4.5}$$

in which the stress-like evolution, in post-elastic regime, is driven by the internal hardening variable Q, which variation depends on the hardening/softening parameter k_H (to see Table 4.1), obtaining a strain-softening contact law for $k_H<0$ in post-elastic response (Fig. 4.2).

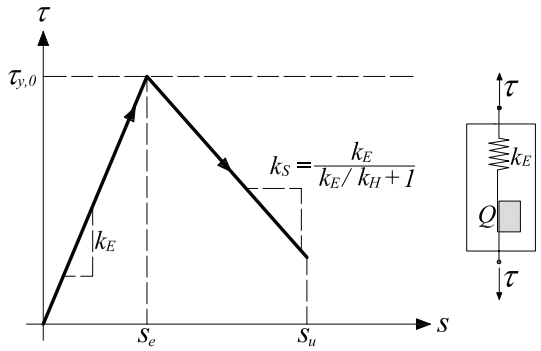

Figure 4.2: Bond-slip plasticity model with linear softening.

The plastic flow is again captured by means of the Kuhn-Tucker loading/unloading and consistency conditions. The incremental bond-slip law, can be written as

$$\dot{\tau} = k_{tan}^{ep} \dot{s} \tag{4.6}$$

where the tangent elasto-plastic module k_{tan}^{ep}, derived as widely reported in literature [Simo and Hughes, 1998], is reported in Table 4.1.

4.3.1 Basic assumptions and closed-form solution

The complete closed-form analytical solution, in case of bilinear $\tau - s$ relationship as in Fig. 4.2, of the pull-out behavior of fiber-to-cementitious matrix is also presented.

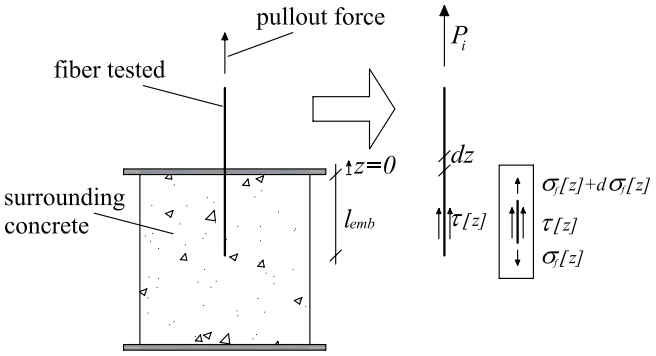

Figure 4.3: Schematic components of pull-out analysis for the analytical solution.

The model, based on small displacement theory, assumes that strains of the matrix support, surrounding the fiber, can be considered negligible during the debonding process. According to the previous plasticity model, the contact law ($\tau - s$) presents a bilinear form, featuring an initial linear ascending branch, with the k_E initial slope, followed, when the elastic limit $\tau_{y,0}$ is reached, by a linear softening branch which slope is now defined as $k_S = k_E \left(1 - \frac{k_E}{k_E + k_H}\right)$. The model is completed considering an ultimate slip, s_u, at which the bond transferred stress is considered null. The full analytical solution is applied to a single fiber, as schematized in Fig. 4.3.

Based on the assumption that the fiber diameter d_f and the local bond-slip relationship keep unchanged throughout the fiber bond length, l_{emb}, the following infinitesimal equilibrium condition can be formulated

$$\frac{d\sigma_f[z]}{dz} = -\frac{4\tau[z]}{d_f} \tag{4.7}$$

where $\tau[z]$ is the shear stress transferred at the interface and $\sigma_f[z]$ the axial steel stress.

Assuming that bond failure occurs for maximum fiber stresses lower than the yield limit of fiber steel (as generally observed in experimental investigations), the following constitutive laws, modeling both the mechanical response of fiber and the interface adherences, respectively, can be expressed

$$\sigma_f[z] = E_f \frac{ds[z]}{dz} \tag{4.8}$$

and

$$\begin{cases} \tau[z] = -k_E s[z] & \rightarrow \text{if } s[z] \leq s_e \\ \tau[z] = -\tau_{y,0} + k_S[s[z] - s_e] & \rightarrow \text{if } s_e < s[z] \leq s_u \\ \tau[z] = 0 & \rightarrow \text{if } s[z] > s_u \end{cases} \tag{4.9}$$

being $s[z]$ the slip measured at generic z coordinate while $s_e = \tau_{y,0}/k_E$ is the elastic slip value.

After substituting the Eq. (4.8) into Eq. (4.7), the following differential equation, in terms of $s[z]$, can be obtained

$$\frac{d^2 s[z]}{dz^2} + \frac{4\tau[z]}{d_f E_f} = 0 \tag{4.10}$$

representing the general governing differential equation of the bonded joint between fiber and concrete which can be integrated assigning the local shear stress-slip laws defined in Eq. (4.9).

Eq. (4.10) can be solved, under appropriate boundary conditions, in order to obtain the complete problem in closed form: i.e., in terms of slips $s[z]$, shear stress distribution $\tau[z]$, axial fiber stress $\sigma_f[z]$ and, finally, the global pull-out response $P_i - s_i$ at the loaded-end.

In particular, three main differential equations must be integrated:

- *Elastic $\tau - s$ case*: $s[z] \leq s_e$, the adherence law is represented by recoverable shear stresses dealing with the following differential equation

  $$\frac{d^2 s[z]}{dz^2} - \alpha_1^2 s[z] = 0 \tag{4.11}$$

  at which corresponds the following general integral

  $$s[z] = A_1 \sinh[\alpha_1 z] + A_2 \cosh[\alpha_1 z] \tag{4.12}$$

  where A_1 and A_2 are two unknown constants to determine with appropriate boundary conditions while $\alpha_1 = 2\left(\frac{k_E}{d_f E_f}\right)^{1/2}$.

- *Softening $\tau - s$ case*: $s_e < s[z] \leq s_u$, the interface law is represented by stress in post-elastic response of the domain, dealing with the following differential relation

$$\frac{d^2 s[z]}{dz^2} + \alpha_2^2 s[z] - 4\frac{k_E + k_S}{E_f} s_e = 0 \tag{4.13}$$

which general integral is

$$s[z] = A_3 \cos[\alpha_2 z] + A_4 \sin[\alpha_2 z] + \frac{k_E + k_S}{k_S} s_e \tag{4.14}$$

with $\alpha_2 = 2\left(\frac{k_S}{d_f E_f}\right)^{1/2}$, A_3 and A_4 are integration constants.

- *Debonded $\tau - s$ case*: $(s[z] > s_u)$, the shear stress locally transferred between concrete and fiber is null, it follows that

$$\frac{d^2 s[z]}{dz^2} = 0 \tag{4.15}$$

which general integral is

$$s_3[z] = A_5 z + A_6 \tag{4.16}$$

being A_5 and A_6 constants of integration.

4.3.2 Full-range bond-slip behavior

This section presents the analytical description of the complete debonding process, by means of a stage-by-stage integration of the relevant equations, whose form depends of the actual state of the interface.

Both interface-slip distribution $s[z]$ and the global force-displacement pull-out response $P_i - s_i$ are investigated. For the sake of brevity, many details of the analytical integration are not provided but can be easily derived in a similar mode as detailed in Caggiano et al. [2012c] in a similar study dedicated to FRP-to-concrete under pull-out loading.

When the bond-slip process starts with a low pull-out action, the transferred shear stresses, along the fiber-to-concrete interface, are in elastic state. This stage is defined as **elastic stage (E)** whose solutions in terms of $P_i - s_i$ curve and slips $s[z]$ are given in Table 4.2.

Once the applied slip at the loaded extreme becomes greater than the elastic limit $s_i > s_e$, a new stage takes place called **softening-elastic (SE)**. In this instance the fiber anchoring interface can be subdivided into two parts: (i) part I closer to the loaded

Table 4.2: Analytical bond-slip model of the bilinear $\tau - s$ relationship.

Closed-form full range pull-out behavior

Elastic stage - E: $s_i \leq s_e$

$$P_i = \pi {\alpha_1}^{-1} \tanh(\alpha_1 l_{emb}) d_f k_E s_i$$

- Elastic solution $z \in [-l_{emb}, 0]$: $s[z] = \frac{\cosh[\alpha_1(lemb+z)]}{\cosh[\alpha_1 l_{emb}]} s_i$

Softening-Elastic stage - SE: $s_i > s_e$

$$s_i = \left(1 + \frac{k_E}{k_S}(1 - \cos[\alpha_2 l_e]) - \frac{\sqrt{k_E}}{\sqrt{k_S}} \sin[\alpha_2 l_e] \tanh[\alpha_1 (l_e - l_{emb})]\right) s_e$$

$$P_i = \frac{\pi}{2} {d_f}^{3/2} \left(k_E / \sqrt{k_S} \sin[\alpha_2 l_e] - \sqrt{k_E} \cos[\alpha_2 l_e] \tanh[\alpha_1 (l_e - lemb)]\right) \sqrt{E_f} s_e$$

- Softening solution $z \in [-l_e, 0]$: $s[z] = \left(1 + \frac{k_E}{k_S}(1 - \cos[\alpha_2 (l_e + z)]) - \frac{\sqrt{k_E}}{\sqrt{k_S}} \tanh[\alpha_1 (l_e - l_{emb})] \sin[\alpha_2 (l_e + z)]\right) s_e$

- Elastic solution $z \in [-l_{emb}, -l_e]$: $s[z] = \frac{\cosh[\alpha_1 (l_{emb}+z)]}{\cosh[\alpha_1 (l_e - l_{emb})]} s_e$

"Short fibers": $l_{emb} \leq l_{sl}$

Softening stage - S: $s_i > s'_B$

$$P_i = \pi d_f {\alpha_2}^{-1} \tan[\alpha_2 l_{emb}]([k_E + k_S] s_e - k_S s_i)$$

- Softening solution $z \in [-l_{emb}, 0]$:

$$s[z] = (s_i - [k_E / k_S + 1] s_e) \cos[\alpha_2 (l_{emb} + z)] \sec[\alpha_2 l_{emb}] + (k_E / k_S + 1) s_e$$

Debonding-Softening stage - DS: $\forall P_i \in [0, P'_C]$

$$s_i = s_u + P_i \left[\frac{\alpha_2}{\pi k_S} \tan^{-1}\left(\frac{k_E \alpha_2}{\pi d_f [k_E k_S s_u - \tau_{y,0}(k_E + k_S)]} P_i\right) + \frac{{\alpha_2}^2 l_{emb}}{\pi k_S}\right]$$

- Debonding solution $z \in [-l_u, 0]$: $s[z] = s_u - \left(s_u - \tau_{y,0} \frac{k_E + k_S}{k_E k_S}\right) \alpha_2 (l_u + z) \tan[\alpha_2 (l_{emb} - l_u)]$

- Softening solution $z \in [-l_{emb}, -l_u]$: already given in the SE-stage (it is now necessary to replace $l_{emb} \rightarrow l_e$).

"Long fibers": $l_{emb} > l_{sl}$

Debonding-Softening-Elastic stage - DSE: $s_i > s_u$

$$s_i = \left(1 + \frac{k_E}{k_S} + \frac{k_E}{k_S} l_u \alpha_2 \sin[\alpha_2 (l_e - l_u)] - \frac{k_E}{k_S} \cos[\alpha_2 (l_e - l_u)] - \frac{1}{2} \alpha_1 \tanh[\alpha_1 (l_e - l_{emb})] \left(\frac{d_f E_f}{2 k_S} \alpha_2 \sin[\alpha_2 (l_e - l_u)] + 2 l_u \cos[\alpha_2 (l_e - l_u)]\right)\right) s_e$$

$$P_i = \left(\frac{\sin[\alpha_2 (l_e - l_u)]}{\sqrt{k_S}} - \frac{\cos[\alpha_2 (l_e - l_u)] \tanh[\alpha_1 (l_e - l_{emb})]}{\sqrt{k_E}}\right) \cdot \frac{\pi}{2} d_f^{3/2} \sqrt{E_f \tau_{y,0}}$$

- Debonding solution $z \in [-l_u, 0]$:

$$s[z] = \left(1 + k_E / k_S - k_E / k_S \cos[\alpha_2 (l_e - l_u)] - \sqrt{k_E} / \sqrt{k_S} \tanh[\alpha_1 (l_e - l_{emb})] (\alpha_2 (l_u + z) \cos[\alpha_2 (l_e - l_u)] + \sin[\alpha_2 (l_e - l_u)]) + k_E / k_S \alpha_2 (l_u + z) \sin[\alpha_2 (l_e - l_u)]\right) s_e$$

- Softening solution $z \in [-l_e, -l_u]$: *already given in the SE-stage*

- Elastic solution $z \in [-l_{emb}, -l_e]$: *already given in the SE-stage*

Debonding-Softening stage - DS: $\forall P_i \in [0, P_C]$

end in which $s[z] > s_e$ and (ii) the remaining part in which $s[z] \leq s_e$. The expressions of the interface slips for the two parts of the bonded interface, $s[z]$, the pull-out force P_i and the slip s_i, reported in Table 4.2, depend on the value of the given parameter $l_e \in [0, l_{emb}]$ which determines the configuration of the bonded interface. It represents the abscissa of the point at which the local slip is equal to the elastic limit $s[-l_e] = s_e$.

The evolution of the fiber debonding process follows two possible alternatives that follows the SE-stage: (i) the applied slip s_i in $z = 0$ reaches the ultimate slip value s_u, while the minimum slip $s[-l_{emb}] < s_e$: this case represents the transition to the new **Debonding-Softening-Elastic (DSE)**-)stage; (ii) the slip at the free-end of the fiber, reaches the elastic limit, $s[-l_{emb}] = s_e$ while $s_i < s_u$: this instance follows to the new only **Softening (S)**stage. The anchoring length $l_{emb} = l_{sl}$ which verifies the two mentioned conditions represents a critical value dealing with the boundary between the short from long anchorages. This length can be now defined as follows

$$l_{sl} = {\alpha_2}^{-1} \sec^{-1}\left(\frac{\tau_0}{\tau_0\left(\frac{k_S}{k_E}+1\right) - k_S s_u}\right) \tag{4.17}$$

Fibers which anchorage $l_{emb} > l_{sl}$ is defined as "long fibers", on the contrary, when $l_{emb} \leq l_{sl}$ the debonding process follows the second of the two mentioned evolutions considering the case of "short fibers". Table 4.2 outlines the complete bond-slip process in case of both short and long steel fibers.

Short fibers

Based on the "stage-by-stage" procedural study, the complete bond-slip response for short anchoring fibers is studied with a only **Softening (S-)**stage that follows the previous SE-stage. All the bond interface is modeled by means of the softening branch of Fig. 4.2. A linear-type softening response is obtained by the global $P_i - s_i$ curve for the S-stage as plotted in Fig. 4.4 (trait $B' - C'$) which expression is given in Table 4.2.

The point B', in the global pull-out curve, posses the following coordinates

$$s'_B = \left(1 + \frac{k_E}{k_S}\left(1 - \cos[\alpha_2 l_{emb}]\right)\right) s_e \tag{4.18}$$

$$P'_B = \pi {\alpha_2}^{-1} d_f \tau_0 \sin[\alpha_2 Lc] \tag{4.19}$$

while the other extreme (C' of Fig. 4.4) is given by the following coordinates

$$s'_C = s_u \tag{4.20}$$

$$P'_C = \pi {\alpha_2}^{-1} d_f \tan[\alpha_2 l_e]([k_E + k_S] s_e - k_S s_u). \tag{4.21}$$

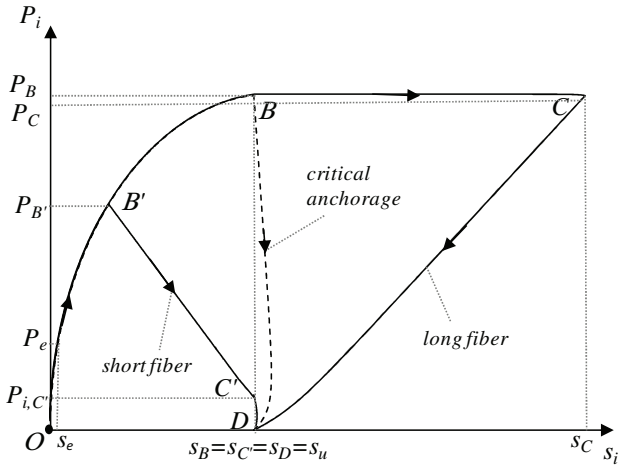

Figure 4.4: Typical analytical curves of the applied load P_i vs. debonding displacement s_i in case of short and long anchorage condition.

Long fibers

In case of "long fibers" ($l_{emb} > l_{sl}$), the bond-slip process develops, from the previous SE-stage, with a crushed zone in the neighbors of the loaded-end, whose length is identified by l_u. The analytical solution of this stage, namely **Debonding-Softening-Elastic (DSE)**, is given in Table 4.2 in terms of slips $s[z]$ and global pull-out curve $P_i - s_i$. The closed relations depend on the two parameters l_e and l_u which determine the configuration states of the fiber-to-concrete bond. The values of those two parameters are strictly connected by means of the following relationships

$$l_u = l_e - \alpha_2^{-1}\sec^{-1}\left(\frac{k_E + k_S d_f \tanh^2[\alpha_1(l_e - l_{emb})]}{k_E + k_S - \frac{k_S s_u}{s_e} + k_1}\right) \tag{4.22}$$

with $k_1 = \left[k_S{}^2\tau_0{}^2\tanh^2[\alpha_1(l_e - l_{emb})]\left((s_e - s_u)(k_E k_S s_u - \tau_0(2k_E + k_S)) + \tau_0{}^2\tanh^2[\alpha_1(l_e - l_{emb})]\right)\right]^{1/2}$.

The bond-slip process can be followed by assuming the value l_e and evaluating l_u. Once the elastic contact vanishes ($l_e = l_{emb}$), the DSE-stage terminates reaching its ultimate point C, which coordinates is analytically obtained as follows

$$s_C = \left(1 + \frac{k_E}{k_S}\left[1 + \alpha_2 l_u \sin[\alpha_2(l_{emb} - l_u)] - \cos[\alpha_2(l_{emb} - l_u)]\right]\right) s_e \tag{4.23}$$

$$P_C = \pi\alpha_2{}^{-1} d_f \sin[\alpha_2(l_{emb} - l_u)]\tau_0. \tag{4.24}$$

Debonding-Softening (DS) stage represents the ultimate scenario for both "short" and "long" fibers in which the equilibrium is governed by two types of bond behaviors: i.e.,

one in which the bond adherence ($s_e < s[z] \leq s_u$) is in softening range while in the remaining part the contact is crashed ($s[z] > s_u$).

Table 4.2 reports both the expressions of $P_i - s_i$ and interface slip distribution $s[z]$ for the DS stage. The obtained results show an unstable behavior characterized by a snap-back softening response ($C-D$ branch for "long fibers" and part $C'-D$ branch for "short fibers") as shown in Fig. 4.4.

4.4 Fracture-based interface model

The proposed model, described in Table 4.1, is based on the plastic yield condition, $f(\tau,\kappa) \leq 0$,

$$f(\tau,\kappa) = \tau^2 - \tau_y^2 \leq 0. \tag{4.25}$$

The evolution of the yielding surface during the debonding process is driven by means of the following scaling law

$$\tau_y = \tau_{y,0}\left(1 - \frac{w_{sl}}{G_f}\right) \tag{4.26}$$

measured by means of the internal variable κ, defined as the work spent (w_{sl}) during the debonding process ("mode II" of fracture) as follows

$$\dot{\kappa} = \dot{w}_{sl} = \tau \cdot \dot{s}^p. \tag{4.27}$$

The amount of plastic slip rate is governed by the plasticity flow rule $\dot{s}^p = \dot{\lambda}\frac{\partial f}{\partial \tau}$, where the plastic multiplier, $\dot{\lambda}$, can be determined in a finite load-step by using the plastic consistency condition, $f_{n+1}(\Delta\lambda) = 0$, satisfying the yield condition f at the $n+1$ load-step, under persistent plastic deformations during the load-interval from n to $n+1$.

4.4.1 Incremental plastic multiplier

In order to find the accurate value of the incremental inelastic multiplier, $\Delta\lambda$, in a finite load-step, the full consistency is imposed according to the following truncated Taylor series

$$\Delta\lambda_{n+1}^{k+1} = \Delta\lambda_{n+1}^{k} - \frac{f_{n+1}^{k}}{\left(\frac{\partial f}{\partial \Delta\lambda}\right)_{n+1}^{k}} \tag{4.28}$$

identifying with k the local iteration step of the Newton-Raphson method of Eq. (4.28). The quantity $\frac{\partial f}{\partial \Delta\lambda}$ can be developed as follows

$$\frac{\partial f}{\partial \Delta\lambda} = \frac{\partial f}{\partial \tau} \cdot \frac{\partial \tau}{\partial \Delta\lambda} + \left[\frac{\partial f}{\partial \tau_y} \frac{\partial \tau_y}{\partial \kappa} \frac{\partial \kappa}{\partial s^p} \right] \cdot \frac{\partial s^p}{\partial \Delta\lambda} \tag{4.29}$$

The first derivative of the shear stress τ with respect to $\Delta\lambda$ can be obtained as

$$\frac{\partial \tau}{\partial \Delta\lambda} = -k_E \cdot \left(\Delta\lambda \frac{\partial^2 f}{\partial \tau^2} \cdot \frac{\partial \tau}{\partial \Delta\lambda} + \frac{\partial f}{\partial \tau} \right) \tag{4.30}$$

then solving for $\frac{\partial \tau}{\partial \Delta\lambda}$

$$\frac{\partial \tau}{\partial \Delta\lambda} = -\left(\frac{k_E}{1 + \Delta\lambda k_E \cdot M} \right) \cdot \frac{\partial f}{\partial \tau} = -k_{E,2} \cdot \frac{\partial f}{\partial \tau} \tag{4.31}$$

where $k_{E,2} = \left[k_E^{-1} + \Delta\lambda M \right]^{-1}$ is the modified elastic stiffness and $M \left(= \frac{\partial^2 f}{\partial \tau^2} = 2 \right)$ represents the Hessian operator.

The derivative $\frac{\partial s^p}{\partial \Delta\lambda}$ can be evaluated as

$$\frac{\partial s^p}{\partial \Delta\lambda} = \left[\frac{\partial f}{\partial \tau} - \Delta\lambda M \cdot k_{E,2} \cdot \frac{\partial f}{\partial \tau} \right]. \tag{4.32}$$

The remaining terms to calcule of Eq. (4.29) are the follows

$$\frac{\partial f}{\partial \tau} = 2 \cdot \tau \tag{4.33}$$

$$\frac{\partial f}{\partial \tau_y} = -2 \cdot \tau_y \tag{4.34}$$

$$\frac{\partial \tau_y}{\partial \kappa} = -\frac{\tau_{y,0}}{G_f} \tag{4.35}$$

$$\frac{\partial \kappa}{\partial s^p} = \tau \tag{4.36}$$

being $\tau_{y,0}$ the shear strength while G_f the fracture energy under mode II of crack.

4.4.2 Algorithmic tangential operator

The non-linear behavior, within a finite increment step, is solved by adopting the classical Newton-Raphson solution to solve the non-linear FE equations. The model is formulated by means of the construction of the algorithmic tangent operator to ensure a higher convergence rate than the continuous consistent one [Kang and Willam, 1999].

Considering the differentiated form of the incremental shear-slip law, a linearized tangential format of Eq. (4.4) can be reached

$$\begin{aligned} \Delta\tau &= k_E \cdot \left(\Delta s - \Delta\lambda \frac{\partial f}{\partial \tau}\right) \Rightarrow \\ d\Delta\tau &= k_E \cdot \left(d\Delta s - d\Delta\lambda \frac{\partial f}{\partial \tau} - \Delta\lambda d\frac{\partial f}{\partial \tau}\right) \end{aligned} \tag{4.37}$$

in which

$$d\frac{\partial f}{\partial \tau} = \frac{\partial^2 f}{\partial \tau^2} \cdot d\Delta\tau = M \cdot d\Delta\tau \tag{4.38}$$

Substituting the Eq. (4.38) into (4.37) and solving for $d\Delta\tau$

$$d\Delta\tau = k_{E,2} \cdot \left(d\Delta s - d\Delta\lambda \frac{\partial f}{\partial \tau}\right) \tag{4.39}$$

being $d\Delta\lambda$ the linearized plastic multiplier.

Based on the first-order differential form of the consistency condition, the linearized tangential format of the plastic multiplier $d\Delta\lambda$ can be derived as

$$df = \frac{\partial f}{\partial \tau} \cdot d\Delta\tau + \frac{\partial f}{\partial \kappa}\frac{\partial \kappa}{\partial s^p} \cdot d\Delta s^p = 0 \tag{4.40}$$

where the differential form of the plastic slip takes the following expression

$$d\Delta s^p = d\Delta\lambda \frac{\partial f}{\partial \tau} + \Delta\lambda \frac{\partial^2 f}{\partial \tau^2} \cdot d\Delta\tau \tag{4.41}$$

and substituting the Eqs. (4.41) and (4.39) into (4.40) and solving for $d\Delta\lambda$, the following

expression can be obtained

$$d\Delta\lambda = \frac{\frac{\partial f}{\partial \tau}\cdot k_{E,2} + \Delta\lambda\left(\frac{\partial f}{\partial \kappa}\frac{\partial \kappa}{\partial s^p}\right)\cdot\frac{\partial^2 f}{\partial \tau^2}\cdot k_{E,2}}{\left(\frac{\partial f}{\partial \tau}\right)^2\cdot k_{E,2} + H}\cdot d\Delta s \tag{4.42}$$

in which the scalar hardening parameter H assumes the following expression

$$H = -\left[\frac{\partial f}{\partial \tau_y}\frac{\partial \tau_y}{\partial \kappa}\frac{\partial \kappa}{\partial s^p}\right]\cdot\left[\frac{\partial f}{\partial \tau} - \Delta\lambda\frac{\partial^2 f}{\partial \tau^2}\cdot k_{E,2}\cdot\frac{\partial f}{\partial \tau}\right]. \tag{4.43}$$

Substituting $d\Delta\lambda$ into Eq. (4.39), the constitutive law and the algorithm tangent operator k^{ep}_{tan} can be obtained

$$d\Delta\tau = k_{E,2}\left(1 - \frac{\left(\frac{\partial f}{\partial \tau}\right)^2\cdot k_{E,2} + \Delta\lambda\frac{\partial f}{\partial \tau}\left(\frac{\partial f}{\partial \kappa}\frac{\partial \kappa}{\partial s^p}\right)\cdot\frac{\partial^2 f}{\partial \tau^2}\cdot k_{E,2}}{\left(\frac{\partial f}{\partial \tau}\right)^2\cdot k_{E,2} + H}\right)\cdot d\Delta s \tag{4.44}$$

in compact form:

$d\Delta\tau = k^{ep}_{tan}\cdot d\Delta s.$

4.4.3 Shear-slip test

The example proposed in this section outlines the interface response under direct fracture mode II. A relative shear slip is applied at Gauss-point level to capture the fundamental behavior of the proposed model.

The parameters which control the numerical predictions are obtained by considering the elastic stiffness $k_E = 120\,MPa/mm$ and the initial shear strength $\tau_{y,0} = 2.2\,MPa$. Fig. 4.5 reports the tangential stress vs. relative slip plots for different values of the fracture parameter: $G_f = 0.05, 0.10, 0.15, 0.20$ and $0.25\,N/mm$, respectively. The elastic contact is already equal for each case until the yield stress in shear is reached. After the peak strength the shear-slip response depicts a descending exponential type of curves characterized by an asymptotic vanishing of the shear stress. The influence of the fracture energy, G_f, correctly captures an increment of the ductility as the fracture parameter increases.

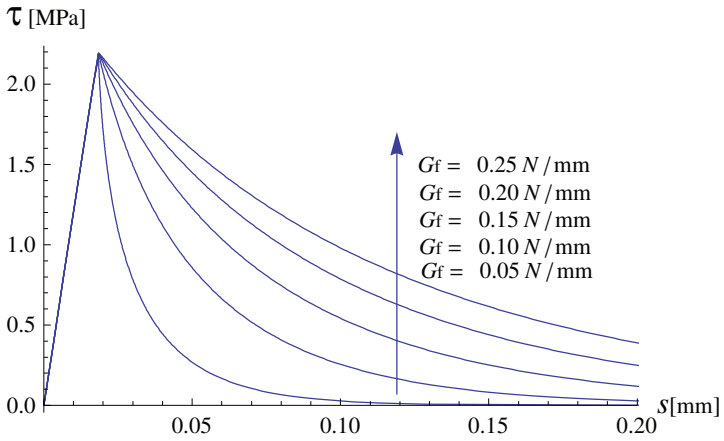

Figure 4.5: Bond-slip model: shear stress (τ) vs. relative slip (s) for different values of fracture energy G_f.

4.5 Comparison between numerical calculations and experimental results

This section presents a comparison between numerical simulations and experimental results. The effects of matrix strength, fiber length and diameter are analyzed in the following with the aim of emphasizing the predictive potential of the proposed unified formulation.

4.5.1 Effect of matrix strength and fiber anchorage

This section is mainly aimed at illustrating the numerical predictions obtained by applying the proposed model to the experimental tests reported by Shannag et al. [1997]. The bond behavior of steel fibers embedded in two different cementitious matrices is investigated for: (i) High Strength cement based Matrix (HSM) characterized by a compressive strength of 150 MPa and (ii) Conventional mortar (CSM) with compressive strength of 40 MPa.

Three different fiber anchoring lengths are also considered: i.e., $l_{emb} = 6\,mm$, $12\,mm$ and $18\,mm$, respectively. Smooth steel fibers, having a tensile strength of 2990 MPa, a module of elasticity of 200 GPa with diameter of $0.19\,mm$, were used by Shannag et al. [1997] and analyzed herein.

Numerical simulations are performed by considering the material interface parameters schematically described in Table 4.3. Non-linear FEM analyses are based on 20 trusses and 20 interface elements (Fig. 4.1) as optimal balance between accuracy and efficiency.

Several curve predictions in terms of load-displacement behavior at the loaded-end of the fiber under bond-slip are analyzed. Fig. 4.6 to 4.9 report the load-slip behavior for

Table 4.3: Model parameters according to the experimental tests by Shannag et al. [1997].

	Fracture – Based Model		Plasticity – Based Model	
CSM	$\tau_{y,0} = 2.2\,MPa$	$s_u = 1.56\,mm$	$\tau_{y,0} = 2.2\,MPa$	$s_u = 1.56\,mm$
	$k_E = 200\,MPa/mm$	$G_f = 2.42\,N/mm$	$k_E = 200\,MPa/mm$	$k_S = 1\,MPa/mm$
HSM	$\tau_{y,0} = 5.3\,MPa$	$s_u = 1.46\,mm$	$\tau_{y,0} = 5.3\,MPa$	$s_u = 1.46\,mm$
	$k_E = 1000\,MPa/mm$	$G_f = 23.41\,N/mm$	$k_E = 1000\,MPa/mm$	$k_S = 1.2MPa/mm$

both HSM and CSM.

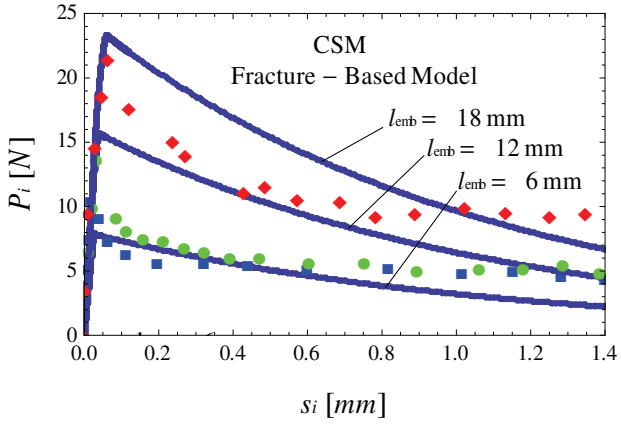

Figure 4.6: Fracture-based model results (continuous lines) vs. experimental data (square, circular and rhomboidal points) by Shannag et al. [1997] of the pull-out behavior on steel fibers from CSM.

The significant improvement (up to three times) of the bond strength in case of HSC, compared to conventional mortar, is well captured by the present models. The effect of the concrete kind is directly reflected on the bond-contact laws as outlined in Table 4.3. Particularly, it can be observed as the shear strength, $\tau_{y,0}$, increases in direct relation to the compressive strength of the surrounding matrix.

Furthermore, Figs. 4.6 to 4.9 show that the increment of the pull-out response is directly related to the anchoring length (varying from 6 to 18 mm). It can also be noted that the fracture-based model captures better the bond–slip process than the analytical bilinear relationship. Fig. 4.7 and 4.9 show as the results based on the analytical relationship and the FEM results are almost identical, this means that the mesh adopted is sufficient to reduce modeling errors due to the FE-discretization.

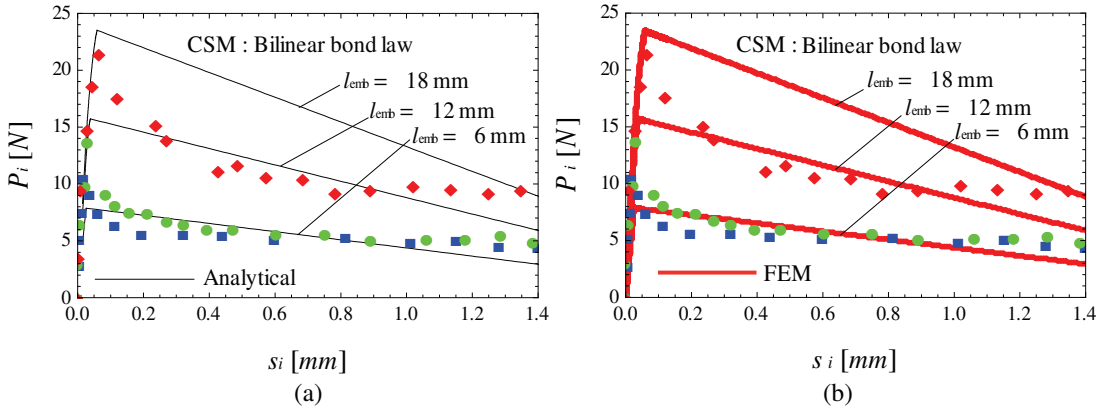

Figure 4.7: (a) Analytical and (b) FEM results (continuous lines) for bilinear $\tau - s$ against the experimental data (square, circular and rhomboidal points) by Shannag et al. [1997] of the pull-out behavior on steel fibers from CSM.

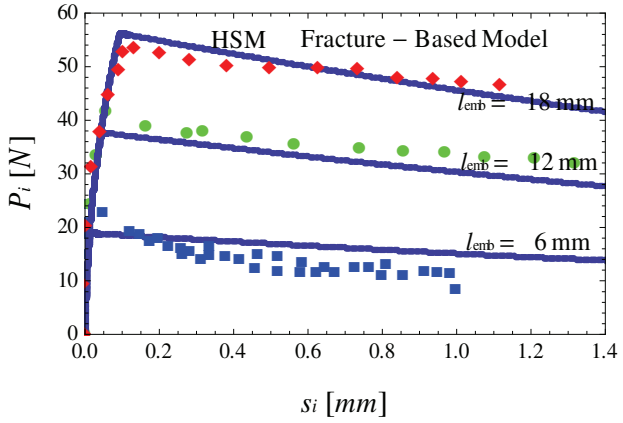

Figure 4.8: Fracture-based model results (continuous lines) vs. experimental data (square, circular and rhomboidal points) by Shannag et al. [1997] of the pull-out behavior on steel fibers from HSM.

4.5.2 Fiber anchorage and diameter effects.

This section presents some predictions using experimental data from pull-out tests which were carried out on steel fibers anchored in concrete systems. The fracture based model given in Section 4.4 is calibrated to predict the load displacement curves of straight and smooth steel fibers, with different diameters and anchoring lengths, tested under pull-out loads by Banholzer et al. [2006].

The following material parameters, dealing with an unified fracture-based $\tau - s$ rule, are employed for all predictions of this section: $\tau_{y,0} = 2.4\,MPa$, $s_u = 0.83\,mm$, $k_E = 120\,MPa/mm$ and $G_f = 0.80\,N/mm$. Numerical simulations are in good agreement with results observed in pull-out tests from Fig. 4.10 to 4.12. Load-slip curves are significantly affected by both fiber diameter which varies from $d_f = 0.8, 1.5$ and $2.0\,mm$, and the embedded

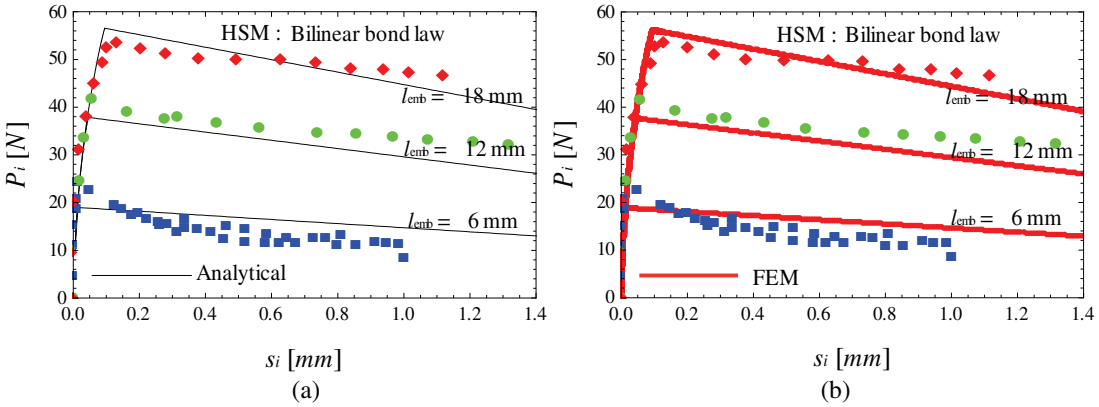

Figure 4.9: (a) Analytical and (b) FEM results (continuous lines) for bilinear $\tau - s$ vs. the experimental data (square, circular and rhomboidal points) by Shannag et al. [1997] of the pull-out behavior on steel fibers from HSM.

lengths, varying from $l_{emb} = 22.1, 27.1$ and $35.0\,mm$. The proposed procedure well captures the effects of both parameters.

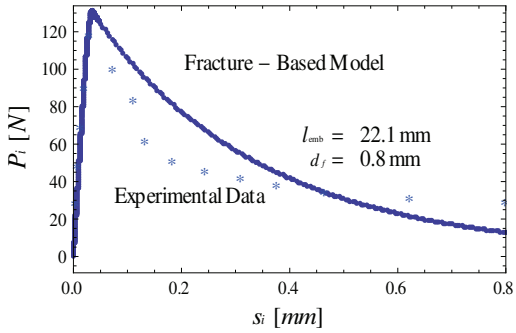

Figure 4.10: Fracture-based numerical prediction (continuous line) vs. experimental data (point lines) by Banholzer et al. [2006] for a steel fiber diameter of $0.8\,mm$ and an embedded length of $22.1\,mm$.

Only the fracture-based results are outlined and compared against the experimental evidence in this section. The bilinear bond-slip relationship posses, as demonstrated in Section 4.5.1, a minor prediction capability for pull-out tests, compared to the fracture-based proposal. For these reason that the numerical predictions realized by employing the bilinear bond-slip curve are not proposed in this section.

Finally, this discussion focuses on the detailed simulation of the complete debonding processes developing in the three cases whose overall response is described in Fig. 4.10 to 4.12. To this end, fiber-to-concrete shear stress and fiber strain distributions throughout the bond length are obtained by numerical simulations. Fig. 4.13 to 4.15 show such results for different values of bond length and diameter. In particular, Figs. 4.13b, 4.14b and 4.15b report the distribution of interface shear stresses throughout

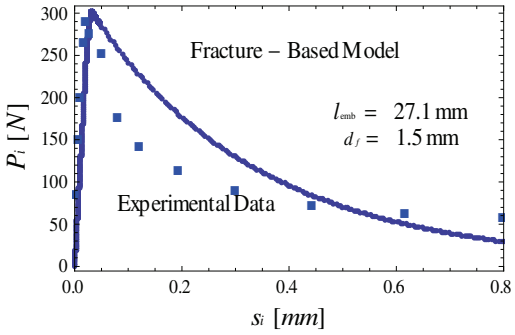

Figure 4.11: Fracture-based numerical prediction (continuous line) vs. experimental data (point lines) by Banholzer et al. [2006] for a steel fiber diameter of 1.5 mm and an embedded length of 27.1 mm.

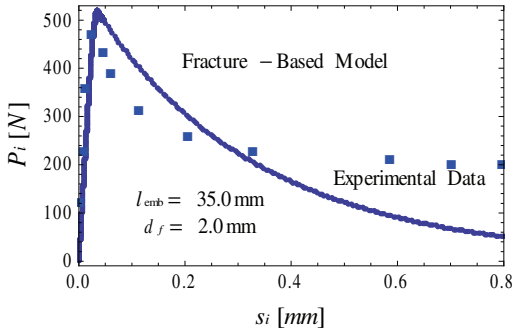

Figure 4.12: Fracture-based numerical prediction (continuous line) vs. experimental data (point lines) by Banholzer et al. [2006] for a steel fiber diameter of 2.0 mm and an embedded length of 35.0 mm.

the bond length for the same force levels labeled by the dots represented in Figs. 4.13a, 4.14a and 4.15a for the three specimens under consideration. Figs. 4.13c, 4.14c and 4.15c report the axial strain distribution, namely $\varepsilon_s[z] = \frac{ds}{dz}$, at each considered abscissa z of the analyzed steel reinforcement tested under pull-out: each curve refers at several force levels mentioned on the $P_i - s_i$ curves.

4.6 Closure chapter and some conclusions

This chapter presented a unified formulation for describing the overall tensile of fibers embedded in cementitious matrices. A series of final remarks can be drawn out on the bases of both the model formulation and the proposed applications:

- The proposed unified formulation is intended as a key element to be employed in the numerical model proposed in Chapter 3 aimed at explicitly simulating the mechanical behavior of FRCC by taking into account the discrete nature of such materials and the contributions of the various constituents within the framework

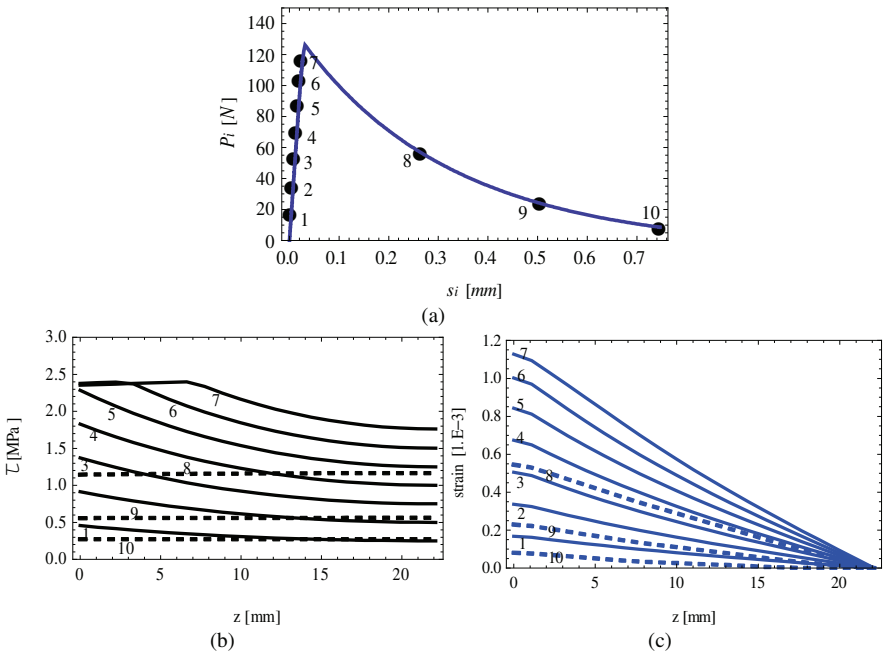

Figure 4.13: Pull-out numerical prediction for a steel fiber diameter of 0.8 mm and an embedded length of 22.1 mm by Banholzer et al. [2006]: (a) load-slip curve $P_i - s_i$, (b) interface shear stress distributions $\tau - z$ and (c) axial strain distributions $\varepsilon_s - z$.

of the so-called meso-mechanical approach;

- Two alternative constitutive models are proposed for obtaining the above mentioned formulation: i.e., the first one is based on the simpler elasto-plastic behavior with isotropic linear softening, while, the second one is founded on a more complex fracture energy-based contact model;

- The limits derived by assuming a simplified bilinear $\tau - s$ relationship for simulating the response of fibers under tensile stresses emerged in the final comparative analysis: although such a relationship allows for a fully analytical solution of the problem under consideration, it lacks in simulating the highly non-linear response which develops in the post-peak stage;

- Thus, a more complex, but more accurate fracture-based energy softening model is also presented and the key aspects of the numerical procedure needed for handling such a relationship are outlined;

- The solutions obtained by considering both models are validated against experimental results obtained on pull-out tests of smooth and straight steel fibers, currently available in the scientific literature;

- Both models demonstrated the capability of the proposed unified formulation to capture the key aspects of the complete pull-out response of fibers taking into

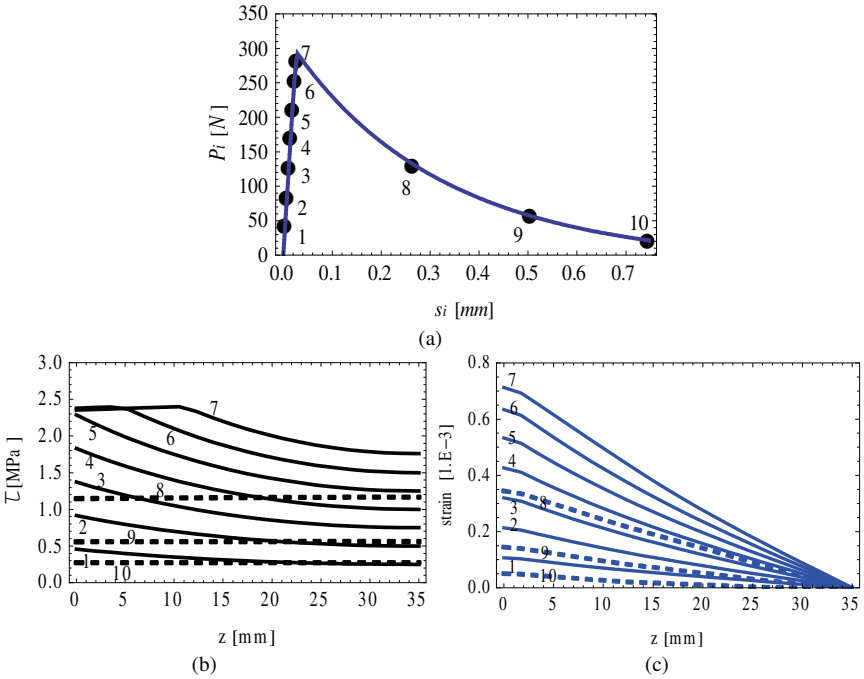

Figure 4.14: Pull-out numerical prediction for a steel fiber diameter of 1.5 mm and an embedded length of 27.1 mm by Banholzer et al. [2006]: (a) load-slip curve $P_i - s_i$, (b) interface shear stress distributions $\tau - z$ and (c) axial strain distributions $\varepsilon_s - z$.

account the possible influence of relevant parameters, such as bond length and fiber diameter.

As a final comment, it is worth noting that the proposed unified formulation can be straightforwardly employed in numerical models aimed at simulating the behavior of FRCC through a discrete-crack approach, as such model (i.e., meso-mechanical one) explicitly simulates the bond-slip response of fibers embedded in cementitious matrices. The adoption of the presented formulation within the framework of general meso-mechanical models of FRCC is, at the same time, the key motivation and the most relevant development of the present Chapter.

Besides the weaknesses described for the above mentioned bilinear relationship, numerical simulations are generally in good agreement with the corresponding experimental data. Also, the meso-scale formulation proposed by means of the zero-thickness interface formulation presented in Chapter 3 and then validated in the following Chapters (5 and 6), actually considers the bilinear proposal for the fiber debonding into the complete formulation for FRCC failure analysis.

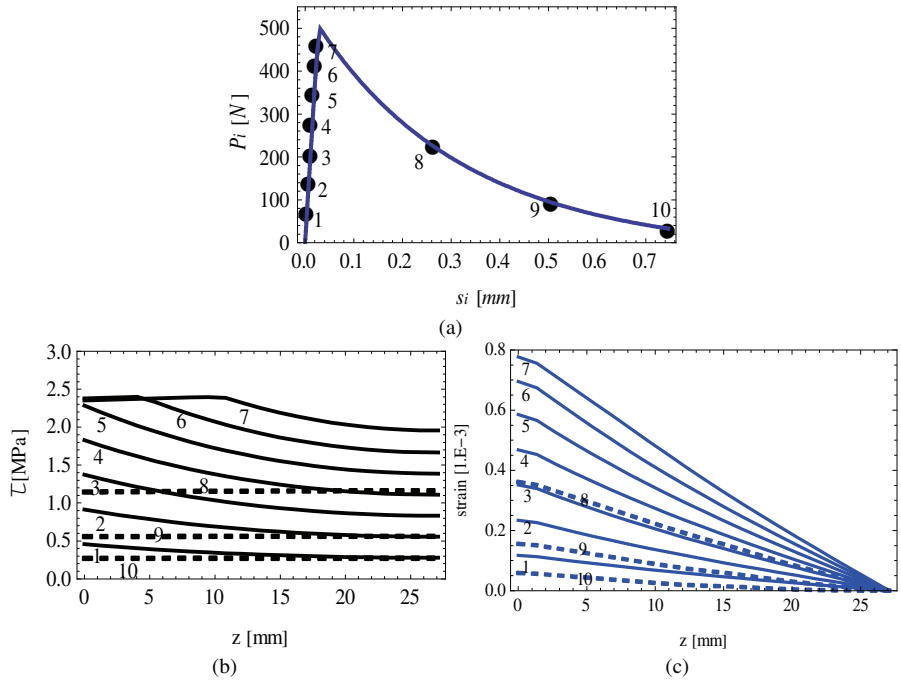

Figure 4.15: Pull-out numerical prediction for a steel fiber diameter of 2.0 mm and an embedded length of 35.0 mm by Banholzer et al. [2006]: (a) load-slip curve $P_i - s_i$, (b) interface shear stress distributions $\tau - z$ and (c) axial strain distributions $\varepsilon_s - z$.

5 Model performance and numerical predictions

This chapter proposes a preliminary calibration and some applications of the proposed interface model for FRCC failure analysis. Numerical simulations against available experimental test data are presented for investigating the soundness and capabilities of the proposed methodology.

5.1 Numerical analyses

For the calibration purpose, experimental results on Steel Fiber-Reinforced Concrete (SFRC) specimens, tested in pure tension, are considered while for the evaluation of model predictions, failure processes under mixed-modes of fracture, in plain and SFRC notched specimens, are taken into account.

5.1.1 Calibration of the interface model for SFRC

In this section, the interface model is calibrated by using experimental results performed on SFRC specimens tested in pure traction. One interface element, with different fiber contents, connecting two 4-node plane stress isoparametric elements is employed for this purpose. Particularly, the basic element patch, shown in Fig. 5.1, has been considered.

The number of fibers per interface is evaluated by means of the expression given by Krenchel [1975]

$$n_f = \alpha_{\vec{N}} \frac{\rho_f}{A_f} A_i \tag{5.1}$$

where ρ_f is the fiber content, $\alpha_{\vec{N}}$ is the orientation factor (assuming the value of 0.405 [Soroushian and Lee, 1990]), while A_f and A_i are the cross-sectional area of a single fiber and the interface area, respectively.

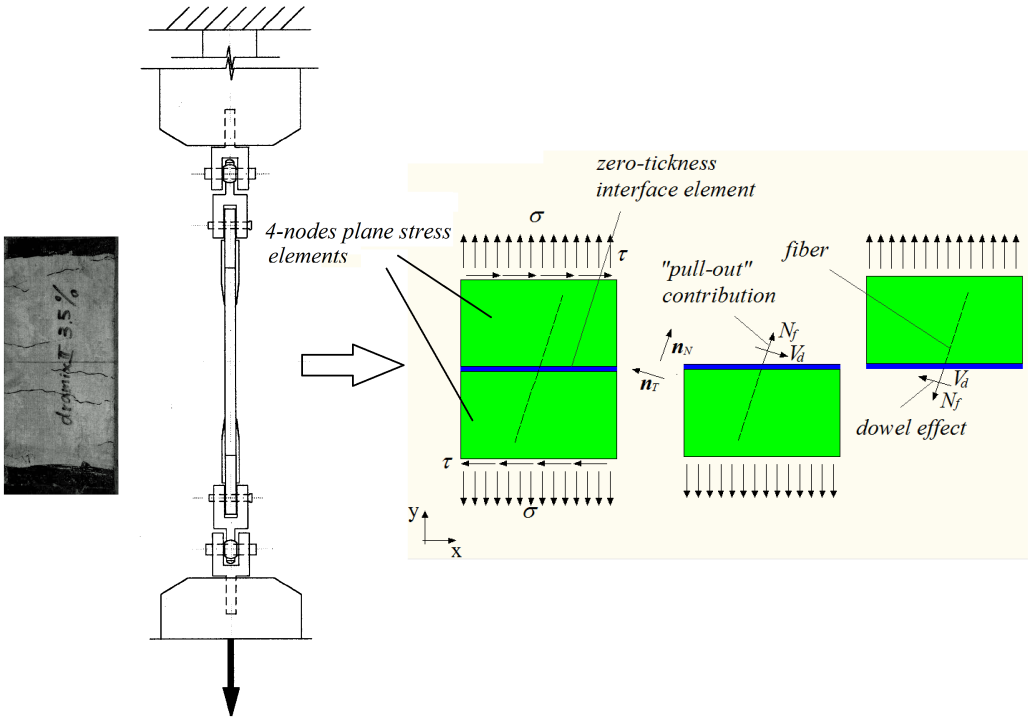

Figure 5.1: Test set-up of tensile tests performed by Li et al. [1998] and the corresponding analysis model.

The tensile tests on SFRC specimens, presented in Li et al. [1998], are firstly considered. Two different kinds of fibers, both with hooked ends, have been utilized as follow:

- **Dramix steel fibers** (diameter $d_f = 0.5\ mm$, length $l_f = 30\ mm$, density $\gamma_f = 7.8\ g/cm^3$, tensile strength $f_{fu} = 1.20\ GPa$ and $E_f = 200\ GPa$).
- **Harex steel fibers** (with arched cross section of area $= 2.2 \times 0.25\ mm^2$, length $l_f = 32\ mm$, density $\gamma_f = 7.8\ g/cm^3$, tensile strength $f_{fu} = 0.81\ GPa$ and $E_f = 200\ GPa$).

An indirect calibration of the numerical model has been performed to identify the model parameters, previously outlined in Chapter 3. The set of those parameters (i.e., the equivalent elastic modulus of fibers, E_d, the equivalent interface elastic limit, $\sigma_{y,d}$, and others mentioned in Chapter 3), collected in the vector $\mathbf{q}$, have been derived by the following least-square procedure

$$\bar{\mathbf{q}} = \arg\min_{\mathbf{q}} \left[\sum_{i=1}^{n} \left(\sigma_{th}\left[\varepsilon_{\exp,i}; \mathbf{q}\right] - \sigma_{\exp,i} \right)^2 \right] \tag{5.2}$$

being $\sigma_{th}\left[\varepsilon_{\exp,i}; \mathbf{q}\right]$ the model prediction of the tensile stress corresponding to the

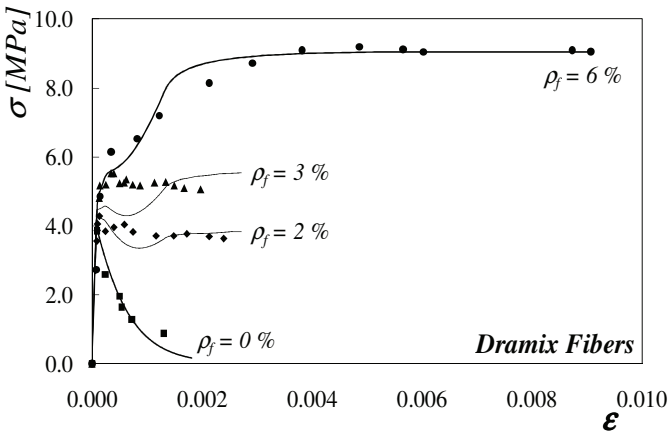

Figure 5.2: Experimental data [Li et al., 1998] and numerical simulation for SFRC with *Dramix* fibers.

experimental strain $\varepsilon_{\text{exp,i}}$ and the set of internal parameters $\mathbf{q}$, while $\sigma_{\text{exp,i}}$ is the corresponding experimental stress. In Eq. (5.2), n represents the number of available tensile stress measurements of the considered experimental test.

For the least-square calibration of the model parameters, experimental data on SFRC by Li et al. [1998] for both *Dramix* and *Harex* type of steel fibers were considered. The case of plain concrete was also included in the calibration analysis. The parameters of the proposed model, optimally adjusted according to the Eq. (5.2), include the elastic parameters of the rigid continuum elements representing the mortar matrix: $E_c = 37\,GPa$ and $\nu = 0.18$. The parameters of the inelastic interface result: $k_N = 1000\,MPa/mm$, $k_T = 200\,MPa/mm$, $\tan\phi_0 = \tan\beta = \tan\phi_r = 0.6$, $\chi_0 = 4.0\,MPa$, $c_0 = 7.0\,MPa$, $G_f^I = 0.12\,N/mm$, $G_f^{IIa} = 1.2\,N/mm$, $\sigma_{dil} = 10\,MPa$, $\alpha_\chi = -0.15$. The remaining interface parameters are considered null.

Some of the fiber parameters are derived by the main mechanical parameters of the component materials, while the others were obtained with the above indicated calibration procedure. In summary, fiber parameters result: $E_d = E_s$, $\sigma_{y,d} = 18\%\ \sigma_{y,s}$, $k_c = 440N/mm^3$, $\alpha_f = 7.7$ and $H_s = H_d = H_{dow} = 0$.

The available experimental results of direct tensile tests, represented by dotted lines in Figs. 5.2 and 5.3, are compared with the corresponding model predictions represented by continuous ones. The plotted stresses and strains in the model prediction (continuous curves of Figs. 5.2 and 5.3) correspond to their average amounts in the single-crack model of Fig. 5.1.

Particularly, in Figs. 5.2 and 5.3 the experimental results by Li et al. [1998] are compared with the corresponding numerical simulations performed through the calibrated numerical model. Specimens reinforced with either *Dramix* or *Harex* fibers are con-

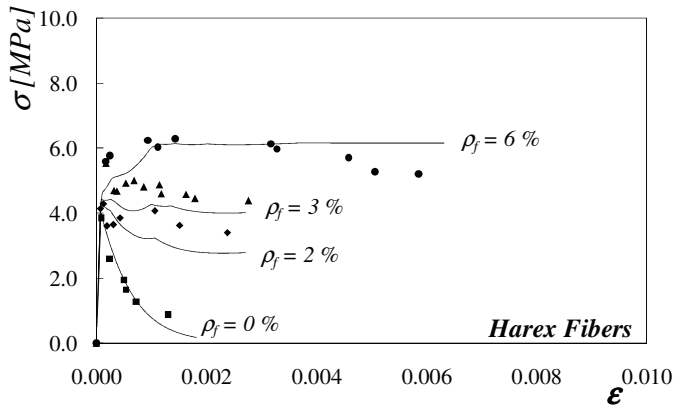

Figure 5.3: Experimental data [Li et al., 1998] and numerical simulation for SFRC with *Harex* fibers.

sidered with fiber contents (ρ_f = 0, 2, 3 and 6%). The results in those figures show that the proposed interface model, with the internal parameters indicated above, leads to accurate predictions of SFRC failure behavior in the direct tensile test when low, medium and high fiber contents are considered.

Beyond the general accuracy of the model predictions and, consequently, the soundness of its assumptions and formulation, the results in Fig. 5.2 and 5.3 emphasize the strong dependency of FRCC mechanical behavior on the fiber content and quality. A progressive transition from the brittle failure mode characterizing the behavior of plain concrete in tension to a more and more ductile post-peak response can be clearly recognized when the fiber content increases.

The diagrams in Figs. 5.2 and 5.3 show the different behaviors of SFRC based on *Dramix* and *Harex* fibers, both hooked at the end. The more ductile performance shown in Fig. 5.2 is probably due to the fact that the volume of the single *Dramix* fiber is significantly smaller (almost three times [Li et al., 1998]) than that of *Harex* types (Fig. 5.3). Consequently, a significantly higher number of fibers are present in the first specimens (for the same considered fiber content) resulting in a more homogeneous material.

5.1.2 Predictive analysis of SFRC failure behavior under mixed-modes of fracture

To asses the predictive capability of the model in terms of failure behavior of SFRC specimens, the stress history on plane concrete panels by Hassanzadeh [1990] are considered in this subsection.

These experimental tests were performed on prismatic concrete specimens of 0.07×0.07

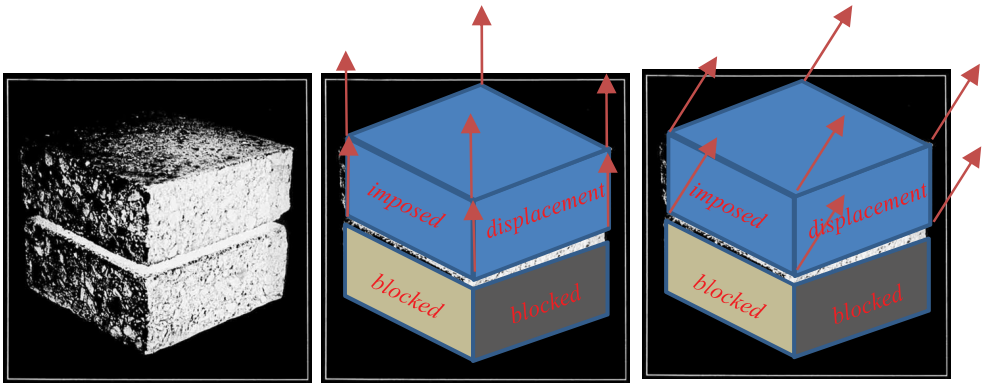

(a) (b) (c)

Figure 5.4: Test set-up of notched specimen performed by Hassanzadeh [1990]: (a) concrete sample, (b) tensile load in the first part of the test and (c) mixed fracture displacements co-imposed in the second part of the experiment.

m^2 cross section with a 0.015 m deep notch along their perimeters (Fig. 5.4a). Both normal and transverse relative displacements are co-imposed to the two parts of the notched specimen with the aim of reproducing the cracking processes in concrete under mode I and II types of fracture depending on the angle between the two imposed displacement components. During the first part of these tests only normal tensile displacements u are applied, as in Fig. 5.4b, until the peak strength is reached. In the second part of the test (Fig. 5.4c), tensile displacements are combined with transverse ones, applied on the upper part of the notched specimen, and defining a pre-fixed angle (namely, $\tan\theta = u/v$).

For the numerical analysis of the Hassanzadeh [1990] tests, the FE-discretization and boundary conditions shown in Fig. 5.5 are considered. Four different cases were evaluated with $\theta = 90^o$, 75^o, 60^o, 30^o and in each case zero ($n_f = 0$), ten ($n_f = 10$), twenty ($n_f = 20$) and thirty ($n_f = 30$) steel fibers, crossing the joint element, were considered.

The interface model parameters, calibrated starting from the experimental data by Hassanzadeh [1990], are: $k_N = 500\ MPa/mm$, $k_T = 200\ MPa/mm$, $\tan\phi_0 = \tan\beta = \tan\phi_r = 0.6$, $\chi_0 = 2.8\ MPa$, $c_0 = 7.0\ MPa$, $G_f^I = 0.08\ N/mm$, $G_f^{IIa} = 10\,G_f^I = 0.8\ N/mm$, $\sigma_{dil} = 15\ MPa$. All remaining parameters, characterizing the interface model, are considered null. For the continuum elements, the elastic parameters $E_m = 25\ GPa$ and $\nu = 0.2$ were considered, representing the Young modulus and Poisson's ratio, respectively. *Dramix* fibers were used in those analyses characterized with the same parameters given in subsection 5.1.1.

Fig. 5.6 shows the results with different number of fibers corresponding to the uniaxial tensile test ($\theta = 90^o$). It can be clearly observed that the model is able to simulate the increment in both ductility and energy released when the number of fibers increase.

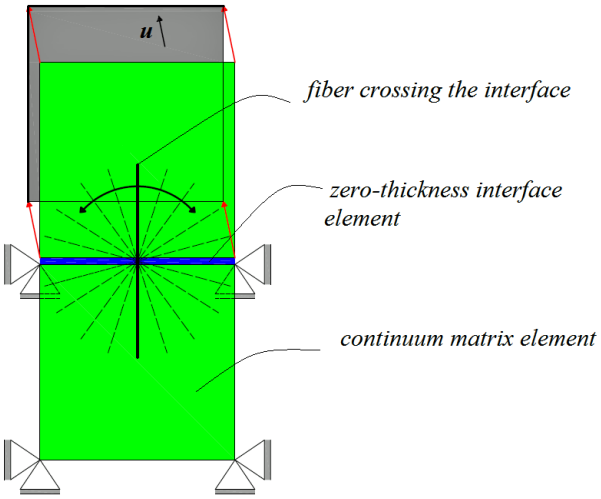

Figure 5.5: Boundary conditions and FE-discretization with one single interface crossed by short fibers for Hassanzadeh [1990] tests on SFRC panels.

Figs. 5.7a, 5.8a and 5.9a show the model predictions in terms of normal stresses vs. displacements ($\sigma - u$) of Hassanzadeh [1990] experiments for $\theta = 75^o$, 60^o and 30^o, respectively. As it can be observed, the combined action of normal and shear displacements causes a more pronounced softening branch in post-peak regime. The tensile strength tends to zero more rapidly and, moreover, changes its sign becoming a compressive stress, due to the fact that the normal dilatancy, produced by the applied shear displacements, exceeds the fixed normal opening rate.

The inclusion of steel fibers leads to an increment of the tensile strength, but also of the ductility in post-peak regime. Simultaneously, the compression branch of the normal stress continuously reduces and then disappears. In other word, the steel fibers reduce the material dilatancy.

Figs. 5.7b, 5.8b and 5.9b report the shear stresses against the relative transverse displacements. The significant influence of fiber content on both peak stress and post-peak toughness can be (again) easily recognized.

The simulation of the interface model in this section demonstrates the capability of the proposed formulation to capture the variation of stiffness, strength, ductility and the overall behavior of concrete due to the presence of steel fibers in both pure tensile failure mode as well as under mode II type of fracture with different levels of confinement pressure (originated by constraining the dilatancy of both plain and fiber concretes).

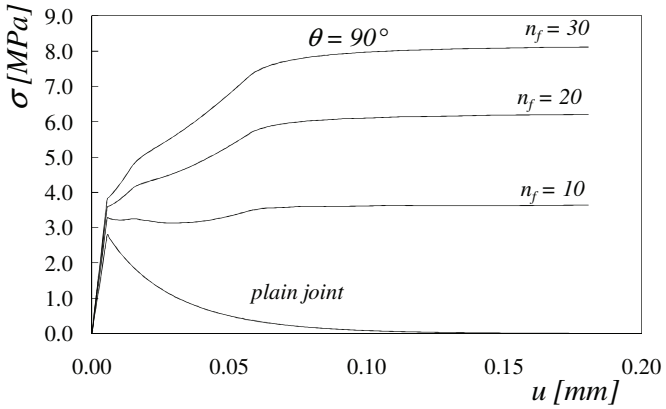

Figure 5.6: Normal stress vs. relative vertical displacement performed with different amount of fibers and $\theta = 90^o$.

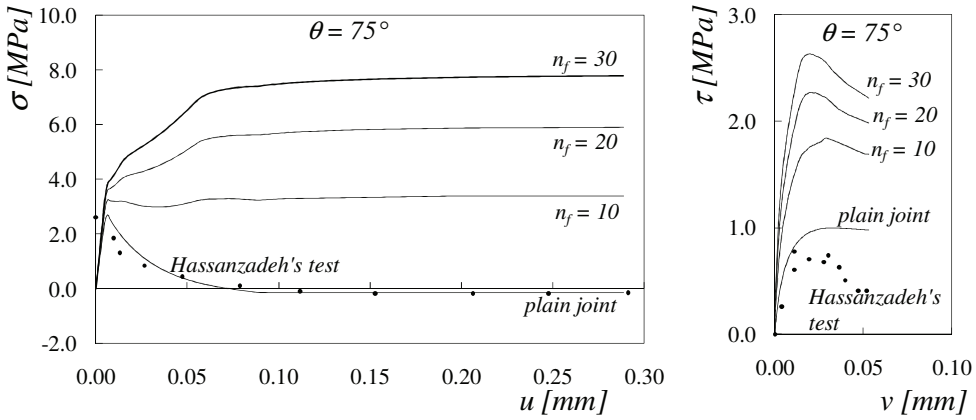

Figure 5.7: Hassanzadeh [1990] tests with different number of fibers and $\theta = 75^o$: a) normal stress vs. relative normal displacement and b) shear stress vs. relative tangential displacement.

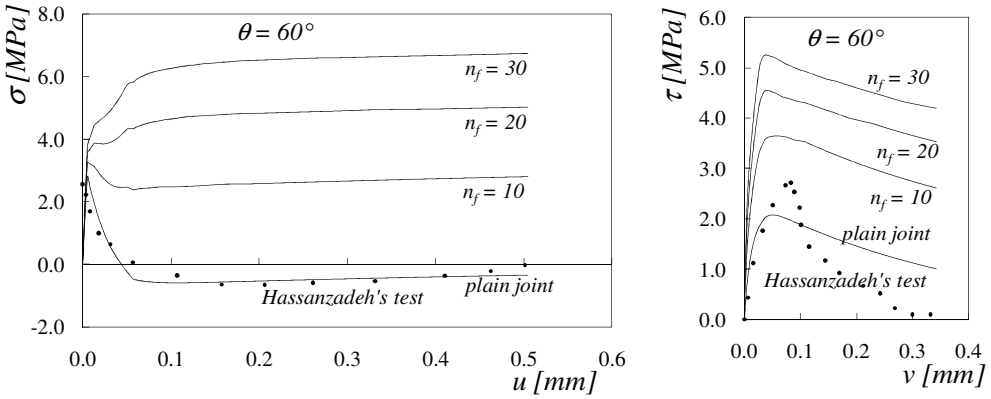

Figure 5.8: Hassanzadeh [1990] tests with different number of fibers and $\theta = 60^o$: a) normal stress vs. relative normal displacement and b) shear stress vs. relative tangential displacement.

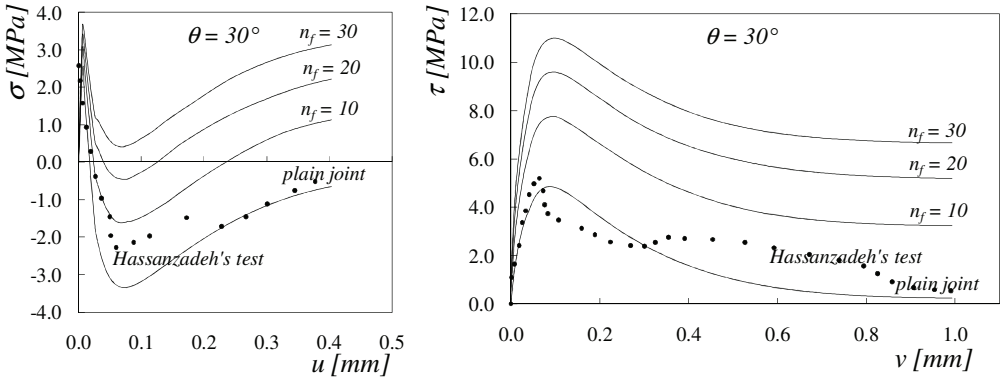

Figure 5.9: Hassanzadeh [1990] tests with different number of fibers and $\theta = 30^o$: a) normal stress vs. relative normal displacement and b) shear stress vs. relative tangential displacement.

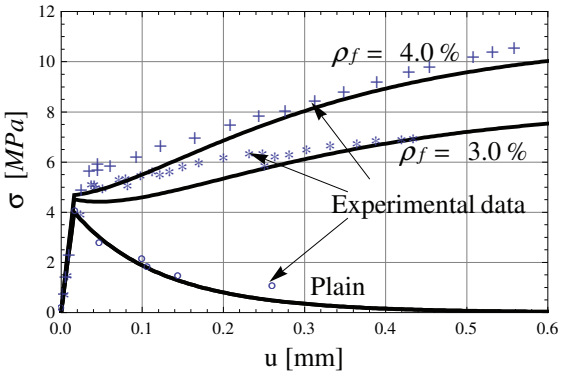

Figure 5.10: Comparison between numerical predictions and experimental results by Li and Li [2001]: SFRC with "Dramix type II" fibers.

5.1.3 Parametric study

The parametric analyses presented in this section are performed by means of the two linear elastic four node FEs connected by one interface element, which FE set-up and boundary conditions are given in the above subsection as shown in Fig. 5.5. Therefore, the results are directly related to the interface model predictions.

Fiber length

The considered experiments on SFRC contain two different fiber types, namely "Dramix type I" and "type II", whose fundamental characteristics are given in Table 5.1. The model parameters, considered in these numerical analyses and adjusted according to the experimental data given in Li and Li [2001], are: $k_N = 98.75\,GPa$, $k_T = 32.92\,GPa$, $\tan\phi_0 = \tan\beta = \tan\phi_r = 0.6$, $\chi_0 = 4.0\,MPa$, $c_0 = 7.0\,MPa$, $G_f^I = 0.12\,N/mm$, $G_f^{IIa} = 1.2\,N/mm$. On the other hand, the considered parameters for the fiber-to-concrete interaction mechanisms are: $\tau_{y,a} = 1.95\,MPa$, $k_E = 52.5\,MPa/mm$ and $k_S = 1.70\,MPa/mm$ for the bond-slip strength; $\kappa_1 = 6.5$, $f_c = 10 \cdot \chi_0$ and $k_{dow} = 0.23$ for the dowel effect. The indirect calibration procedure outlined in subsection 5.1.1 was performed to identify the model parameters above outlined.

Table 5.1: Fiber types employed in the experimental tests by Li and Li [2001].

	Density $[g/cm^3]$	$d_f\,[mm]$	$l_f\,[mm]$	$\sigma_{y,s}\,[GPa]$	$E_s\,[GPa]$
Dramix type I	7.8	0.5	30	1.20	200
Dramix type II	7.8	0.5	50	1.20	200

Model predictions are compared with the experimental data by Li and Li [2001]. The comparisons in terms of force-displacement diagrams are shown in Figs. 5.10 and 5.11.

Particularly, the stress-crack opening response for SFRC with steel "Dramix type II"

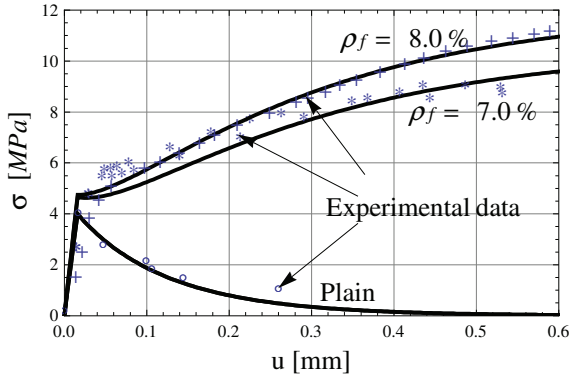

Figure 5.11: Comparison between numerical predictions and experimental results by Li and Li [2001]: SFRC with "Dramix type I" fibers.

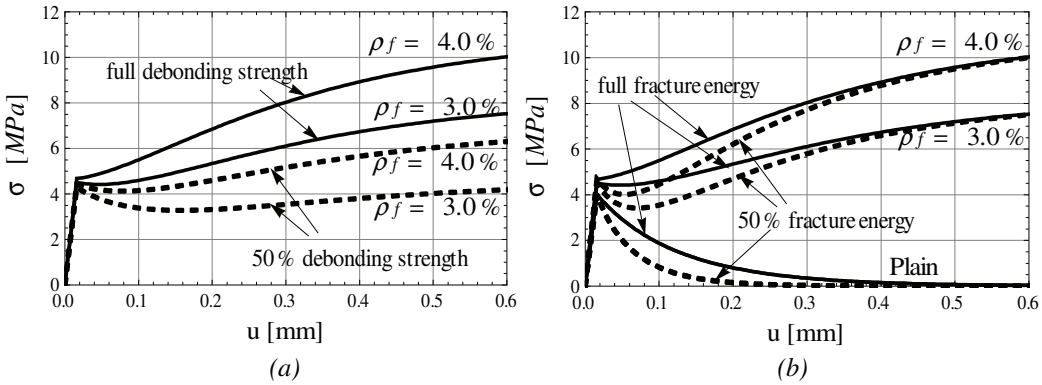

Figure 5.12: Comparison between the numerical predictions of the test by Li and Li [2001] on SFRC with "Dramix type II" fibers: (a) full debonding vs. 50% of the debonding strength and full fracture energy G_f^I, (b) full debonding strength and 100% vs. 50% of G_f^I.

fibers, and fiber contents of 3.0% and 4.0%, are given in Fig. 5.10. While Fig. 5.11 shows numerical and experimental comparisons of stress-crack opening displacements of tests on SFRC with "Dramix type I" fibers, and fiber contents of 7.0% and 8.0%.

The numerical predictions compared against experimental results demonstrate a very good agreement. Actually, the interface model is able to realistically reproduce the overall response behaviors of SFRC.

It should be noted that all previous numerical predictions have been obtained by just changing the fiber contents (ρ_f) and/or fiber types (changing the l_f value), according to the experimental properties. No particular further calibrations or adjustments were required for each test.

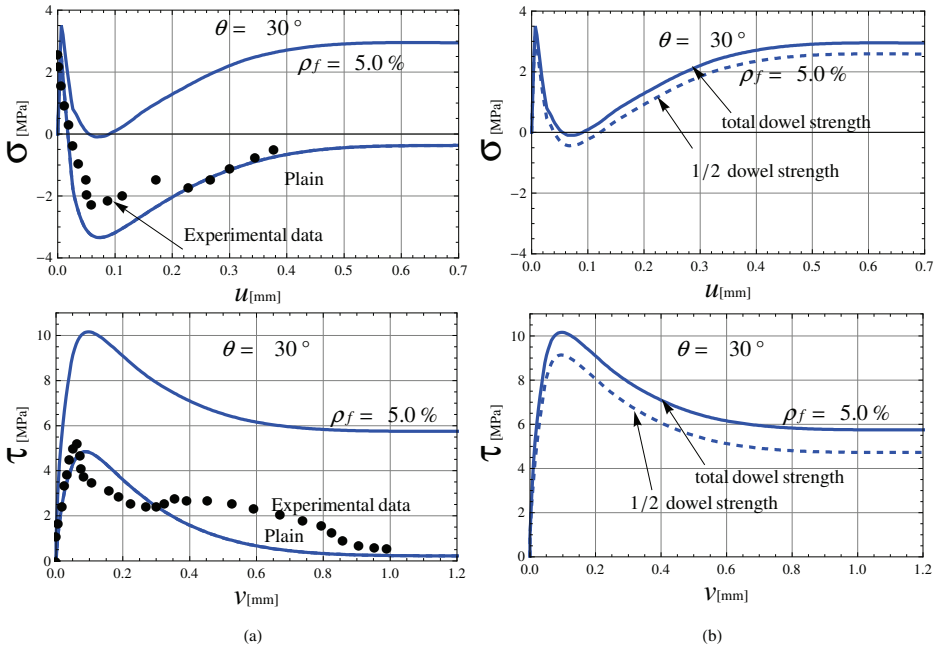

Figure 5.13: (a) Experimental test by Hassanzadeh [1990] and numerical prediction for SFRC with "Dramix type I" fibers, with $\rho_f = 5.0\%$ and, (b) effect of the dowel strength on the stress-opening displacements in mixed-modes of fracture.

Debonding strength

Stress-crack opening predictions of SFRC with steel "Dramix Type II" fibers are evaluated when full and 50% of the debonding strength capacity of steel fibers to concrete are considered. This results, depicted in Fig.5.12 (a), clearly illustrate the capability of the interface model to realistically reproduce the incidence of the main parameter governing the interaction between concrete and steel fiber in mode I type of fracture.

Fracture energy release

In Fig. 5.12 (b), the stress-crack opening behavior of the same experiment on SFRC is illustrated, but corresponding to the case when only 50% of the concrete fracture energy release in mode I is considered. As can be observed from Fig. 5.12 (a) and (b) the interface model is able to capture the influence of fundamental properties of the constituents in the overall response behavior.

Dowel strength

Finally, the stress history on concrete panels by Hassanzadeh [1990] is evaluated as it activates failure processes under both mode I and II types of fracture. These experimental tests are performed on prismatic concrete specimens of $0.07 \times 0.07\ m^2$ cross

section with a 0.015 m deep notch along their perimeters. Both normal and transverse relative displacements are co-imposed on the upper border of the notched specimen while the remaining borders are fixed with the aim of reproducing cracking processes in concrete under mode I and II types of fracture. During the first part of these tests only normal tensile displacements u are applied until the peak strength is reached. Then, tensile displacements are combined with transverse ones v defining a prefixed load angle ($\tan\theta = u/v$).

Fig. 5.13 (a) shows the model predictions in terms of $\sigma - u$ and $\tau - v$ curves, analyzing the case in which $\theta = \pi/6$ on both plain and SFRC concrete panels. The proposed application consider the model parameters previously calibrated and given in subsection 5.1.2. Numerical analyses demonstrate on the one hand, the very good agreement of the numerical prediction with the plain interface regarding the experimental results on plain concrete tests by Hassanzadeh [1990]. On the other hand, the results also illustrate the significant influence of fiber reinforcements on the peak strength and post-peak ductility of the concrete panel response (when $\rho_f = 5.0\%$).

Fig.5.13 (b) deals with the stress-crack opening predictions of SFRC when a reduction of the 50% for the dowel strength is considered. Model predictions mainly capture the fundamental influence of the dowel effect on the overall response behavior under mixed failure modes. As expected, the dowel effect controls the transverse interaction between concrete and steel fiber in this complex failure mode.

No experimental results are currently available in scientific literature related to the Hassanzadeh type tests on SFRC. Nevertheless, the numerical results here presented, provide realistic predictions of peak stresses, ductility and post-peak behavior of SFRC tested in mixed fracture modes like the ones in the Hassanzadeh [1990] tests.

5.2 Cracking analysis of the proposed interface model for FRCC

This section is aimed at analyzing the incidence of steel fibers on the post-cracking performance for several stress states (lying on the initial yielding surface) under overall possible failure modes. As a matter of principle, the method herein applied could be intended as a similar approach as used for continuum-based models, where the localization analysis is mainly performed by employing the analytical solution of the classical discontinuous bifurcation condition [Folino, 2012]. In principle, strong differences can be noted between the localized failure analyses of classical continuum approaches compared with the discontinuous analysis outlined in this section. However, in several aspects and conclusion both procedures are quite similar.

A large amount of numerical results are presented in this section. They are based on the cracking analysis by considering different SFRC qualities and load scenarios. The results illustrate a wide range of failure modes which characterize the post-peak response

of both plain and SFRC when different stress histories and stages are considered. A dimensionless "cracking indicator" is discussed and analyzed.

5.2.1 Post-cracking behavior

An extensive post-cracking analysis is proposed, based on the FRCC interface model outlined in the previous chapters. For this purpose, several interface cracking conditions are considered for different load scenarios. In this analysis the "cracking indicator" (CI) defined as

$$CI(\theta,\rho) = \frac{\boldsymbol{N}^t \cdot \boldsymbol{E}^{ep} \cdot \boldsymbol{N}}{\boldsymbol{N}^t \cdot \boldsymbol{E} \cdot \boldsymbol{N}} \tag{5.3}$$

being θ (with $\tan\theta = u/v$) the initial cracking angle (Fig. 5.14) and $\boldsymbol{N}$ the unit vector, defining the normal of a potential cracking direction, expressed as

$$\boldsymbol{N} = [N_1, N_2]^t = [\cos(\rho), \sin(\rho)]^t \tag{5.4}$$

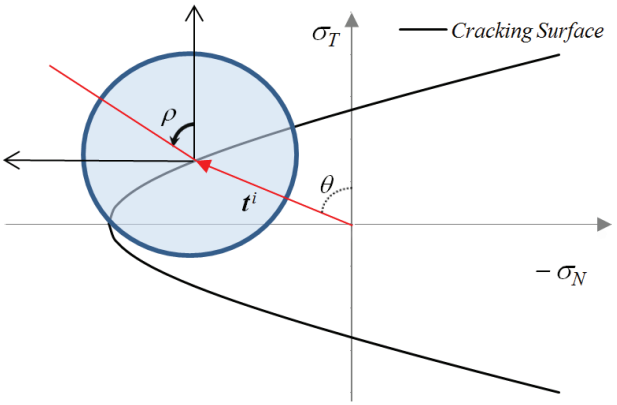

Figure 5.14: ρ and θ angles defined in the interface stress space.

The angles ρ is depicted in Fig. 5.14 and describes the set of all possible vectors $\boldsymbol{N}$ of the failure surface. $\boldsymbol{E}^{ep}$ and $\boldsymbol{E}$ are the constitutive tangent operator and the elastic one, respectively, defined in Chapter 3. The superscript ^{t} deals with the transposition vectorial operation.

The performance of the "cracking indicator" is proposed in terms of the ρ-angle (between $\boldsymbol{N}$ and the σ_T direction, as depicted in Fig. 5.14). Particularly, $\rho = \frac{\pi}{2}$ indicates a pure tensile fracture mode path, while $\rho = 0$ outlines a direct shear without dilatancy. For any given θ angle, a particular value for ρ (labeled as critical one ρ_{cr}) exists for which the mentioned CI parameter assumes its minimum: ρ_{cr} defines the weakness direction of the considered composite interface.

5.2.2 Failure performance and cracking indicators for mixed fracture modes

In this subsection, the post-cracking analysis under mixed-modes condition and peak stress is presented. The analyses are performed for three different SFRC: i.e., plain concrete, Dramix steel fibers with 3.0 and 6.0%. All the numerical predictions refer to the calibrated tests proposed in Section 5.1.1. Different initial θ-angles, at peak stress under mixed-modes of fracture, are considered.

A set of six interface stress states are selected and analyzed for the three types of SFRC under consideration. These stress states are indicated on the maximum interface strength following the numeration of Fig. 5.15. Particularly, the considered stress states are listed below:

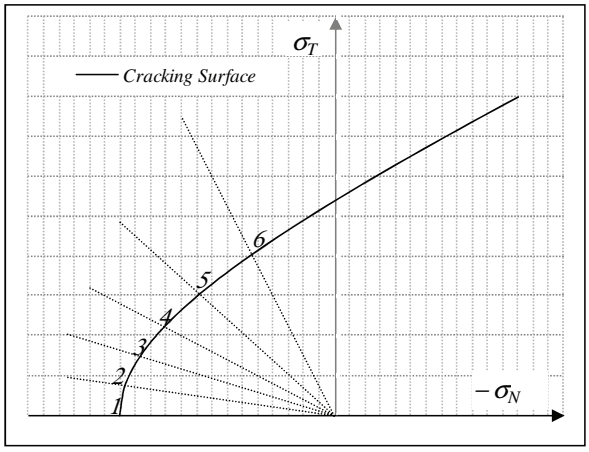

Figure 5.15: Schematic interface stress states selected for the post-cracking analysis.

- Point 1: Uniaxial Tensile (UT): $\frac{\sigma_N}{\sigma_T} = \frac{1}{0} \Longrightarrow \theta = \frac{\pi}{2}$;
- Point 2: Tension-Shear (TS2): $\frac{\sigma_N}{\sigma_T} = \frac{1}{2-\sqrt{3}} \Longrightarrow \theta = \frac{5\pi}{12}$;
- Point 3: Tension-Shear (TS3): $\frac{\sigma_N}{\sigma_T} = \frac{1}{\frac{1}{\sqrt{3}}} \Longrightarrow \theta = \frac{\pi}{3}$;
- Point 4: Tension-Shear (TS4): $\frac{\sigma_N}{\sigma_T} = \frac{1}{1} \Longrightarrow \theta = \frac{\pi}{4}$;
- Point 5: Tension-Shear (TS5): $\frac{\sigma_N}{\sigma_T} = \frac{1}{\sqrt{3}} \Longrightarrow \theta = \frac{\pi}{6}$;
- Point 6: Tension-Shear (TS6): $\frac{\sigma_N}{\sigma_T} = \frac{1}{2+\sqrt{3}} \Longrightarrow \theta = \frac{\pi}{12}$;

The results of these analyses, performed with the FRCC interface model at peak stresses, are presented in Fig. 5.16, while the same post-cracking performance results are also depicted in polar plots in Figs. 5.17, 5.18 and 5.19.

The critical angles, ρ_{cr}, at which the CI parameters assume its minimum values, for the above considered materials (plain concrete and FRCCs with Dramix steel fibers having the 3.0 and 6.0% of fiber content) are:

- Point 1: Uniaxial Tensile (UT): $\theta = \frac{\pi}{2} = 90°$, $\rho_{cr,PI} = 90°$, $\rho_{cr,3.0\%} = 90°$ and $\rho_{cr,6.0\%} = 90°$;
- Point 2: Tension-Shear (TS2): $\theta = \frac{5\pi}{12} = 75°$, $\rho_{cr,PI} = 83.15°$, $\rho_{cr,3.0\%} = 85.31°$ and $\rho_{cr,6.0\%} = 86.03°$;
- Point 3: Tension-Shear (TS3): $\theta = \frac{\pi}{3} = 60°$, $\rho_{cr,PI} = 76.65°$, $\rho_{cr,3.0\%} = 80.26°$ and $\rho_{cr,6.0\%} = 80.98°$;
- Point 4: Tension-Shear (TS4): $\theta = \frac{\pi}{4} = 45°$, $\rho_{cr,PI} = 67.99°$, $\rho_{cr,3.0\%} = 73.77°$ and $\rho_{cr,6.0\%} = 75.21°$;
- Point 5: Tension-Shear (TS5): $\theta = \frac{\pi}{6} = 30°$, $\rho_{cr,PI} = 57.17°$, $\rho_{cr,3.0\%} = 65.11°$ and $\rho_{cr,6.0\%} = 67.27°$;
- Point 6: Tension-Shear (TS6): $\theta = \frac{\pi}{12} = 15°$, $\rho_{cr,PI} = 43.47°$, $\rho_{cr,3.0\%} = 52.85°$ and $\rho_{cr,6.0\%} = 55.73°$.

where the subscript PI indicates the “Plain Interface”, while 3.0% and 6.0% outline the fiber percentages.

Observing these results, the following conclusions can be itemized:

- The first comment deals with the observation that CI assumes negative values only for plain concrete and in particular zone of the ρ angle. While, only positive CI characterize the SFRC specimens (Fig. 5.16). This is due to the post-cracking softening response of the unreinforced concrete, contrarily the SFRC with 3.0% and 6.0% of fiber contents are charactertized by a post-hardening crack opening behavior.
- In the case of UT-test, the angle θ (initial load angle) coincides with ρ_{cr} (angles at which the CI reaches its minimum value) for each type of composite: i.e., plain concrete and SFRCs. Practically, no difference was observed for the weak cracking directions in the considered concretes, resulting $\theta = \rho_{cr} = \frac{\pi}{2}$ for both plain and SFRC with 3.0% and 6.0% of fiber contents.
- The cracking indicator assumes the unity value when the stress increment deals with a pure elastic response of the considered interface law: the polar plot mainly outlines a curve as part of circle with a unitary radius. From a mechanical standpoint, these points represent stress increments in compression/shear states,

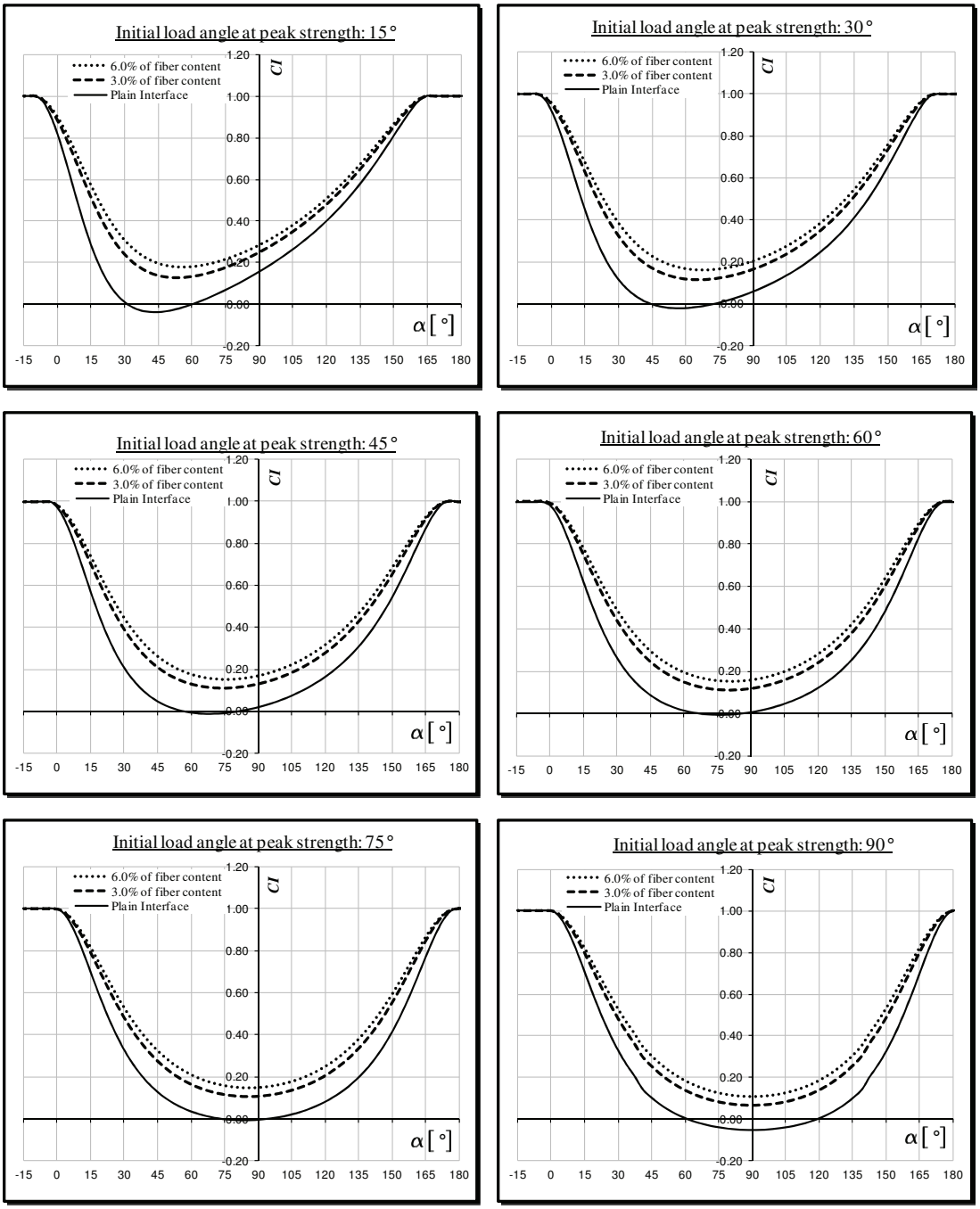

Figure 5.16: Post-cracking analysis at peak stress for different concrete types: plain concrete and SFRC with “Dramix type I” fibers having fiber contents of 3.0% and 6.0%.

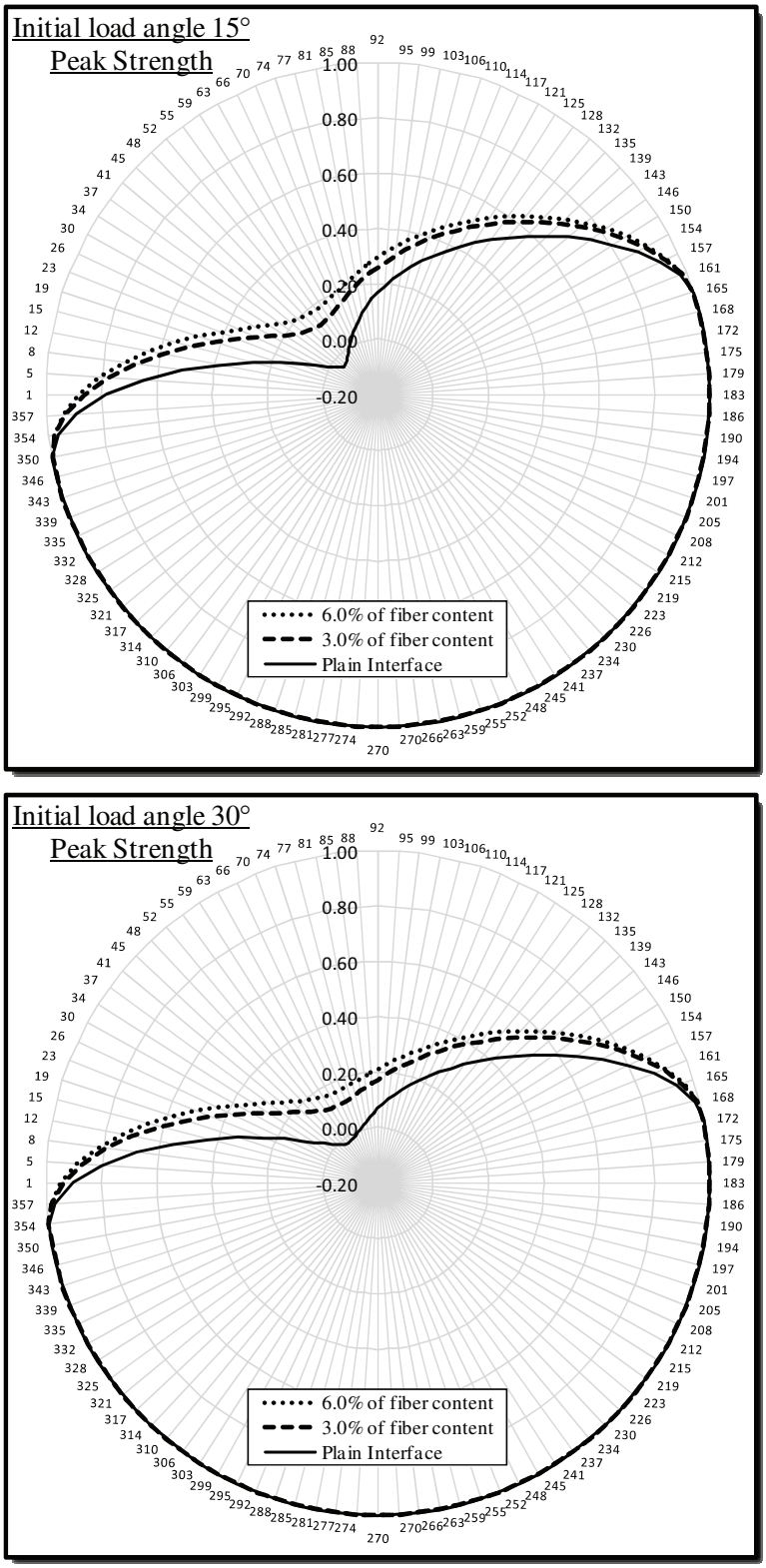

Figure 5.17: Polar plots of post-cracking analysis of TS5 and TS6 for different concrete types: plain concrete and SFRC with “Dramix type I” fibers having fiber contents of 3.0% and 6.0%.

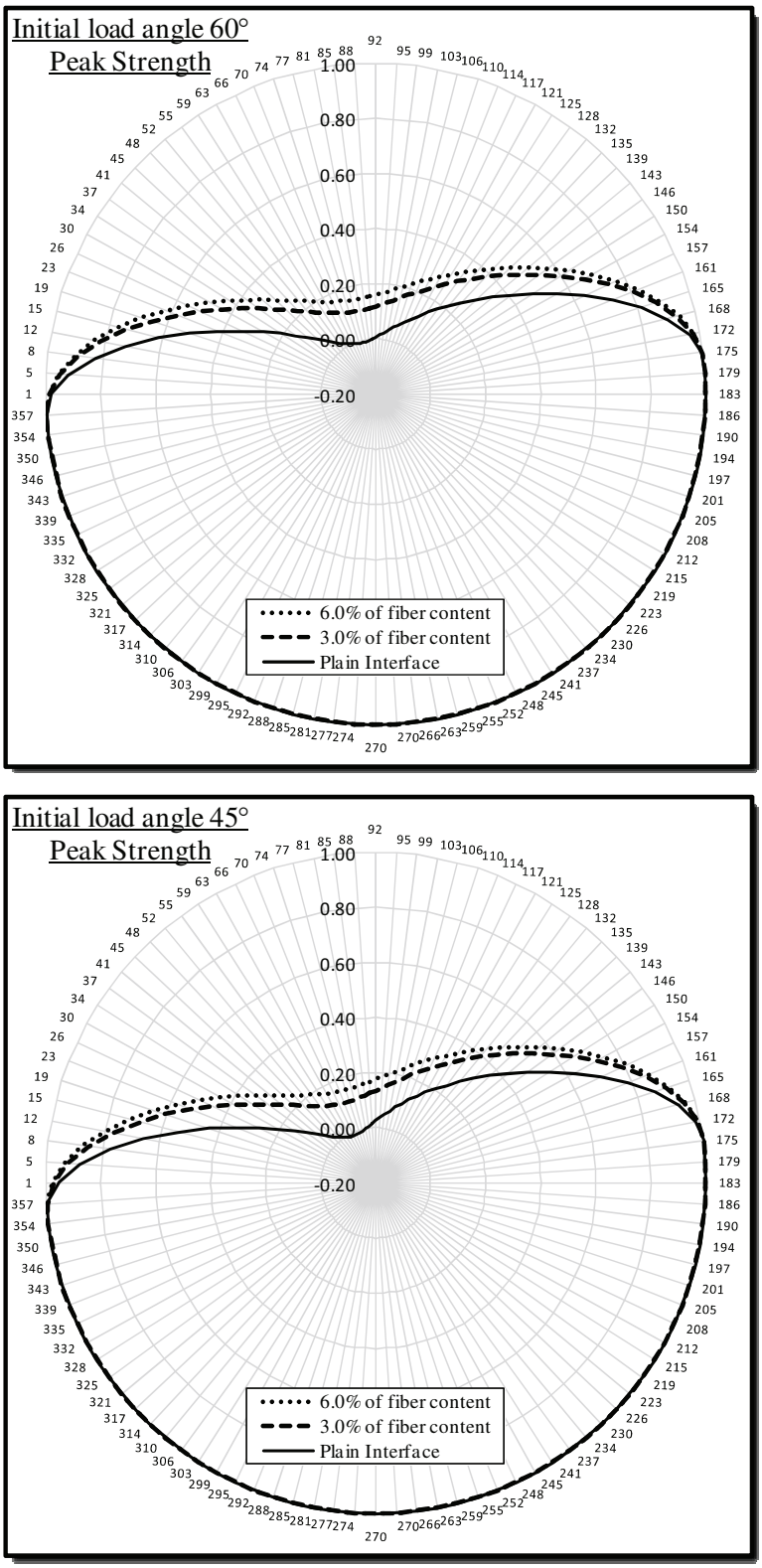

Figure 5.18: Polar plots of post-cracking analysis of TS3 and TS4 for different concrete types: plain concrete and SFRC with “Dramix type I” fibers having fiber contents of 3.0% and 6.0%.

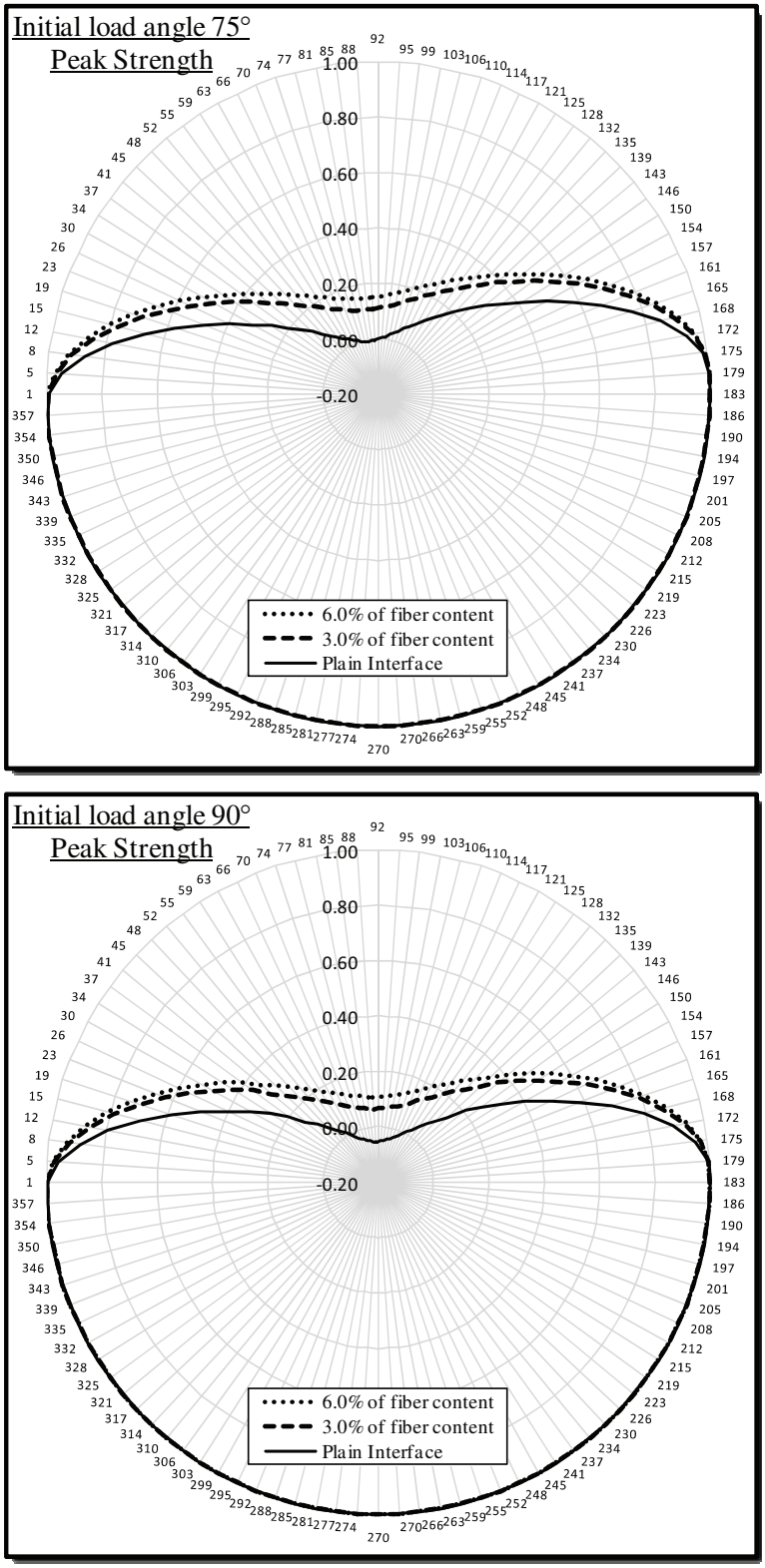

Figure 5.19: Polar plots of post-cracking analysis of TS2 and UT for different concrete types: plain concrete and SFRC with “Dramix type I” fibers having fiber contents of 3.0% and 6.0%.

where the proposed interface model for FRCC mainly behaves in a elastic manner.

- For the different initial load stages ρ, it can be observed that the critical angles ρ_{cr}, at which corresponds the minimum values for the CI parameter, slightly turns toward failure modes I of fracture $\rho_{cr} \longrightarrow \frac{\pi}{2}$ as the fiber concrete increases.
- As final comment, it can be stated that the influence of the fiber effect is relevant in all cases, but it is more pronounced in the mixed fracture modes (acting in both CI values and the critical value of the ρ angle) than for the tensile one where only the value of CI is influenced.

5.3 Closure chapter and concluding remarks

This chapter proposes the numerical application at material (Gauss-point) level of the interface model for simulating the cracking behavior of Fiber-Reinforced Cementitious Composites (FRCCs). The adopted formulation on the interface element for connecting nodes of two adjacent cement matrix elements is one of the key contribution of the present chapter. The proposal, completely detailed in Chapter 3, was obtained by extending an interface model already available for analyzing the behavior of plain concrete members. Thus, the contribution of fibers bridging cracks possibly developing throughout those interfaces is modeled within the zero-thickness elements, along with the bonding behavior of cement matrix.

Finally, applications of the numerical procedure on both notched specimens tested under mixed fracture modes and FRCC samples in tension demonstrate the soundness of the proposed model and its accuracy in simulating the cracking behavior of fiber-reinforced concrete members. The proposed simulations of experimental tests under several complex states for stresses demonstrate the accuracy of the proposed interface model to reproduce the mechanical behavior of FRCCs. In particular, the role of the fiber content in turning the brittle behavior of plain concrete in tensile regime in an increasing ductile response was accurately reproduced by the model, after the calibration of the internal mechanical parameters based on experimental results.

6 Structural scale failure analysis of fiber reinforced concrete based on a discrete crack model

TO BE WRITTEN

7 Cracked hinge numerical for fiber-reinforced concrete

This section figures out a non-linear cracked hinge model developed through an appropriate mechanical approach aimed at simulating the two key crack-bridging mechanisms of steel fibers, as mentioned in the previous chapters, on a notched section of four-point bending tests. Particularly, the results of the experimental activity carried out on Steel Fiber-Reinforced Concrete (SFRC) by mixing short and long hooked-end fibers (completely reported in Chapter 2) were considered for calibrating and validating the proposed numerical tool.

Section 7.1 of this chapter outlines the basic assumptions of the possible lumped-plasticity method, above mentioned, for simulating the observed post-cracking behavior of SFRC specimens presented in Chapter 2. In Section 7.2 the bridging effects induced by fibers crossing the fracture surfaces in terms of bond-slip mechanisms is described. Then, Section 7.3 reports the dowel action resulting in a shear transfer mechanism of steel fibers crossing cracks. Both models were briefly described while the complete description can be founded in Chapter 3 and 4. Comparisons between experimental data and numerical predictions are presented and discussed in Section 7.4. Finally, some conclusions are given in Section 7.5.

7.1 Basic assumptions

The model formulation, outlined in this section, was based on the original idea by Olesen [2001]. Similar proposals for fracture behavior of both plain and SFRC members were proposed in literature a.o. by Zhang and Li [2004], Oh et al. [2007], Walter and Olesen [2008], Park et al. [2010], Buratti et al. [2011].

According to the fictitious crack method [Olesen, 2001], the following stress-strain and stress-crack opening relationships can be founded in the notched section of Fig. 7.1

$$\sigma_{SFRC} = E \cdot \varepsilon \tag{7.1}$$

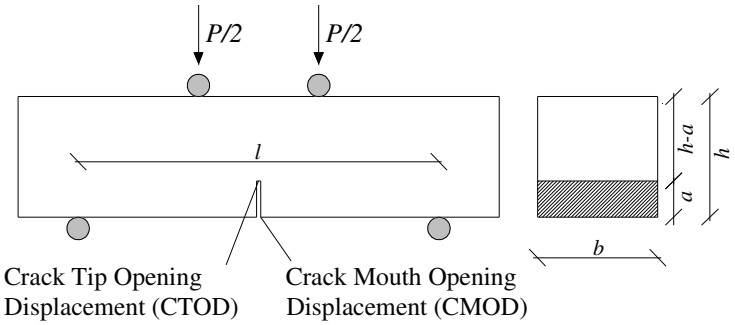

Figure 7.1: Geometrical description of the analyzed four-point bending scheme.

$$\sigma_{SFRC} = \sigma\left[u_{cr}\right] + \sum_{f=0}^{n_f}\left[\sigma_f\left[u_{N,cr}\right] n_{N,f} + \tau_f\left[u_{T,cr}\right] n_{T,f}\right] \tag{7.2}$$

being σ_{SFRC} the stress of the considered cementitious composite in the notched section, E the concrete elastic modulus, ε the elastic strain and $\sigma\left[u_{cr}\right]$ the stress-crack opening law of the plain concrete; σ_f and τ_f mean the bond-slip and dowel actions of the single considered reinforcement which are related to axial and tangential cracking displacements, $u_{N,cr}$ and $u_{T,cr}$ at fiber level, respectively (Fig. 7.2); $n_{N,f}$ and $n_{T,f}$ are the cosine directors of fiber for its normal and tangential direction, respectively. Finally, n_f represents the number of fibers crossing the analyzed strip in the crack section, considering for simplicity that each generic fiber crosses the fracture line at its mid-length, $l_{emb} = l_f/2$.

As a matter of principle Eq. (7.2) is the same one proposed for the interface formulation in Chapter 3 (to see Eq. 3.2) that was also employed in more general finite element models in Chapter 6.

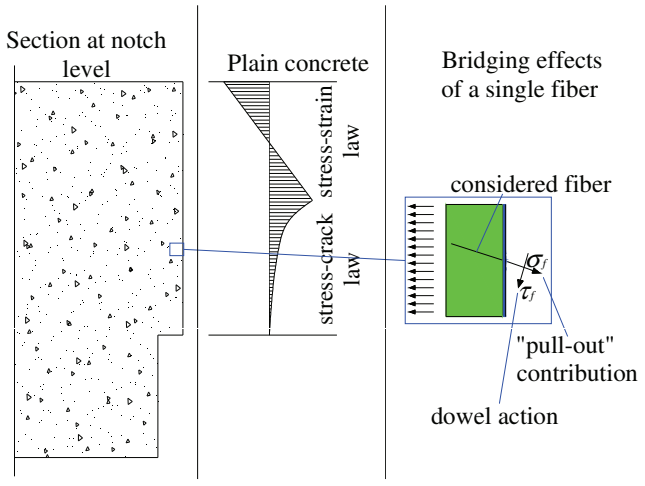

Figure 7.2: Stress distributions and fiber actions during the crack evolution.

The considered cosine directors for each fiber, given in Eq. (7.2), were finally based on

the following relations

$$n_{N,f} = \cos\vartheta\cos\varpi;\ \ n_{T,f} = \sin\vartheta\cos\varpi. \tag{7.3}$$

being ϑ and ϖ the polar and the azimuthal angle of the single fiber crossing the crack surface.

The number of crossing fibers per strip, n_f, was evaluated through the proposal outlined by Dupont and Vandewalle [2005]

$$n_f = \alpha_{\vec{N}} \frac{\rho_f}{A_f} A_i \tag{7.4}$$

where ρ_f is the fiber content, A_f and A_i are the cross-sectional area of a single fiber and the interface area ($A_i = b \cdot h_s$, being b the base width and h_s the height of the analyzed strip), respectively.

The orientation factor can be estimated by means of the following relationship [Dupont and Vandewalle, 2005]

$$\alpha_{\vec{N}} = \frac{\alpha_{\vec{N},1} \cdot (b - l_f)(h - l_f) + \alpha_{\vec{N},2} \cdot \left[(b - l_f) l_f + (h - l_f) l_f\right] + \alpha_{\vec{N},3} \cdot {l_f}^2}{b \cdot h} \tag{7.5}$$

by geometrically averaging the orientation factors $\alpha_{\vec{N},1}$, $\alpha_{\vec{N},2}$ and $\alpha_{\vec{N},3}$, referred to the zone 1, 2 and 3 as outlined in Fig. 7.3.

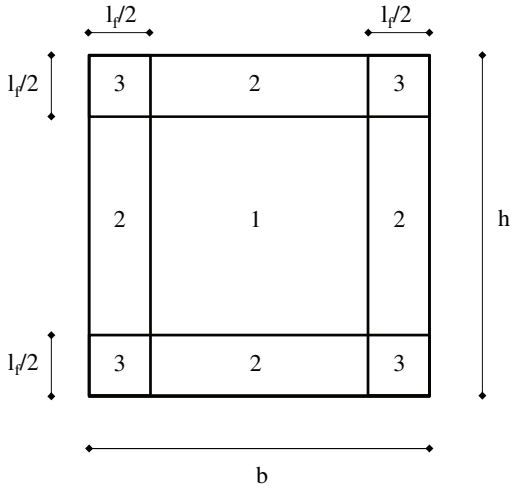

Figure 7.3: The three orientation zones for the concrete beam specimen: $b \times h \times l$ (base × height × length) having $l \geq b$ and $l \geq h$.

The stress-crack opening relationship, $\sigma\,[u_{cr}]$, of plain concrete matrix was based on the fracture-based interface law proposed by Carol et al. [1997] and herein considering

the case of only tension. Particularly, the interface loading criterion, the flow rule and the softening (evolution) law were defined as

$$\begin{aligned} f(\sigma,\kappa) &= \sigma^2 - \sigma_y^2 \leq 0 && \text{loading criterion} \\ \dot{u}_{cr} &= \dot{\lambda}\frac{\partial f}{\partial \sigma} = 2\cdot\dot{\lambda}\cdot\sigma && \text{plastic flow} \\ \sigma_y &= f_t\left(1-\frac{w_{cr}}{G_f^I}\right) && \text{evolution law} \end{aligned} \tag{7.6}$$

where σ_y is the current tensile strength and κ the internal state variable. The incremental cracking separation, $\dot{u}_{cr}$, was defined by means of the classical flow rule, being $\dot{\lambda}$ the non-negative plastic multiplier. The variation in σ_y was assumed to be linear, from its maximum value f_t (tensile strength) to zero, based on the work spent-to-fracture energy ratio, $\frac{w_{cr}}{G_f^I}$. The incremental work spent for fracture, $\dot{w}_{cr}$, was defined as follows

$$\dot{w}_{cr} = \sigma\cdot\dot{u}_{cr}. \tag{7.7}$$

Based on these hypothesis, the employed model exhibits the following closed-form solution under persistent loading conditions [Carol et al., 1997, Stankowski et al., 1993]

$$\sigma = f_t \exp\left(-\frac{u_{cr} f_t}{G_f^I}\right). \tag{7.8}$$

as it can be shown in Fig. 7.4(a). The total crack displacement u_{cr}, at the considered strip, was given as the difference between the total one minus the elastic part

$$u_{cr} = u_{tot} - s\frac{\sigma_{SFRC}[u_{cr}]}{E} \tag{7.9}$$

where

$$u_{tot} = 2\cdot\phi\cdot(y-y_0) \tag{7.10}$$

being ϕ the angular deformation, while y and y_0 deal with the considered strip position and the depth of the neutral axis as depicted in Fig. 7.4(b). In Eq. (7.9), s represents the hinge length.

By solving the Eq. (7.9) for σ_{SFRC} and substituting $u_{tot} = s\cdot\epsilon^*$, where ϵ^* figures out the mean longitudinal strain of the section

$$\varepsilon^* = \frac{2\cdot\phi\cdot(y-y_0)}{s} \tag{7.11}$$

the following expression for σ_{SFRC} can be obtained

$$\sigma_{SFRC} = \frac{E \cdot (2 \cdot \phi \cdot (y - y_0) - u_{cr}[y])}{s} \tag{7.12}$$

Now, by substituting Eqs. (7.2) and (7.8) into Eq. (7.12) the expression of the cracking relative displacement u_{cr}, at the y level of the considered strip, is reached

$$u_{cr}[y] = \frac{G_f^I \cdot W\left[-\frac{f_t^2 \cdot s \cdot \exp\left(-\frac{2 \cdot f_t \cdot \phi \cdot (y-y_0)}{G_f^I} + \frac{s \cdot (\sigma_f + \tau_f)}{E \cdot G_f^I}\right)}{E \cdot G_f^I}\right]}{f_t} + 2 \cdot \phi \cdot (y - y_0) + \frac{s \cdot (\sigma_f + \tau_f)}{E \cdot f_t} \tag{7.13}$$

where $W[...]$ represents the well-known Lambert W function (also known as "omega" function or product logarithm).

Finally, by adopting the above Eq. (7.13) into Eq. (7.8), the following composite stress σ_{SFRC} can be obtained

$$\sigma_{SFRC} = f_t \cdot \exp\left(\begin{array}{l} -\frac{2 \cdot f_t \cdot \phi \cdot (y-y_0)}{G_f^I} + \frac{s \cdot (\sigma_f + \tau_f)}{E \cdot G_f^I} - \\ W\left[-\frac{f_t^2 \cdot s \cdot \exp\left(-\frac{2 \cdot f_t \cdot \phi \cdot (y-y_0)}{G_f^I} + \frac{s \cdot (\sigma_f + \tau_f)}{E \cdot G_f^I}\right)}{E \cdot G_f^I}\right] \end{array}\right) + (\sigma_f + \tau_f) \tag{7.14}$$

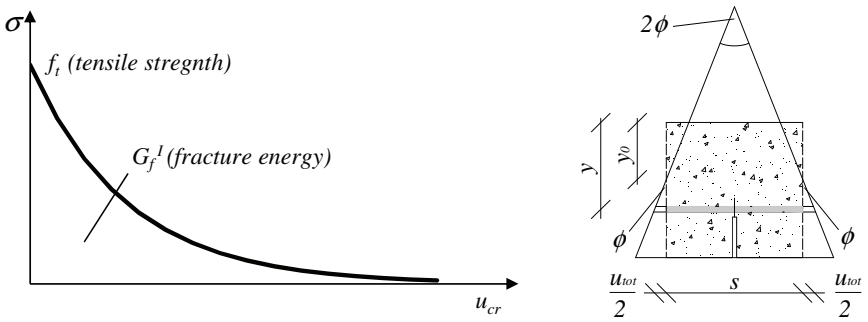

(a) (b)

Figure 7.4: Cracked hinge: (a) stress-crack opening displacement of plain concrete and (b) main geometrical assumption under deformation.

Knowing the complete stress distributions in both elastic and post-cracking state the external force P and/or the subsequent bending moment M can be easily obtaining by equilibrium conditions between internal and external forces. Particularly the axial equilibrium was commonly employed for obtaining the position of the neutral axis y_0.

Once this latter was achieved the bending equilibrium can be employed for calculating the resultant moment.

Then, both Crack-Tip and Mouth Opening Displacements (CTOD and CMOD as shown on Fig. 7.1) can be easily calculated by evaluating u_{tot} of Eq. (7.10) for $y = h - a$ and $y = h$, respectively, as follows

$$\begin{aligned} CTOD &= u_{tot}[h-a] \\ CMOD &= u_{tot}[h]. \end{aligned} \tag{7.15}$$

7.2 Bond-slip bridging of fibers on concrete cracks

Fracture opening processes in concrete activate bridging effects induced by fibers. The axial (tensile) stresses in fibers are balanced by bond developing on their lateral surface embedded in concrete matrix. Thus, a simple equilibrium equation can be written

$$\frac{d\sigma_f[x]}{dx} = -\frac{4\tau_a[x]}{d_f} \tag{7.16}$$

where σ_f is the fiber axial tensile stress accounted in the composite model of Eq. (7.2), τ_a the local bond stress between fiber and surrounding concrete, and d_f the fiber diameter. This approach is strictly true in case of considering synthetic fibers, while can be accepted for steel ones when the length l_{emb} results in the condition that $|\sigma_{f,max}| \leq \sigma_{y,s}$, where $\sigma_{f,max}$ and $\sigma_{y,s}$ represent the maximum axial stress and the steel yielding, respectively.

A simplified bilinear shear-slip law was proposed to model the fiber-to-concrete debonding process as follows

$$\tau_a[x] = \begin{cases} -k_E s[x] & s[x] \leq s_e \\ -\tau_{y,a} + k_S (s[x] - s_e) & s_e < s[x] \leq s_u \\ 0 & s[x] > s_u \end{cases} \tag{7.17}$$

where $s[x]$ defines the debonded displacement between the fiber and concrete (at the point of the abscissa x). The positive constants k_E and k_S represent the elastic and softening slopes of such bond-slip relationships, respectively; $\tau_{y,a}$ is the shear bond strength, while s_e and s_u are the elastic and ultimate slips, respectively.

The complete derivation of this numerical model, and its validation against bond-slip experimental tests, were proposed in a previous work published by the authors, see Caggiano et al. [2012c], Caggiano and Martinelli [2012] and completely reported in Chapter 4.

7.3 Dowel action of fibers crossing the concrete cracks

The dowel mechanism, resulting in a shear transfer action across cracks, represents an important component on the overall interaction between steel fibers and concrete matrix. A simple analytical model was developed for this purpose.

The well-known Winkler beam theory was used to describe the relationship of the dowel force, V_d, and the transversal displacement, Δ. Its analytical solution was defined as

$$V_d = E_s J_s \lambda_f^3 \Delta \tag{7.18}$$

where E_s is the steel elastic modulus and J_s the fiber moment of inertia. The Winkler parameter, λ_f, is analytically derived as

$$\lambda_f = \sqrt[4]{\frac{k_c d_f}{4 E_s J_s}} = \sqrt[4]{\frac{16 k_c}{E_s \pi d_f^3}} \tag{7.19}$$

where k_c is the foundation stiffness (herein, the surrounding mortar).

The following expression proposed by Soroushian et al. [1987] was employed for the evaluation of k_c,

$$k_c = \frac{127 c_1 f_c^{(1/2)}}{d_f^{(2/3)}} \tag{7.20}$$

where c_1 mainly defines the amount of the elastic foundation stiffness of the surrounding concrete.

Finally, the empirical expression proposed by Dulacska [1972] for RC-structures was taken as the maximum dowel strength

$$V_{d,u} = k_{dow} d_f^2 \sqrt{|f_c||\sigma_{y,s}|} \tag{7.21}$$

being k_{dow} a non-dimensional coefficient whose typical value 1.27 could be assumed as reference for RC-members [El-Ariss, 2007], d_f is the diameter of the fiber, while f_c and $\sigma_{y,s}$ are the strengths of concrete and the steel, respectively.

7.4 Numerical predictions

The composite model outlined in the three above sections were introduced in the cracked hinge zone with the aim to simulate the $150 \times 150 \times 600\ mm^3$ notched concrete specimens, tested under four-point bending presented in Chapter 2.

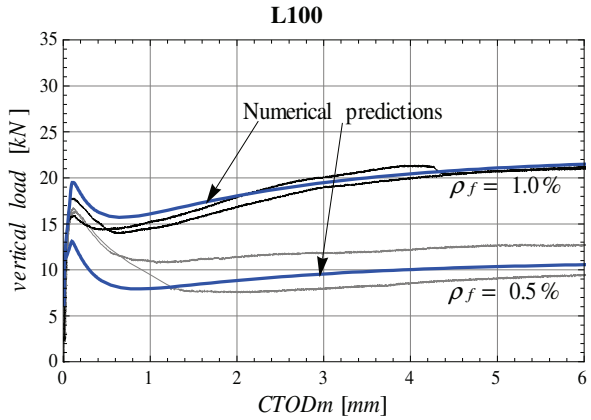

Figure 7.5: Load-$CTODm$ numerical predictions against the experimental data on SFRC L100-type by Caggiano et al. [2012a].

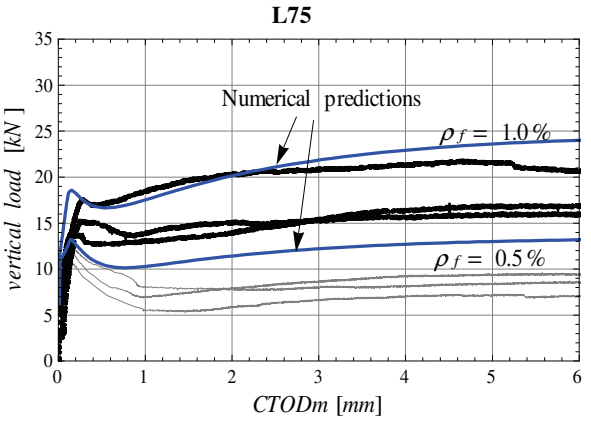

Figure 7.6: Load-$CTODm$ numerical predictions against the experimental data on SFRC L75-type by Caggiano et al. [2012a].

For the purpose of the numerical evaluations, three material types were considered: (1) plain concrete, (2) steel fiber-reinforced concrete having $\rho_f = 0.5\%$ and, (3) the same as (2) but considering $\rho_f = 1.0\%$. The geometry and material properties were chosen according to the tests outlined in experimental campaign given in Chapter 2.

The local bond-slip law was determined through an inverse identification on the test results obtained on specimens reinforced with only short fibers with $\rho_f = 1.0\%$. Then, such a calibration was used to simulate the behavior observed in all other tests. The mechanical parameters calibrated and employed in the numerical evaluations were: $f_t = 2.08$ MPa (tensile strength), $E = 31.5$ GPa (elastic modulus), $s = 75$ mm (hinge length), $G_f^I = 0.5$ N/mm (fracture energy), $\tau_{y,a} = 4.5$ MPa (shear bond strength), $k_E = 100.0\,N/mm^3$ (elastic stiffness), $k_S = 0.1\,N/mm^3$ (softening stiffness), $k_{dow} = 2.8$ (dowel parameter) and $c_1 = 0.15$ (coefficient of beam foundation). The assumed values for the orientation factors $\alpha_{\vec{N}}$ were based on the theoretical proposal given by Dupont

and Vandewalle [2005] and briefly reported in Section 7.1. Particularly, the values 0.57 and 0.54 were determined for long and short fibers, respectively.

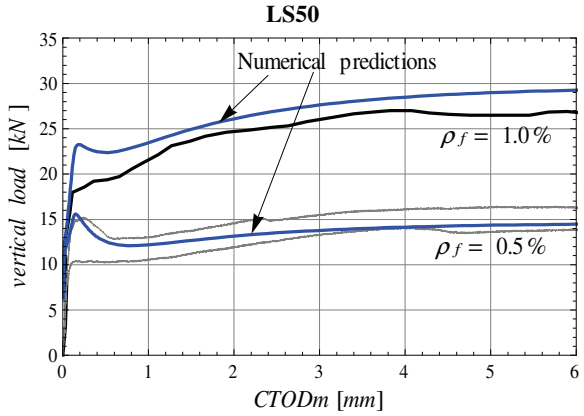

Figure 7.7: Load-$CTODm$ numerical predictions against the experimental data on SFRC LS50-type by Caggiano et al. [2012a].

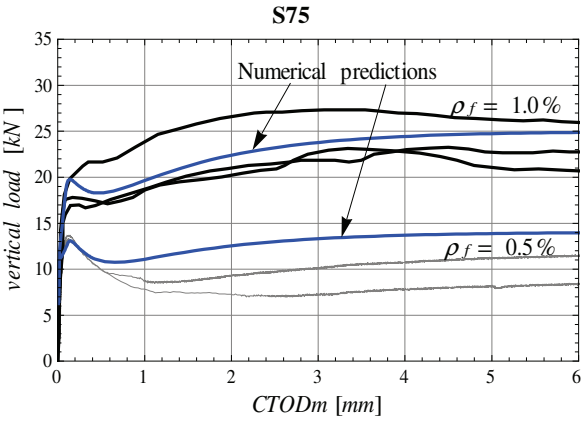

Figure 7.8: Load-$CTODm$ numerical predictions against the experimental data on SFRC S75-type by Caggiano et al. [2012a].

The numerical force-$CTODm$ curves, against the corresponding experimental results, are proposed from Fig. 7.5 to 7.9. $CTODm$ represents the mean of the two opposite Crack Tip Opening Displacements ($CTODs$) registered by the transductor devices of the experimental campaign (to see Chapter 2). The load-crack opening responses of SFRC beams emphasize the significant influence of the fiber reinforcement on the peak strength and the post-peak behavior. Fiber bridging effects on the pre-cracked concretes were well simulated by the considered numerical approach with the proposed non-linear separation law for SFRC.

The results of these numerical analyses demonstrate that the model reproduces very accurately the performance of SFRCs in terms of both peak strength and post-peak ductility of failure processes under mode I type of fracture when different fiber types

and contents were considered.

7.5 Closure chapter and final remarks

The four-point bending behavior of notched SFRC beams was numerically investigated and compared against experimental results on four-point bending tests. Two different amounts of steel fibers were considered and modeled at a numerical stand point. A novel stress-crack opening model, based on a hinge-crack approach already available in the scientific literature, were employed to reproduce and simulate the experimental results proposed in an other chapter of this thesis. As for the interface formulation, originally employed for meso-mechanical analyses as proposed in Chapter 6, the model was founded on the explicit modeling of the interaction between concrete and steel fibers. The model predictions, compared with the experimental measures, demonstrate the soundness and capability of the model with the aim to reproduce the mechanical response of SFRC beam frames in terms of force-$CTOD$ curves.

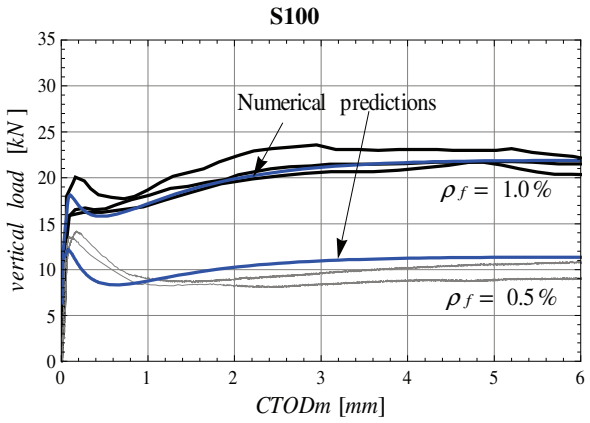

Figure 7.9: Load-$CTODm$ numerical predictions against the experimental data on SFRC S100-type by Caggiano et al. [2012a].

8 Final remarks and conclusions

TO BE WRITTEN

Bibliography

ACI-318-08/318R-08. *ACI Committee 318, Building code and commentary.* American Concrete Institute, ACI Farmington Hills, 2008.

ACI-544.2R-89. *Measurement of properties of fibre reinforced concrete. ACI Manual of Concrete Practice; Part 5: Masonry, Precast Concrete and Special Processes, American Concrete Institute.* 1996.

ACI-544.4R-88. *Design considerations for steel Fiber Reinforced Concrete.* American Concrete Institute, ACI Farmington Hills, 1996.

AFGC-SETRA. *Ultra High Performance Fibre-Reinforced Concretes, Interim recommendations.* AFGC Publication, France, 2002.

B. Akcay and M. Tasdemir. Mechanical behaviour and fibre dispersion of hybrid steel fibre reinforced self-compacting concrete. *Construction and Building Materials*, 28 (1):287 – 293, 2012.

J. Alwan, A. Naaman, and W. Hansen. Pull-out work of steel fibers from cementitious composites: Analytical investigation. *Cement and Concrete Composites*, 13(4):247–255, 1991.

F. Armero and C. Linder. Numerical simulation of dynamic fracture using finite elements with embedded discontinuities. *Int. J. of Fracture*, 160:119–141, 2009.

ASTM-C-1018. *Standard Test Method for Flexural Toughness and First-Crack Strength of Fiber-Reinforced Concrete (Using Beam With Third-Point Loading).* American Society for Testing and Materials, 1998.

B. Banholzer, W. Brameshuber, and W. Jung. Analytical evaluation of pull-out tests- The inverse problem. *Cement and Concrete Composites*, 28:564–571, 2006.

N. Banthia and N. Nandakumar. Crack growth resistance of hybrid fiber reinforced cement composites. *Cement and Concrete Composites*, 25(1):3 – 9, 2003.

N. Banthia and M. Sappakittipakorn. Toughness enhancement in steel fiber reinforced concrete through fiber hybridization. *Cement and Concrete Research*, 37(9):1366 – 1372, 2007.

N. Banthia and J. Trottier. Test methods for flexural toughness characterization of fiber reinforced concrete: Some concerns and a proposition. *ACI - Materials J.*, 92(1):48 – 57, 1995.

J. Barros and J. Figueiras. Flexural behavior of SFRC: Testing and Modeling. *ASCE - J. of Materials in Civil Engrg.*, 11(4):331–339, 1999.

J. Barros, V. Cunha, A. Ribeiro, and J. Antunes. Post-cracking behaviour of steel fibre reinforced concrete. *Material Structures*, 38(1):47 – 56, 2005.

Z. Bazant and B. Oh. Crack band theory for fracture of concrete. *RILEM - Muterial Structures*, 93:155–177, 1983.

Z. Bazant, M. Tabbara, M. Kazemi, and G. Pijaudier-Cabot. Random particle model for fracture of aggregate or fiber composites. *J. of Engrg. Mech., ASCE*, 116:1686–1705, 1990.

A. Beghini, Z. Bazant, Y. Zhou, O. Gouirand, and F. Caner. Microplane model M5f for multiaxial behavior and fracture of fiber-reinforced concrete. *ASCE - J. of Materials in Civil Engrg.*, 133(1):66–75, 2007.

T. Belytschko, Y. Lu, and L. Gu. Crack propagation by element-free Galerkin methods. *Engrg. Fracture Mechanics*, 51(2):295 – 315, 1995.

T. Belytschko, D. Organ, and C. Gerlach. Element-free galerkin methods for dynamic fracture in concrete. *Computer Methods in Applied Mechanics and Engineering*, 187 (3-4):385 – 399, 2000.

S. Billington. Alterate approaches to simulating the performance of ductile fiber-reinforced cement-based materials in structural applications. In N. Bicanic, R. de Borst, H. Mang, and G. Meschke, editors, *Computational Modelling of Concrete Structures, Rohrmoos/Schladming, Austria*, pages 15–29, 2010.

S. Bishnoi and K. L. Scrivener. μic: A new platform for modelling the hydration of cements. *Cement and Concrete Research*, 39(4):266 – 274, 2009.

A. Blanco, P. Pujadas, A. de la Fuente, S. Cavalaro, and A. Aguado. Application of constitutive models in european codes to rc–frc. *Construction and Building Materials*, 40(0):246 – 259, 2013.

J. Bolander and S. Saito. Discrete modeling of short-fiber reinforcement in cementitious composites. *Advanced Cement Based Materials*, 6(3-4):76–86, 1997.

A. M. Brandt. Fibre reinforced cement-based (FRC) composites after over 40 years of development in building and civil engineering. *Composite Structures*, 86(1-3):3 – 9, 2008.

N. Buratti, C. Mazzotti, and M. Savoia. Post-cracking behaviour of steel and macro-synthetic fibre-reinforced concretes. *Construction and Building Materials*, 25(5): 2713 – 2722, 2011.

M. Butler, V. Mechtcherine, and S. Hempel. Experimental investigations on the durability of fibre-matrix interfaces in textile-reinforced concrete. *Cement and Concrete Composites*, 31:221–231, 2009.

A. Caballero, K. Willam, and I. Carol. Consistent tangent formulation for 3D interface modeling of cracking/fracture in quasi-brittle materials. *Computer Methods in Applied Mechanics and Engrg.*, 197:2804–2822, 2008.

A. Caggiano and E. Martinelli. A unified formulation for simulating the bond behaviour of fibres in cementitious materials. *Materials & Design*, 42(0):204 – 213, 2012.

A. Caggiano, G. Etse, and E. Martinelli. Interface model for fracture behaviour of fiber-reinforced cementitious composites (FRCCs): Theoretical formulation and applications. *Europ. journal of environmental and civil engineering*, 15(9):1339–1359, 2011.

A. Caggiano, M. Cremona, C. Faella, C. Lima, and E. Martinelli. Fracture behavior of concrete beams reinforced with mixed long/short steel fibers. *Construction and Building Materials*, 37(0):832 – 840, 2012a.

A. Caggiano, G. Etse, and E. Martinelli. Zero-thickness interface model formulation for failure behavior of fiber-reinforced cementitious composites. *Computers & Structures*, 98-99(0):23 – 32, 2012b.

A. Caggiano, E. Martinelli, and C. Faella. A fully-analytical approach for modelling the response of FRP plates bonded to a brittle substrate. *Int. J. of Solids and Structures*, 49(17):2291 – 2300, 2012c.

G. Camps, A. Turatsinze, A. Sellier, G. Escadeillas, and X. Bourbon. Steel-fibre-reinforcement and hydration coupled effects on concrete tensile behaviour. *Engineering Fracture Mechanics*, 75(18):5207 – 5216, 2008.

I. Carol, P. Prat, and C. Lopez. Normal/shear cracking model: Applications to discrete crack analysis. *J. of Engrg. Mechanics - ASCE*, 123:765–773, 1997.

A. Carosio, K. Willam, and G. Etse. On the consistency of viscoplastic formulations. *Int. J. of Solids and Structures*, 37(48-50):7349 – 7369, 2000.

A. Carpinteri and R. Brighenti. Fracture behaviour of plain and fiber-reinforced concrete with different water content under mixed mode loading. *Materials & Design*, 31(4): 2032 – 2042, 2010.

A. Carpinteri, B. Chiaia, and K. M. Nemati. Complex fracture energy dissipation in concrete under different loading conditions. *Mechanics of Materials*, 26(2):93 – 108, 1997.

CEB-FIP-90. *CEB, CEB-FIP Model Code 1990*. Bulletin d'information, Thomas Telford, London, pp. 203-205, 1993.

B. Chen and J. Liu. Residual strength of hybrid-fiber-reinforced high-strength concrete after exposure to high temperatures. *Cement and Concrete Research*, 34(6):1065 – 1069, 2004.

CNR-DT-204. *Guidelines for design, construction and production control of fiber reinforced concrete structures*. National Research Council of Italy, 2006.

C. Comi and U. Perego. Fracture energy based bi-dissipative damage model for concrete. *Int. J. of Solids and Structures*, 38(36-37):6427 – 6454, 2001.

P. Cundall. *A computer model for simulating progressive large scale movements in blocky rock systems*. Proc. Int. Symp. Rock Fracture, ISRM, Nancy, France, 2-8, 1971.

V. Cunha, J. Barros, and J. Sena-Cruz. Pullout behavior of steel fibers in self-compacting concrete. *J. of Engrg. Mechanics - ASCE*, 22(1):1–9, 2010.

V. M. Cunha, J. A. Barros, and J. M. Sena-Cruz. A finite element model with discrete embedded elements for fibre reinforced composites. *Computers & Structures*, 94–95 (0):22 – 33, 2012.

CUR. *Bepaling van de Buigtrekterk de Buigtaaiheid en de Equivalente Buigtreksterkte van Staalvezelbeton*. Civieltechnisch Centrum Uitvoering Research en Regelgeving, The Netherlands, 12 pp., 1994.

DAfStB. *Richtlinie "Stahlfaserbeton" (Directive for SFRC)*. Deutscher Ausschuss fur Stahlbeton, Germany - (In German), 2010.

E. Dawood and M. Ramli. Development of high strength flowable mortar with hybrid fiber. *Construction and Building Materials*, 24(6):1043 – 1050, 2010.

E. Dawood and M. Ramli. High strength characteristics of cement mortar reinforced with hybrid fibres. *Construction and Building Materials*, 25(5):2240 – 2247, 2011.

E. Dawood and M. Ramli. Mechanical properties of high strength flowing concrete with hybrid fibers. *Construction and Building Materials*, 28(1):193 – 200, 2012.

DBV. *Merkblatt "Stahlfaserbeton" (SFRC leaflet)*. Deutscher Beton- und Bautechnik-Verein E.V., Germany - (In German), 2001.

R. De Borst and M. Guitierrez. A unified framework for concrete damage and fracture models including size effects. *Int. J. of Fracture*, 95:261–277, 1999.

R. de Borst, J. Pamin, R. Peerlings, and L. Sluys. On gradient-enhanced damage and plasticity models for failure in quasi-brittle and frictional materials. *Comp. Mech.*, 17:130–141, 1995.

S. Dei Poli, M. Di Prisco, and P. Gambarova. Shear response, deformations, and subgrade stiffness of a dowel bar embedded in concrete. *ACI Structural J.*, 89(6):665–675, 1992.

M. di Prisco, G. Plizzari, and L. Vandewalle. Fibre reinforced concrete: new design perspectives. *Material Structures*, 42(9):1261 – 1281, 2009.

DIN-1048. *Prüfverfahren für Beton; Teil 1: Frischbeton*. Festbeton in Bauwerken und Bauteilen, 1991.

Y. Ding, Y. Zhang, and A. Thomas. The investigation on strength and flexural toughness of fibre cocktail reinforced self-compacting high performance concrete. *Construction and Building Materials*, 23(1):448 – 452, 2009.

Y. Ding, Z. You, and S. Jalali. Hybrid fiber influence on strength and toughness of RC beams. *Composite Structures*, 92(9):2083 – 2089, 2010.

Y. Ding, C. Azevedo, J. Aguiar, and S. Jalali. Study on residual behaviour and flexural toughness of fibre cocktail reinforced self compacting high performance concrete after exposure to high temperature. *Construction and Building Materials*, 26(1):21 – 31, 2012.

J. S. Dolado and K. van Breugel. Recent advances in modeling for cementitious materials. *Cement and Concrete Research*, 41(7):711 – 726, 2011.

K. Duan, X. Hu, and F. H. Wittmann. Size effect on specific fracture energy of concrete. *Engrg. Fracture Mechanics*, 74(1-2):87 – 96, 2007.

H. Dulacska. Dowel action of reinforcement crossing cracks in concrete. *ACI Structural J.*, 69(12):754–757, 1972.

D. Dupont and L. Vandewalle. Distribution of steel fibres in rectangular sections. *Cement and Concrete Composites*, 27(3):391 – 398, 2005.

E. Dvorkin, A. Cuitino, and G. Gioia. Finite elements with displacement embedded localization lines insensitive to mesh size and distortions. *Int. J. for Numerical Methods in Engrg.*, 30:541–564, 1990.

EHE08. *Comisión Permanente del Hormigón (Ministerio de Fomento), Instrucción del Hormigón Estructural*. Spanish Code - In Spanish, 2008.

B. El-Ariss. Behavior of beams with dowel action. *Engrg. Structures*, 29(6):899 – 903, 2007.

A. S. El-Dieb. Mechanical, durability and microstructural characteristics of ultra-high-strength self-compacting concrete incorporating steel fibers. *Materials & Design*, 30 (10):4286 – 4292, 2009.

EN-12390-3. *Testing of hardened concrete. Part 3: compressive strength of test specimens.* BSI, 2009.

EN-14651. *Test method for metallic fibrered concrete - Measuring the flexural tensile strength (limit of proportionality (LOP), residual).* NS-EN 14651:2005, 2005.

G. Etse and K. Willam. A fracture energy-based constitutive formulation for inelastic behavior of plain concrete. *ASCE-JEM*, 120:1983–2011, 1994.

G. Etse, A. Caggiano, and S. Vrech. *Constitutive microplane and interface laws for multiscale analysis of steel fiber concrete.* ECCOMAS 2012 - European Congress on Computational Methods in Applied Sciences and Engineering, e-Book Full Papers, pp. 7459-7477.

G. Etse, M. Nieto, and P. Steinmann. A micropolar microplane theory. *Int. J. of Engrg. Science*, 41(13–14):1631 – 1648, 2003.

G. Etse, A. Caggiano, and S. Vrech. Multiscale failure analysis of fiber reinforced concrete based on a discrete crack model. *Int J of Fracture*, pages 1–16, 2012. ISSN 0376-9429. URL http://dx.doi.org/10.1007/s10704-012-9733-z.

Eurocode-2. *Design of concrete structures.* EN 1992-1-1, 2004.

A. Ezeldin and P. Balaguru. Normal- and high-strength fiber-reinforced concrete under compression. *ASCE - J. of Materials in Civil Engrg.*, 4(4):415–429, 1992.

A. Fantilli and P. Vallini. A cohesive interface model for the pollout of inclined steel fibers in cementitious matrixes. *J. of Advanced Concrete Technology*, 5(2):247–258, 2007.

A. P. Fantilli, P. Vallini, and B. Chiaia. Ductility of fiber-reinforced self-consolidating concrete under multi-axial compression. *Cement and Concrete Composites*, 33(4): 520 – 527, 2011.

Faserbeton-R. *Osterreichische Vereinigung fur Beton-und Bautechnik.* OBBV, Wien, 2002.

L. Ferrara and A. Meda. Relationships between fibre distribution, workability and the mechanical properties of SFRC applied to precast roof elements. *Materials and Structures*, 39:411–420, 2006.

G. Ferro, A. Carpinteri, and G. Ventura. Minimum reinforcement in concrete structures and material/structural instability. *Int. J. of Fracture*, 146:213–231, 2007.

fib Model-Code. *Model Code 2010 - First complete draft, Vol. 1*. Comité Euro-International du Beton-Federation International de la Precontrainte, Paris, 2010a.

fib Model-Code. *Model Code 2010 - First complete draft, Vol. 2*. Comité Euro-International du Beton-Federation International de la Precontrainte, Paris, 2010b.

P. Folino. *Computational Analysis of Failure Behavior of Arbitrary Strength Concretes*. PhD thesis, Universidad de Buenos Aires, LMNI-FI-UBA, 2012.

P. Folino and G. Etse. Performance dependent model for normal and high strength concretes. *Int. J. of Solids and Structures*, 49(5):701 – 719, 2012.

P. Folino, G. Etse, and A. Will. A performance dependent failure criterion for normal and high strength concretes. *ASCE J. of Engrg. Mechanics*, 135(12):1393 – 1409, 2009.

E. Gal and R. Kryvoruk. Meso-scale analysis of FRC using a two-step homogenization approach. *Computers & Structures*, 89(11-12):921 – 929, 2011.

A. Gens, I. Carol, and E. Alonso. An interface element formulation for the analysis of soil-reinforcement interaction. *Computers and Geotechnics*, 7(1-2):133–151, 1988.

R. Gettu. *Fibre Reinforced Concrete: design and applications*. BEFIB 2008, Bagneux, France, RILEM Publications S.A.R.L., PRO60, 2008.

R. Gettu, D. Gardner, H. Saldivar, and B. Barragan. Study of the distribution and orientation of fibers in SFRC specimens. *Materials and Structures*, 38:31–37, 2005.

A. Ghavami, A. Abedian, and M. Mondali. Finite difference solution of steady state creep deformations in a short fiber composite in presence of fiber/matrix debonding. *Materials & Design*, 31(5):2616 – 2624, 2010.

V. Gopalaratnam, S. Shah, G. Batson, M. Criswell, V. Ramakishnan, and M. Wecharatana. Fracture toughness of fiber reinforced concrete. *ACI - Materials J.*, 88(4):339 – 353, 1991.

V. S. Gopalaratnam and R. Gettu. On the characterization of flexural toughness in fiber reinforced concretes. *Cement and Concrete Composites*, 17(3):239 – 254, 1995.

T. Guttema. *Ein Beitrag zur realitatsnahen Modellierung und Analyse von stahlfaserverstarkten Stahlbeton- und Stahlbetonflachentragwerken*. PhD thesis, Universitat Kassel, 2003.

M. Hassanzadeh. Determination of fracture zone properties in mixed mode I and II. *Engrg. Fracture Mechanics*, 35(4-5):845–853, 1990.

T. Hettich, A. Hund, and E. Ramm. Modeling of failure in composites by X-FEM and level sets within a multiscale framework. *Computer Methods in Applied Mechanics and Engrg.*, 197(5):414–424, 2008.

A. Hillerborg, M. Modeer, and P. Petersson. Analysis of crack formation and crack growth in concrete by means of fracture mechanics and finite elements. *Cement and Concrete Composites*, 6(6):773–781, 1976.

M. Hsie, C. Tu, and P. Song. Mechanical properties of polypropylene hybrid fiber-reinforced concrete. *Materials Science and Engrg.: A*, 494(1–2):153 – 157, 2008.

X. Hu, R. Day, and P. Dux. Biaxial failure model for fiber reinforced concrete. *ASCE - J. of Materials in Civil Engrg.*, 15(6):609–615, 2003.

A. Hund and E. Ramm. Locality constraints within multiscale model for non-linear material behaviour. *Int. J. for Numerical Methods in Engrg.*, 70(13):1613–1632, 2006.

A. Idiart. *Coupled analysis of degradation processes in concrete specimens at the meso-level*. PhD thesis, Universitat Politecnica de Catalunya, ETSECCCP-UPC, 2009.

M. Jirasek and Z. P. Bazant. Macroscopic fracture characteristics of random particle systems. *Int. J. of Fracture*, 69:201–228, 1994.

JSCE-SF4. *Method of tests for flexural strength and flexural toughness of steel fibre reinforced concrete. Concrete Library of previous Japan Society of Civil Engineers (JSCE), Tokyo, 3, pp. 58-61*. 1984.

P. Kabele. Equivalent continuum model of multiple cracking. *Engineering Mechanics*, 9 (1-2):75–90, 2002.

L. Kaczmarczyk and C. J. Pearce. A corotational hybrid-trefftz stress formulation for modelling cohesive cracks. *Computer Methods in Applied Mechanics and Engrg.*, 198 (15-16):1298 – 1310, 2009.

H. Kang and K. Willam. Localization characteristics of triaxial concrete model. *J. of Engrg. Mechanics - ASCE*, 125(8):941–950, 1999.

A. Katz and V. Li. Inclination angle effect of carbon fibers in cementitious composites. *J. of Engrg. Mechanics - ASCE*, 121(12):1340–1348, 1995.

T. Kawai. Some considerations on the finite element method. *Int. J. Numer. Meth. Engrg.*, 16:81 – 120, 1980.

A. Khaloo and N. Kim. Influence of concrete and fiber characteristics on behavior of steel fiber reinforced concrete under direct shear. *ACI Materials J.*, 94(6):592–601, 1997.

D. Kim, A. Naaman, and S. El-Tawi. Comparative flexural behavior of four fiber reinforced cementitious composites. *Cement & Concrete Composites*, 30:917 – 928, 2008.

D. Kim, S. Park, G. Ryu, and K. Koh. Comparative flexural behavior of hybrid ultra high performance fiber reinforced concrete with different macro fibers. *Construction and Building Materials*, 25(11):4144 – 4155, 2011.

S.-M. Kim and R. K. A. Al-Rub. Meso-scale computational modeling of the plastic-damage response of cementitious composites. *Cement and Concrete Research*, 41(3): 339 – 358, 2011.

R. Klein. *Concrete and abstract Voronoi diagrams*. Lecture Notes in Computer Science, Springer-Verlag, Berlin, 1989.

A. Kooiman. *Modelling steel fibre reinforced concrete for structural design*. Doctoral Thesis at the Technical University of Delft (The Netherlands), 2000.

H. Krenchel. *Fiber spacing and specific fiber surface*. In: Neville A, editor. Fibre reinforced cement and concrete. UK: The Construction Press; p. 69–79, 1975.

F. Laranjeira, C. Molins, and A. Aguado. Predicting the pullout response of inclined hooked steel fibers. *Cement and Concrete Research*, 40(10):1471 – 1487, 2010.

F. Laranjeira, A. Aguado, C. Molins, S. Grunewald, J. Walraven, and S. Cavalaro. Framework to predict the orientation of fibers in FRC: A novel philosophy. *Cement and Concrete Research*, 42(6):752 – 768, 2012.

J. Lee and G. Fenves. Plastic-damage model for cyclic loading of concrete structures. *ASCE - JEM*, 124(8):892 – 901, 1998.

M. Lee and B. Barr. A four-exponential model to describe the behaviour of fibre reinforced concrete. *Materials and Structures*, 37(7):464–471, 2003.

C. Leung and P. Geng. Micromechanical modeling of softening behavior in steel fiber reinforced cementitious composites. *Int. J. of Solids and Structures*, 35(31-32):4205–4222, 1998.

F. Li and Z. Li. Continuum damage mechanics based modeling of fiber reinforced concrete in tension. *Int. J. of Solids and Structures*, 38(5):777–793, 2001.

V. Li and Y. Chan. Determination of interfacial debond mode for fiber-reinforced cementitious composites. *J. of Engrg. Mechanics - ASCE*, 120(4):707–719, 1994.

V. Li, Y. Wang, and S. Backer. A micromechanical model of tension-softening and bridging toughening of short random fiber reinforced brittle matrix composites. *J Mech Phys Solids*, 39(5):607 – 625, 1991.

Z. Li, F. Li, T. Chang, and Y. Mai. Uniaxial tensile behavior of concrete reinforced with randomly distributed short fibers. *ACI Materials J.*, 95(5):564–574, 1998.

N. Libre, M. Shekarchi, M. Mahoutian, and P. Soroushian. Mechanical properties of hybrid fiber reinforced lightweight aggregate concrete made with natural pumice. *Construction and Building Materials*, 25(5):2458 – 2464, 2011.

G. Lilliu and J. van Mier. 3D lattice type fracture model for concrete. *Engrg. Fracture Mechanics*, 70:927–941, 2003.

T. Lim, P. Paramasivam, and S. Lee. An analytical model for tensile behaviour of steel fiber concrete. *ACI Materials J.*, 84(4):286–298, 1987.

C. Liu, M. Lovato, M. Stout, and Y. Huang. Measurement of the fracture toughness of a fiber-reinforced composite using the Brazilian disk geometry. *Int. J. of Fracture*, 87: 241–263, 1997.

Z. Liu, T. Menouillard, and T. Belytschko. An XFEM/Spectral element method for dynamic crack propagation. *Int. J. of Fracture*, 169:183–198, 2011.

C. Lopez. *Microstructural analysis of concrete fracture using interface elements. Application to various con-cretes (In Spanish)*. PhD thesis, Universitat Politecnica de Catalunya, ETSECCCP-UPC, 1999.

C. M. Lopez, I. Carol, and A. Aguado. Meso-structural study of concrete fracture using interface elements. I: numerical model and tensile behavior. *Materials and Structures*, 41(3):583–599, 2008a.

C. M. Lopez, I. Carol, and A. Aguado. Meso-structural study of concrete fracture using interface elements. II: compression, biaxial and brazilian test. *Materials and Structures*, 41(3):601–620, 2008b.

R. Lorefice, G. Etse, and I. Carol. Viscoplastic approach for rate-dependent failure analysis of concrete joints and interfaces. *Int. J. of Solids and Structures*, 45(9): 2686–2705, 2008.

H. Manzano, J. Dolado, and A. Ayuela. *Prediction of the mechanical properties of the major constituent phases of cementitious systems by atomistic simulations*. RILEM Proceedings PRO 58: 47–55, 2008.

H. Manzano, J. Dolado, and A. Ayuela. Elastic properties of the main species present in portland cement pastes. *Acta Materialia*, 57(5):1666 – 1674, 2009a.

H. Manzano, J. S. Dolado, and A. Ayuela. Structural, mechanical, and reactivity properties of tricalcium aluminate using first-principles calculations. *Journal of the American Ceramic Society*, 92(4):897 – 902, 2009b.

O. Manzoli, J. Oliver, G. Diaz, and A. Huespe. Three-dimensional analysis of reinforced concrete members via embedded discontinuity finite elements. 1(1):58–83, 2008.

V. Mechtcherine. Towards a durability framework for structural elements and structures made of or strengthened with high-performance fibre-reinforced composites. *Construction and Building Materials*, 31(0):94 – 104, 2012.

G. Meschke and P. Dumstorff. Energy-based modeling of cohesive and cohesionless cracks via X-FEM. *Computer Methods in Applied Mechanics and Engrg.*, 196(21-24): 2338 – 2357, 2007.

F. Minelli and F. Vecchio. Compression field modeling of fiber-reinforced concrete members under shear loading. *ACI Structural J.*, 106(2):244–252, 2006.

D. J. Moes, N. and T. Belytschko. A finite element method for crack growth without remeshing. *Int. J. for Numerical Methods in Engrg.*, 46:131–150, 1999.

A. Naaman and H. Najm. Bond-slip mechanisms of steel fibers in concrete. *ACI Materials J.*, 88:135–145, 1991.

A. Naaman and H. Reinhardt. Proposed classification of HPFRC composites based on their tensile response. *Materials and Structures*, 39:547–555, 2006.

M. Nataraja, N. Dhang, and A. Gupta. Stress-strain curves for steel-fiber reinforced concrete under compression. *Cement and Concrete Composites*, 21(5-6):383 – 390, 1999.

NB. *Sprayed Concrete for Rock Support - Technical Specifications and Guidelines*. Norvegian Concrete Association, 7, 74 pp., 1993.

NBN-B-15-238. *Essai des betons renforces des fibres. Essai de Flexion sur eprouvettes prismatiques (Testing of fiber reinforced concrete. Bending test on prismatic specimens)*. Belgian Code - In French, 1992.

NFP-18409. *Beton avec fibres metalliques - Essai de flexion (Steel Fiber Concrete - Bending test)*. French Code - In French, 1993.

T.-H. Nguyen, A. Toumi, and A. Turatsinze. Mechanical properties of steel fibre reinforced and rubberised cement-based mortars. *Materials & Design*, 31(1):641 – 647, 2010.

B. Oh, J. Kim, and Y. Choi. Fracture behavior of concrete members reinforced with structural synthetic fibers. *J. of Engrg. Mechanics - ASCE*, 74:243–257, 2007.

J. Olesen. Fictitious crack propagation in fiber-reinforced concrete beams. *J. of Engrg. Mechanics - ASCE*, 127(3):272–280, 2001.

J. Oliver. Consistent characteristic length for smeared cracking models. *Int. J. for Numerical Methods in Engrg.*, 28:461–474, 1989.

J. Oliver. Modelling strong discontinuities in solid mechanics via strain softening constitutive equation. 1. fundamentals. *Int. J. for Numerical Methods in Engrg.*, 39: 3575–3600, 1996.

J. Oliver, A. Huespe, M. Pulido, and E. Chaves. From continuum mechanics to fracture mechanics: the strong discontinuity approach. *Engrg. Fracture Mechanics*, 69:113–136, 2002.

J. Oliver, A. Huespe, and P. Sanchez. A comparative study on finite elements for capturing strong discontinuities: E-FEM vs X-FEM. *Computer Methods in Applied Mechanics and Engrg.*, 195:4732–4752, 2006.

J. Oliver, D. Linero, A. Huespe, and O. Manzoli. Two-dimensional modeling of material failure in reinforced concrete by means of a continuum strong discontinuity approach. *Computer Methods in Applied Mechanics and Engrg.*, 197:332–348, 2008.

J. Oliver, D. Mora, A. Huespe, and R. Weyler. A micromorphic model for steel fiber reinforced concrete. *International Journal of Solids and Structures*, 49(21):2990 – 3007, 2012.

A. Pandolfi and M. Ortiz. An efficient adaptive procedure for three-dimensional fragmentation simulations. *Engineering with Computers*, 18:148–159, 2002.

A. Pandolfi, P. Guduru, M. Ortiz, and A. Rosakis. Three dimensional cohesive-element analysis and experiments of dynamic fracture in C300 steel. *Int. J. of Solids and Structures*, 37:3733–3760, 2000.

K. Park, G. Paulino, and J. Roesler. Cohesive fracture model for functionally graded fiber reinforced concrete. *Cement and Concrete Composites*, 40:956–965, 2010.

S. Park, D. Kim, G. Ryu, and K. Koh. Tensile behavior of ultra high performance hybrid fiber reinforced concrete. *Cement and Concrete Composites*, 34(2):172 – 184, 2012.

R. Peerlings, T. Massart, and M. Geers. A thermodynamically motivated implicit gradient damage framework and its application to brick masonry cracking. *Computer Methods in Applied Mechanics and Engrg.*, 193(30-32):3403 – 3417, 2004.

E. B. Pereira, G. Fischer, and J. A. Barros. Direct assessment of tensile stress-crack opening behavior of strain hardening cementitious composites (SHCC). *Cement and Concrete Research*, 42(6):834 – 846, 2012.

S. Pont and A. Ehrlacher. Numerical and experimental analysis of chemical dehydration, heat and mass transfers in a concrete hollow cylinder submitted to high temperatures. *International Journal of Heat and Mass Transfer*, 47(1):135 – 147, 2004.

F. Puertas, M. Palacios, H. Manzano, J. Dolado, A. Rico, and J. Rodríguez. A model for the c-a-s-h gel formed in alkali-activated slag cements. *Journal of the European Ceramic Society*, 31(12):2043 – 2056, 2011.

T. Rabczuk and T. Belytschko. Application of particle methods to static fracture of reinforced concrete structures. *Int. J. of Fracture*, 137(1-4):19–49, 2006.

F. Radtke, A. Simone, and L. Sluys. A computational model for failure analysis of fibre reinforced concrete with discrete treatment of fibres. *Engrg. Fracture Mechanics*, 77 (4):597 – 620, 2010.

RILEM-TC162-TDF. *Test and design methods for steel fibre reinforced concrete: bending test.* 2002.

RILEM-TC162-TDF. Test and design methods for steel fibre reinforced concrete - σ - ϵ design method: final recommendation. *Mater Struct*, 36(262):560 – 567, 2003.

J. Rodriguez. *Study of behavior of granular heterogeneous media by means of analogical mathematical discontinuous models.* Thesis presented to the Universidad Politecnico de Madrid, at Madrid, Spain, in partial fulfillment of the requirements for the degree of Doctor of Philosophy (in Spanish), 1974.

J. Rots, P. Nauta, G. Kusters, and J. Blaauwendraad. Smeared crack approach and fracture localization in concrete. *Heron*, 30:1–49, 1985.

M. Sahmaran and I. Yaman. Hybrid fiber reinforced self-compacting concrete with a high-volume coarse fly ash. *Construction and Building Materials*, 21(1):150 – 156, 2007.

E. Schauffert and G. Cusatis. Lattice discrete particle model for fiber reinforced concrete (LDPM-F): I. theory. *J of Eng Mech*, 138(7):826–833, 2012.

E. Schauffert, G. Cusatis, D. Pelessone, J. O'Daniel, and J. Baylot. Lattice discrete particle model for fiber reinforced concrete (LDPM-F): II: Tensile fracture and multiaxial loading behavior. *J of Eng Mech*, 138(7):834–841, 2012.

E. Schlangen, E. Koenders, and K. van Breugel. Influence of internal dilation on the fracture behaviour of multi-phase materials. *Engineering Fracture Mechanics*, 74 (1–2):18 – 33, 2007.

H. Schorn and U. Rode. *3-D modelling of process zone in concrete by numerical simulation.* In: Shah SP, Swartz SE, editors. Fracture of concrete and rock. New York: Springer Verlag; pp. 220-228, 1987.

G. D. Schutter. Applicability of degree of hydration concept and maturity method for thermo-visco-elastic behaviour of early age concrete. *Cement and Concrete Composites*, 26(5):437 – 443, 2004.

P. E. C. Seow and S. Swaddiwudhipong. Failure surface for concrete under multiaxial load - a unified approach. *ASCE - J. of Materials in Civil Engrg.*, 17(2):219–228, 2005.

P. Shah and C. Ouyang. Mechanical behavior of fiber-reinforced cement-based composites. *J. of Engrg. Mechanics - ASCE*, 74(11):2727–2738, 1991.

S. Shah. Size-effect method for determining fracture energy and process zone size of concrete. *Materials and Structures*, 23:461–465, 1990.

J. Shannag, R. Brincker, and W. Hansen. Pullout behavior of steel fibers from cement-based composites. *Cement and Concrete Research*, 27:925–936, 1997.

SIA-162-6. *Stahlfaserbeton*. Schweizerischer Ingenieur und Architekten-Verein, Postfach, 8039 Zurich, 1999.

J. Simo and T. Hughes. *Computational Inelasticity*, volume 7. Interdisciplinary Applied Mathematics, Springer, New York, 1998.

I. Singh, B. Mishra, and M. Pant. An enrichment based new criterion for the simulation of multiple interacting cracks using element free Galerkin method. *Int. J. of Fracture*, 167:157–171, 2011.

S. Singh, A. Shukla, and R. Brown. Pullout behavior of polypropylene fibers from cementitious matrix. *Cement and Concrete Research*, 34(10):1919 – 1925, 2004.

L. Sorelli, A. Meda, and G. Plizzari. Bending and uni-axial tensile tests on concrete reinforced with hybrid steel fibers. *ASCE - J. of Materials in Civil Engrg.*, 17(5):519 – 527, 2005.

P. Soroushian and C. Lee. Distribution and orientation of fibers in steel fiber reinforced concrete. *ACI - Materials J*, 87(5):433–439, 1990.

P. Soroushian, K. Obaseki, and M. Rojas. Bearing strength and stiffness of concrete under reinforcing bars. *ACI Materials J.*, 84(3):179–184, 1987.

Stalfiberbetong. *Rekommendationer for konstruction, utforande och provning Betongrapport n.4*. Svenska Betongforeningen, Betongrapport, 1995.

H. Stang and J. Olesen. On the interpretation of bending tests on FRC materials. In N. Bicanic, R. de Borst, H. Mang, and G. Meschke, editors, *Third Int. Conference on Fracture Mechanics of Concrete and Concrete Structures (FRAMCOS-3), Gifu, Japan*, pages 511–520, 1998.

H. Stang, Z. Li, and S. Shah. Pullout problem: stress versus fracture mechanical approach. *J. of Engrg. Mechanics - ASCE*, 116(10):2136–2150, 1990.

T. Stankowski, K. Runesson, and S. Sture. Fracture and slip of interfaces in cementitious composites. I: Characteristics, II: Implementation. *ASCE - J. Engrg. Mech.*, 119(2): 292–327, 1993.

P. Stroeven. *Local strength reduction at boundaries due to nonuniformity of steel fibre distribution.* In: Proceedings of the international conference "Specialist Techniques and Materials for Concrete Construction", Dundee (UK), 8–10 September 1999, p. 377–87, 1999.

H. Tlemat, K. Pilakoutas, and K. Neocleous. Stress-strain characteristic of SFRC using recycled fibres. *Materials and Structures*, 39:365–377, 2006.

C. Trusdell and R. Toupin. *The classical field theories,*, volume III/I. Handbuch der Physik, Springer-Verlag, Berlin, 1960.

F. Ulm and O. Coussy. The chunnel fire i: Chemoplastic softening in rapidly heated concrete. *ASCE, Journal of Engineering Mechanics*, 125(3):272 – 282, 1999a.

F. Ulm and O. Coussy. The chunnel fire ii: Analysis of concrete damage. *ASCE, Journal of Engineering Mechanics*, 125(3):283 – 289, 1999b.

UNE-83510. *Hormigones con Fibras de Acero y/o Polipropileno. Determinacion del Indice de tenacidad de resistencia a primera fisura (Steel and/or polypropylene fiber concrete. Determination of the toughness index of the first crack strength).* Spanish Code - In Spanish, 1989.

UNI-11039-1. *Steel fibre reinforced concrete - Definitions, classification and designation.* UNI Editions, Milan, Italy, 2003.

UNI-11039-2. *Steel fibre reinforced concrete - Test method to determine the first crack strength and ductility indexes.* UNI Editions, Milan, Italy, 2003.

UNI-11188. *Design, production and control of Steel Fibre Reinforced structural elements.* Italian Board of Standardization, Italy, 2004.

UNI-EN-12620. *Aggregates for concrete*, volume Ref. No. EN 12620:2002 E. Europ. Committee for Standardization, Brussels, 2002.

M. Valle and O. Buyukozturk. Behavior of fiber-reinforced high-strength concrete under direct shear. *ACI Materials J.*, 90(2):122–133, 1993.

J. van Mier, M. van Vliet, and T. Wang. Fracture mechanisms in particle composites: statistical aspects in lattice type analysis. *Mech. of Materials*, 34:705–724, 2002.

I. Vardoulakis and E. C. Aifantis. A gradient flow theory of plasticity for granular materials. *Acta Mechanica*, 87:197–217, 1991.

S. Vrech and G. Etse. Gradient and fracture energy-based plasticity theory for quasi-brittle materials like concrete. *Computer Methods in Applied Mechanics and Engrg.*, 199(1-4):136 – 147, 2009.

S. Vrech, G. Etse, G. Meschke, A. Caggiano, and E. Martinelli. Meso- and macroscopic models for fiber-reinforced concrete. In N. Bicanic, R. de Borst, H. Mang, and G. Meschke, editors, *Computational Modelling of Concrete Structures, Rohrmoos/Schladming, Austria*, pages 241–250, 2010.

R. Walter and J. F. Olesen. Cohesive mixed mode fracture modelling and experiments. *Engrg. Fracture Mechanics*, 75(18):5163 – 5176, 2008.

X. Wang, S. Jacobsen, J. He, Z. Zhang, S. Lee, and H. Lein. Application of nano-indentation testing to study of the interfacial transition zone in steel fiber reinforced mortar. *Cement and Concrete Research*, 39:701–715, 2009.

G. Wells and L. Sluys. A new method for modelling cohesive cracks using finite elements. *Int. J. for Numerical Methods in Engrg.*, 50:2667–2682, 2001.

K. Willam, N. Bicanic, and S. Sture. *Constitutive and Computational Aspects of Strain-Softening and Localization in Solids.* ASME-WAM84, New Orleans, Symp. Vol. G00274 Constitutive Equations: Micro, Macro and Computational Aspects, 233-252, 1984.

Z. Xu, H. Hao, and H. Li. Experimental study of dynamic compressive properties of fibre reinforced concrete material with different fibres. *Materials & Design*, 33(0):42 – 55, 2012.

W. Yao, J. Li, and K. Wu. Mechanical properties of hybrid fiber-reinforced concrete at low fiber volume fraction. *Cement and Concrete Research*, 33(1):27 – 30, 2003.

M. Yip, Z. Li, B.-S. Liao, and J. Bolander. Irregular lattice models of fracture of multiphase particulate materials. *Int. J. of Fracture*, 140:113–124, 2006.

H. Yuan, J. Teng, R. Seracino, Z. Wu, and J. Yao. Full-range behavior of FRP-to-concrete bonded joints. *Engrg. Structures*, 26(5):553 – 565, 2004.

J. Zhang and V. C. Li. Simulation of crack propagation in fiber-reinforced concrete by fracture mechanics. *Cement and Concrete Research*, 34(2):333 – 339, 2004.

J. Zhang and H. Stang. Applications of stress crack width relationship in predicting the flexural behavior of fibre-reinforced concrete. *Cement and Concrete Research*, 28(2): 439–452, 1998.

Z. Zhang, K. Liew, Y. Cheng, and Y. Lee. Analyzing 2D fracture problems with the improved element-free Galerkin method. *Engrg. Analysis with Boundary Elements*, 32:241–250, 2008.

A. Zubelewicz and Z. Bazant. Interface element modeling of fracture in aggregate composites. *J. of Engrg. Mechanics - ASCE*, 113:1619–1630, 1987.